PREPARATION AND SPECTROSCOPIC PROPERTIES OF RARE EARTH-DOPED BISMUTH SODIUM TITANATE-BASED FERROELECTRIC CERAMICS

LAU CHI MAN

M.Phil

The Hong Kong Polytechnic University

2015

The Hong Kong Polytechnic University
Department of Applied Physics

Preparation and Spectroscopic Properties of Rare Earth-doped Bismuth Sodium Titanate-based Ferroelectric Ceramics

Lau Chi Man

A thesis submitted in partial fulfillment of the requirements for the degree of Master of Philosophy

December 2014

CERTIFICATE OF ORIGINALITY

I hereby declare that this thesis is my own work and that, to the best of my knowledge and belief, it reproduces no material previously published or written, nor material that has been accepted for the award of any other degree or diploma, except where due acknowledgement has been made in the text.

_____ (Signed)

Lau Chi Man (Name of student)

Abstract

The photoluminescence (PL) properties of various rare-earth (RE)-doped materials have been investigated extensively. The up-conversion (UC) and down-conversion (DC) luminescent emissions have attracted considerable interest due to the wide variety of applications such as biological imaging, spectral convertor, optical telecommunication and military use. Er^{3+} and Pr^{3+} are the most common lanthanide ions and efficient activators for UC and DC PL. Various multifunctional materials have been developed by combining two or more materials via different fabrication methods or special structure designs. In this work, novel lead-free RE^{3+}-doped PL ferroelectric ceramics have been fabricated and their PL, dielectric, piezoelectric and ferroelectric properties have been investigated. The corresponding PL mechanisms and energy transfer processes have also been deduced. $0.93(Bi_{0.5}Na_{0.5}TiO_3)$-$0.07(BaTiO_3)$ (abbreviated as BNBT) ferroelectric ceramic with good ferroelectric and ferroelectric properties is chosen as the host material for the new PL materials.

BNBT ceramics doped with 0.01 mole Er^{3+} at various sites have been fabricated by the solid state reaction (SSR) method and the effects of the resulting oxygen and cation vacancies have been investigated. The samples are abbreviated as BNBT-Er(y), where y is Bi, Ti, Ba or Na for denoting the ions replaced by the RE dopants. The XRD results reveal that Er^{3+} has diffused into and entered the corresponding sites successfully, and no secondary phase is observed. Under an excitation of 980 nm, the ceramics exhibit strong green and red UC emissions and near-infrared (NIR) and mid-infrared (MIR) DC emissions. Our results also reveal that

the vacancies arisen from charge imbalance between the dopants and the replaced ions could increase the PL intensity of the NIR and MIR emission bands at the expense of the visible emissions. For the BNBT-Er(Ba) and BNBT-Er(Na) ceramics containing cation vacancies (V_c), a looping mechanism is established such that their PL intensities of NIR emission increase by more than 50 % and 70 % respectively. In addition to the good dielectric, piezoelectric and ferroelectric properties, the BNBT-Er(y) ceramics should have great potential for multifunctional applications.

On the basis of the results, BNBT ceramics doped with various contents of Er^{3+} at the Bi-site have then been prepared for studying the resulting effects of Er^{3+}. The samples have a formula of $0.93(Bi_{0.5-x/0.93}Er_{x/0.93}Na_{0.5}TiO_3)$-$0.07(BaTiO_3)$ and are abbreviated as BNBT-xEr, with x varying from 0 to 0.07. Owing to the higher probability of cross relaxation (CR) and efficient multi-phonon relaxation (MPR) at higher Er^{3+} concentrations, the PL intensity of the red emission (660 nm) increases significantly by more than 47 times at x = 0.06. As a result, the Commission Internationale de L'Eclairage (CIE) chromaticity coordinates shift from (0.29, 0.69) at x = 0.005 to (0.49, 0.50) at x = 0.07, and the observed emission color changes from green to yellowish green. Moreover, due to the establishment of a dynamic circulatory energy process at high Er^{3+} concentration (x = 0.06), the PL intensity of the MIR emission (2.62 μm – 2.84 μm) increases by more than 4 times at the expense of NIR emission. The BNBT-xEr ceramics also exhibit good dielectric, piezoelectric and ferroelectric properties, and thus suggesting that they should be promising candidates for multifunctional optoelectronic applications.

For comparing the effects of various RE ions, Pr^{3+}-doped $0.93(Bi_{0.5-x/0.93}Er_{x/0.93}Na_{0.5}TiO_3)$-$0.07(BaTiO_3)$ ceramics (abbreviated as BNBT-xPr,

where x = 0 – 0.02) have been fabricated. The DC PL mechanism and properties have been systemically investigated. The BNBT-xPr ceramics exhibit a low quenching concentration of x = 0.005. Owing to the enhancement of MPR and CR, the PL intensity of most of the emissions decreases by 50% to 75% as the Pr^{3+} concentration increases from 0.0025 to 0.02. On the other hand, the PL intensities of the emissions at 654 nm and 741 nm increase by more than 2 times at x = 0.02. The BNBT-xPr ceramics with x ≤ 0.005 also exhibit good dielectric, piezoelectric and ferroelectric properties, showing great potential for multifunctional optoelectronic applications.

The electric field (E-field)-dependent PL properties of the BNBT ceramics doped with 0.005 mole Er^{3+} at the Bi-site (i.e. BNBT-0.005Er) have been studied and the corresponding mechanism has been investigated. Our results reveal that the E-field does not affect the splitting of energy levels of Er^{3+} in BNBT ceramics. However, it can decrease the PL intensity effectively. Under a static E-field of 3.6 kV/mm, the decrease can be up to 22%. This should be partly attributed to the increase in structural symmetry arisen from dipoles alignment, and partly attributed to the increase in crystal symmetry arisen from E-field induced transformation. Although the change is not entirely reversible in the first E-field cycle (i.e. the E-field is increased stepwise from 0 to 3.6 kV/mm and then decreased back to 0 kV/mm), the reversibility is improved in the consecutive cycles. The difference between the observed PL intensity at the minimum and maximum E-field (0 and 3.6 kV/mm, respectively) remains almost the same for different E-field cycles as well as different samples, suggesting that the ceramics should be potential candidates for electric controlled multifunctional optoelectronic applications.

List of Publication

Peer-reviewed Journals

1. Wu, X., **Lau, C. M.** and Kwok, K. W. "Effect of phase transition on photoluminescence of Er-doped KNN ceramics," *Journal of Luminescence* 155, 343, 2014.
2. **Lau, C. M.,** Wu, X. and Kwok, K. W. "Photoluminescence, ferroelectric, dielectric and piezoelectric properties of Er-doped BNT-BT multifunctional ceramics," *Journal of Applied Surface Science*, 2014.

Presentations in international conferences

1. **Lau, C. M.** and Kwok, K. W. "Photoluminescence, ferroelectric, dielectric and piezoelectric properties of Er-doping BNT-BT multifunctional ceramics," *European Materials Research Society 2014 Spring Meeting*, Lillie, France, 26-30th May 2014.
2. Wu, X., Lin, M., **Lau, C. M.** and Kwok, K. W. "Photoluminescence, ferroelectric, dielectric and piezoelectric properties of sol-gel-derived Er-doped KNN-LN lead-free multifunctional ceramics," *CIMTEC 2014: 13th International Ceramics Congress*, Tuscany, Italy, 8-20th June 2014.

Acknowledgements

I would like to express my sincere appreciation to my supervisor Dr. K. W. Kwok for his patience, advice and constant encouragement throughout my whole period of research work. With his broad knowledge, academic insight, enthusiastic and painstaking guidance, I can finish my MPhil study quickly, smoothly and successfully.

Moreover, I would like to thank Dr. J. H. Hao for the photoluminescence measurements. I gratefully acknowledge the technical support provided by the Materials Research Centre of the Hong Kong Polytechnic University. Without their help, I cannot finish my experimental work readily.

I would also like to thank all members in Dr. Kwok's group, especially Mr. Xiao Wu, Mr. Mau Tak Wong and Mr. Tat Hang Chung, for their friendship, help and valuable discussions on my experiments. In addition, I would like to give my sincere thanks to my colleagues in our department, Mr. Ming Kiu Tsang, Miss Man Ying Lam, Mr. Wing Chung Li, Mr. Ki Fung Kam, Mr. Gongxun Bai, Dr. Yan Chen and Mr. Huajing Fang, for their great help and assistance.

Last but not the least, I am deeply indebted to my family and friends for their understanding, constant support and encouragement.

Table of Contents

Abstract 1

List of Publication 4

Acknowledgements 5

Table of Contents 6

List of Figures 10

List of Table 14

Chapter 1. Introduction 1

1.1. Luminescence 1

1.2. Photoluminescence 1

1.3. Transitions 4

1.3.1. Radiative transition 4

1.3.2. Non-radiative transition 4

1.3.2.1. Multi-phonon relaxation (MPR) 4

1.3.2.2. Energy transfer (ET) 5

1.3.2.3. Cross relaxation (CR) 5

1.4. Up-conversion process 6

1.4.1. Ground state absorption (GSA)/ Excited state absorption (ESA) 7

1.4.2. Energy transfer up-conversion (ETU) 7

1.4.3. Photon avalanche (PA) 8

1.4.4. Up-conversion efficiency 9

1.5. Down-conversion process 9

1.6. Rare-earth ions 11

1.6.1. Erbium ion (Er^{3+}) 14

1.6.2. Praseodymium ion (Pr^{3+}) 15

1.7. Materials 17

1.7.1. Piezoelectricity 17

1.7.2. Ferroelectricity 18

1.7.3. Electrical properties of ferroelectric materials 20

1.7.4. Multifunctional ferroelectric materials 23

1.8. Motivation of work 25

1.9. Scope of work 26

Chapter 2. Ceramics preparation and Characterization 28

2.1. Classification of ceramics in this thesis 28

2.2. Fabrication Process 28

2.2.1. Conventional solid state reaction 28

2.2.2. Poling Process 29

2.3. Characterization of ceramics 30

2.3.1. Structural characterization 31

2.3.1.1. XRD 31

2.3.1.2. FE-SEM 32

2.3.1.3. Raman spectroscopy 33

2.3.2. PL characterization 34

2.3.3. Electrical characterization 36

2.3.3.1. Dielectric measurement 36

2.3.3.2. Piezoelectric measurement 37

2.3.3.3. Ferroelectric measurement 38

Chapter 3. Er^{3+}-doped BNBT ceramics at various sites 40

3.1. Introduction 40

3.2. Structural properties 42

3.2.1. XRD 42

3.2.2. FE-SEM 43

3.2.3. Raman spectroscopy 44

3.3. PL properties 46

3.3.1. PL mechanism 49

3.3.2. Effects of vacancies on PL properties 50

3.4. Electrical properties 53

3.4.1. Dielectric and piezoelectric properties 53

3.4.2. Ferroelectric properties 55

3.5. Conclusion 56

Chapter 4. Er^{3+}-doped BNBT ceramics 58

4.1. Introduction 58

4.2. Structural properties 59

4.2.1. XRD 59

4.2.2. FE-SEM 60

4.3. PL properties 63

4.3.1. Visible UC emissions 63

4.3.2. NIR and MIR DC emissions 66

4.3.3. PL mechanism 68

4.4. Electrical properties 72

4.4.1. Dielectric and piezoelectric properties 72

4.4.2. Ferroelectric properties 74

4.5. Conclusion 75

Chapter 5. Pr^{3+}-doped BNBT ceramics 76

5.1. Introduction 76

5.2. Structural properties 77

5.2.1. XRD 77

5.2.2. FE-SEM 78

5.3. PL properties 80

5.3.1. Photoluminescence Excitation (PLE) 80

5.3.2. Visible to NIR emissions 81

5.3.3. PL mechanism 84

5.4. Electrical properties 86

5.4.1. Dielectric and piezoelectric properties 86

5.4.2. Ferroelectric properties 87

5.5. Conclusion 88

Chapter 6. E-field-dependent PL properties of RE^{3+}-doped BNBT ceramics 89

6.1. Introduction 89

6.2. Preparation of transparent electrode 90

6.3. E-field induced PL property 91

6.4. Conclusion 97

Chapter 7. Conclusion 98

Reference 101

List of Figures

FIGURE 1.1 SCHEMATIC DIAGRAM OF (A) SINGLY DOPED ION SYSTEM (B) CO-DOPED ION SYSTEM. 2

FIGURE 1.2 PHOTOLUMINESCENCE PROCESS 3

FIGURE 1.3. THE SIMPLIFIED ENERGY LEVEL DIAGRAM OF ENERGY TRANSFER BETWEEN TWO IONS 5

FIGURE 1.4 THE SIMPLIFIED ENERGY LEVEL DIAGRAM OF CROSS-RELAXATION BETWEEN TWO IONS 6

FIGURE 1.5 SIMPLIFIED ENERGY LEVEL DIAGRAM OF DIFFERENT TYPE OF UPCONVERSION PROCESSES: (A) EXCITED STATE ABSORPTION (ESA) (B) ENERGY TRANSFER UPCONVERSION (ETU) (C) PHOTON AVALANCHE (PA) 9

FIGURE 1.6 THE SIMPLIFIED ENERGY LEVEL DIAGRAM OF DC PROCESS CAUSED BY (A) MULTI-PHONON RELAXATION OR (B) QUANTUM-CUTTING. 10

FIGURE 1.7 THE DIEKE DIAGRAM - ENERGY LEVELS OF VARIOUS RARE-EARTH IONS[31] 13

FIGURE 1.8 THE SIMPLIFIED ENERGY DIAGRAM OF Er^{3+} UNDER STARK EFFECT. (CHECK THE ACCURACY OF THE FIGURE!!) CHECKED 15

FIGURE 1.9 THE SIMPLIFIED ENERGY LEVEL DIAGRAM OF Pr^{3+} WITH THE LOWEST 4F5D STATE IS (A) ABOVE THE $^1S_0$ STATE. (B) BELOW THE $^1S_0$ STATE. 16

FIGURE 1.10 RELATIONSHIP BETWEEN DIELECTRIC, PIEZOELECTRIC, PYROELECTRIC AND FERROELECTRIC MATERIALS 17

FIGURE 1.11 PEROVSKITE STRUCTURE OF ABO_3. 18

FIGURE 1.12 THE ORIENTATION OF DOMAINS IN A POLYCRYSTALLINE FERROELECTRIC MATERIAL BEFORE AND AFTER POLING.[50] 19

FIGURE 1.13 A STRUCTURE OF ME LAMINATE COMPOSITE 24

FIGURE 2.1 FLOW DIAGRAM OF CERAMICS FABRICATION PROCESS 29

FIGURE 2.2 THE SCHEMATIC DIAGRAM OF POLING SYSTEM. 30

FIGURE 2.3 THE SCHRMATIC DIAGRAM OF X-RAY DIFFRACTION IN CRYSTAL..... 32

FIGURE 2.4 PHOTOGRAPH OF THE PL SPECTROMETER SYSTEM. 34

FIGURE 2.5 PHOTOGRAPH OF THE CHAMBER OF THE PL SPECTROMETER SYSTEM. 36

FIGURE 2.6 THE SCHEMATIC DIAGRAM OF THE EXPERIMENTAL SETUP FOR MEASURING DIELECTRIC PROPERTIES IN FUNCTION OF TEMPERATURE. 37

FIGURE 2.7 THE SCHEMATIC DIAGRAM OF THE EXPERIMENTAL SETUP FOR THE PE LOOP MEASUREMENT.... 39

FIGURE 3.1 XRD PATTERNS OF THE BNBT-ER(Y) CERAMICS. 42

FIGURE 3.2 FE-SEM MICROGRAPHS OF THE BNBT-ER(Y) CERAMICS: (A) Y = 0, (B) Y = BI, (C) Y = TI, (D) Y = BA AND (E) Y = NA. 44

FIGURE 3.3 RAMAN SPECTRA OF THE BNBT-ER(Y) CERAMICS. 46

FIGURE 3.4 VISIBLE UC EMISSION SPECTRA OF THE BNBT-ER(Y) CERAMICS..... 47

FIGURE 3.5 NIR DC EMISSION SPECTRA OF THE BNBT-ER(Y) CERAMICS. 47

FIGURE 3.6 MIR DC EMISSION SPECTRA OF THE BNBT-ER(Y) CERAMICS. 48

FIGURE 3.7 SCHEMATIC DIAGRAM FOR THE PL MECHANISM OF ER^{3+} UNDER AN EXCITATION OF 980 NM. ... 48

FIGURE 3.8 VARIATIONS OF THE RELATIVE INTEGRATED INTENSITIES OF THE GREEN, RED, NIR AND MIR EMISSIONS WITH Y FOR THE BNBT-ER(Y) CERAMICS..... 51

FIGURE 3.9 TEMPERATURE DEPENDENCES OF E_R AND $TAN\Delta$ MEASURED AT 1 KHZ, 10 KHZ AND 100 KHZ FOR THE BNBT-ER(0) CERAMIC. 53

FIGURE 3.10 TEMPERATURE DEPENDENCE OF (A) E_R (B) $TAN\Delta$ MEASURED AT 100KHZ FOR THE BNBT-ER(Y) CERAMICS..... 54

FIGURE 3.11 PE LOOPS OF THE BNBT-ER(Y) CERAMICS 56

FIGURE 4.1 XRD PATTERNS OF THE BNBT-XER CERAMICS (A) FROM 20^{O} TO 80^{O}, (B) 46^{O} TO 47.3^{O}..... 60

FIGURE 4.2 FE-SEM MICROGRAPHS OF THE BNBT-XER CERAMICS, (A) X=0, (B) X=0.005, (C) X=0.01, (D) X=0.02, (E) X=0.03, (F) X=0.04, (G) X=0.05, (H) X=0.06, (I) X=0.07 62

FIGURE 4.3 VISIBLE UC EMISSION SPECTRA OF THE BNBT-XER CERAMICS. 63

FIGURE 4.4 R/G OF THE BNBT-XER CERAMICS. 64

FIGURE 4.5 CIE CHROMATICITY DIAGRAM OF THE BNBT-XER CERAMICS. 65

FIGURE 4.6 PHOTOGRAPHS OF THE VISIBLE EMISSIONS OF THE BNBT-XER CERAMICS. 65

FIGURE 4.7 NIR DC EMISSION SPECTRA OF THE BNBT-XER CERAMICS. 66

FIGURE 4.8 MIR DC EMISSION SPECTRA OF THE BNBT-XER CERAMICS. 67

FIGURE 4.9 PEAK WAVELENGTH OF NIR AND MIR DC EMISSIONS OF THE BNBT-XER CERAMICS. 68

FIGURE 4.10 RELATIVE INTEGRATED INTENSITY OF THE BNBT-XER CERAMICS. 71

FIGURE 4.11 SCHEMATIC DIAGRAM FOR THE PL MECHANISM OF Er^{3+} UNDER AN EXCITATION OF 980 NM. 71

FIGURE 4.12 TEMPERATURE DEPENDENCE OF (A) E_R (B) $TAN\,\Delta$ MEASURED AT 100KHZ OF THE BNBT-XER CERAMICS. 73

FIGURE 4.13 PE LOOPS OF THE BNBT-XER CERAMICS. 74

FIGURE 5.1 XRD PATTERNS OF THE BNBT-XPR CERAMICS. 77

FIGURE 5.2 FE-SEM MICROGRAPHS OF THE BNBT-XPR CERAMICS, (A) X=0, (B) X=0.0025, (C) X=0.005, (D) X=0.0075, (E) X=0.01, (F) X=0.0125, (G) X=0.015, (H) X=0.02. 79

FIGURE 5.3 PLE SPECTRUM OF THE BNBT-0.01PR CERAMICS. 80

FIGURE 5.4 VISIBLE-NIR DC EMISSION SPECTRA OF THE BNBT-XPR CERAMICS. 82

FIGURE 5.5 NIR DC EMISSION SPECTRA OF THE BNBT-XPR CERAMICS. 82

FIGURE 5.6 RELATIVE PEAK INTENSITIES OF THE BNBT-XPR CERAMICS 83

FIGURE 5.7 SCHEMATIC DIAGRAM FOR THE PL MECHANISM OF Pr^{3+} UNDER AN EXCITATION OF 474 NM XENON LAMP. 85

FIGURE 5.8 TEMPERATURE DEPENDENCE OF (A) E_R (B) $TAN\,\Delta$ MEASURED AT 100KHZ OF THE BNBT-XPR CERAMICS. 86

FIGURE 5.9 PE LOOPS OF THE BNBT-XPR CERAMICS. 88

FIGURE 6.1 THE SCHEMATIC DIAGRAM OF MAGNETRON SPUTTERING. 90

FIGURE 6.2 VISIBLE UC EMISSION SPECTRA OF THE BNBT-0.005ER CERAMIC. 91

FIGURE 6.3 E-FIELD DEPENDENCE OF RELATIVE INTENSITY (547 NM) OF THE BNBT-0.005ER CERAMIC. ... 92

FIGURE 6.4 (A) VARIATION OF APPLIED E-FIELD AND (B) E-FIELD DEPENDENCE OF RELATIVE PL INTENSITY (547 NM) OF THE BNBT-0.005ER CERAMIC. THE INSET PRESENTS THE RELATIVE PL INTENSITY (547 NM) AT 0 AND 3.6 KV/MM IN THE CONSECUTIVE E-FIELD CYCLES. 94

FIGURE 6.5 RELATIVE PL INTENSITY (547 NM) OF THE BNBT-0.005ER CERAMICS UNDER CONSTANT E-FIELD. 95

FIGURE 6.6 RELATIVE PL INTENSITY (547 NM) OF THE BNBT-0.005ER CERAMIC AT 0 AND 3.6 KV/MM IN THE CONSECUTIVE E-FIELD CYCLES. 96

List of Table

TABLE 1.1 ELECTRONIC CONFIGURATIONS OF TRIVALENT RARE-EARTH IONS IN THE GROUND STATE 12

TABLE 3.1 AVERAGE GRAIN SIZES OF THE BNBT-ER(Y) CERAMICS. 44

TABLE 3.2 DIELECTRIC CONSTANT, DIELECTRIC LOSS, AND PIEZOELECTRIC CONSTANT OF THE BNBT-ER(Y) CERAMICS 55

TABLE 4.1 AVERAGE GRAIN SIZES OF THE BNBT-XER CERAMICS. 62

TABLE 4.2 DIELECTRIC CONSTANT, DIELECTRIC LOSS AND PIEZOELECTRIC CONSTANT OF THE BNBT-XER CERAMICS. 73

TABLE 5.1 AVERAGE GRAIN SIZES OF THE BNBT-XPR CERAMICS 79

TABLE 5.2 DIELECTRIC CONSTANT, DIELECTRIC LOSS AND PIEZOELECTRIC CONSTANT OF THE BNBT-XPR CERAMICS. 87

Chapter 1. Introduction

1.1. Luminescence

Luminescence is an emission of light by some cool substance, when they are excited by external source such as energetic electron beam, electric current or electromagnetic radiation. The emissions not only in visible region (400 – 700 nm) of the electromagnetic wave spectrum, but also in the ultraviolet (UV) and infrared (IR) regions [1][2]. Because of the rapid development of science and technology, different kinds of luminescence have been extensively studied and applied in a number of high-technology products. Cathodoluminescence (CL) is produced by the bombardment between a beam of energetic electrons and luminescent materials. The most typical example is the cathode-ray tube (CRT) in televisions and monitors. Electroluminescence (EL) is the phenomenon caused by electric current. Electrons in conduction band recombine with holes in valence band, and thus energy is released according to the band gap energy of the material. Recombination of electron-hole pairs on different energy levels results in different emissions. One of the examples is Light-emitting diodes (LEDs), which are widely used as a component of LED displays[3].

1.2. Photoluminescence

Photoluminescence (PL) starts with the absorption of photon energy. The mechanisms can be explained by Fig. 1. Fig. 1.1a shows a singly-doped system containing activator (denoted as “A”), which is responsible for emitting the output photon and then also called luminescent center. The activator ions first absorb the

incoming photon energy and are excited to high energy levels. Due to the instability at the high energy levels, they return to the ground state and emit a photon. For example, a ferroelectric host material $SrBi_4Ti_4O_{15}$ containing Er^{3+} ions as activators emits green and red light under 980 nm excitation [4]. Fig. 1b shows a co-doped system containing sensitizers (denoted as "S") as well as activators. Owing to the larger absorption cross-section, sensitizers absorb the incoming photon energy with higher efficiency and then transfer to activators for exciting them to high-energy levels. Such a co-doped system can solve the problem of poor absorption cross-section of activators and then enhance the luminescence efficiency. Yb^{3+} is a common sensitizer widely used for co-doping with Er^{3+}, Tm^{3+} and Ho^{3+}[5][6][7]. Nowadays, the activators as well as sensitizers in most of the luminescent materials are mainly the rare-earth ions (RE^{3+}).

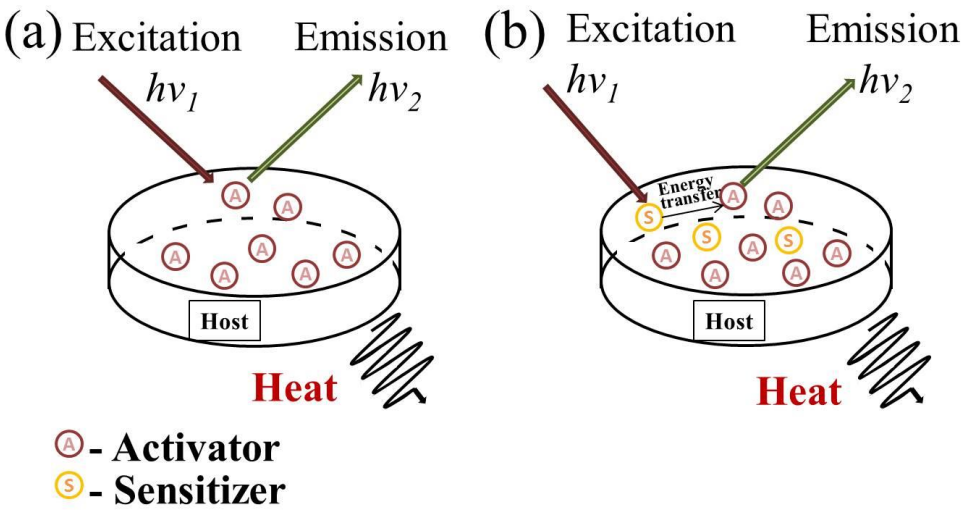

Figure 1.1 Schematic diagram of (a) singly doped ion system (b) co-doped ion system.

The PL process is schematically shown in Fig. 1.2. When a luminescent material is irradiated by an excitation source with energy equal to or a little greater than the

difference between their energy levels, an electron originally in ground state absorbs the incoming energy and is excited to the high energy levels. Owing to the instability, the electron then relaxes to the lower energy level by non-radiative transitions, in which part of the absorbed energy is dissipated as heat, in the form of phonons. Finally, the electron returns to the ground state by radiative transition, in which a photon with energy equal to the difference between the two energy levels is emitted. If the energy of the emitted photon is larger than that of the excitation source, the process is called as anti-stoke shift or up-conversion (UC) process.

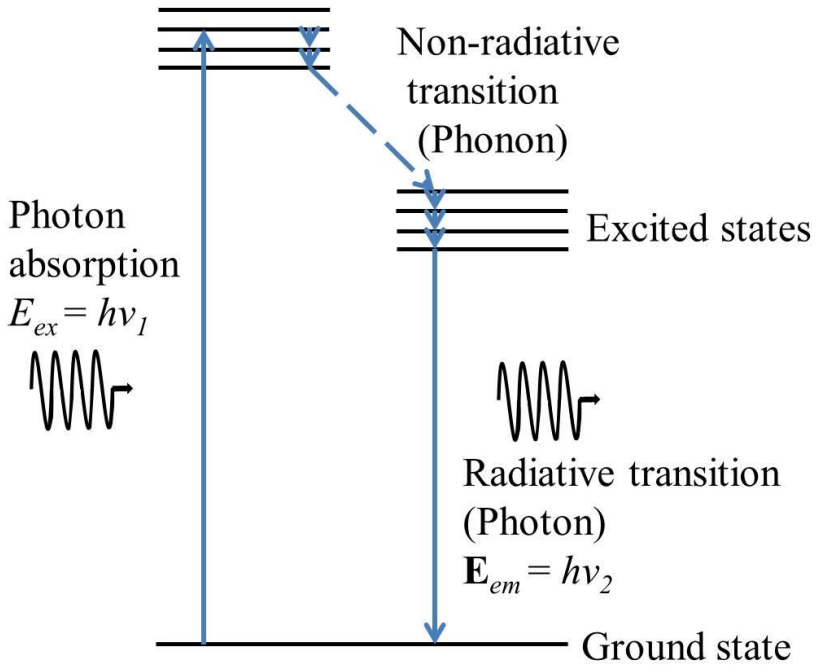

Figure 1.2 Photoluminescence process

1.3. Transitions

Although there are different ways for the excited electrons to return to the ground state, the involved transitions can generally be divided into two classes, i.e., radiative and non-radiative transitions.

1.3.1. Radiative transition

Radiative transition refers to the de-excitation of an excited electron to the ground state via the emission of photons. The wavelength of emitted photons λ_{em} can be in the range of UV, visible light or IR, and is determined by the energy difference between the excited and ground state following an equation: $E = hc/\lambda_{em}$.

1.3.2. Non-radiative transition

Multi-phonon relaxation (MPR), energy transfer (ET) and cross relaxation (CR) belong to non-radiative transitions, which refer to the relaxation to lower energy levels without the emission of photons. However, CR and ET can take place between energy gaps with equal energies or difference energies by one or two phonon energy. Excess energy will be dissipated in form of phonons [3].

1.3.2.1. Multi-phonon relaxation (MPR)

MPR is a process that an excited electron loses its energy by emission of phonons. MPR is an energy-gap-dependent process, as several phonons are required to achieve the process if the energy gap between the excited and next-lower energy levels is larger than the maximum phonon energy of the host [8][9]. It has been reported that the MPR rate decreases exponentially with increasing energy gap to the next-lower energy level

[10][11]. Therefore, MPR usually occurs between energy levels with small energy gaps and stop at the light-emitting levels, which are at least 2×10^3 cm^{-1} away from the next energy level[1][3].

1.3.2.2. Energy transfer (ET)

ET refers to energy migration between two neighboring ions, either between sensitizer and activator or two activators. The probability of ET increases when the ions are getting close to each other. Fig. 1.3 shows schematically the resonant non-radiative energy transfer process, in which the electron in the excited energy level E2 releases its energy to another electron for exciting it to the energy level E2 [3][12].

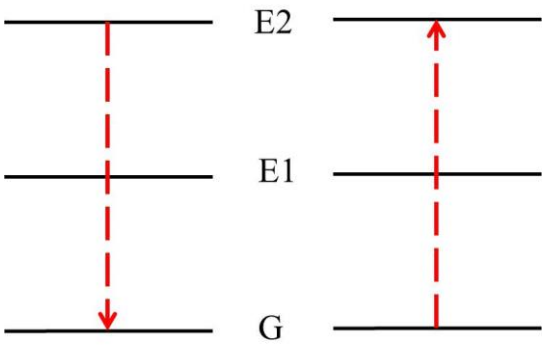

Figure 1.3. The simplified energy level diagram of energy transfer between two ions

1.3.2.3. Cross relaxation (CR)

Similar to ET, CR occurs between two ions, where the separations of energy levels are the same or nearly the same with one or two phonons difference [3]. Three types of CR processes are schematically shown in Fig. 1.4. CR1 (red arrows) and CR2 (green arrows) occur between two pairs of energy levels with identical separation equal energy gaps. For CR1 process, the excited electron loses all of its absorbed energy from E1 to

the ground level G for exciting another electron from E2 to a higher energy level E3, whereas the excited electron in CR2 loses only part of its energy to E2 for exciting another electron from the ground level to the same energy level E2. Unlike CR1 and CR2, CR3 (blue arrows) occurs between two pairs of energy levels with difference separations, in which the excessive energy is emitted as phonons. Similar to CR2, the excited electron in CR3 process releases part of its energy for exciting another electron to occupy the same energy level E2. It has been reported that ET and CR are the dominant non-radiative transitions at high concentration of activators [8][13].

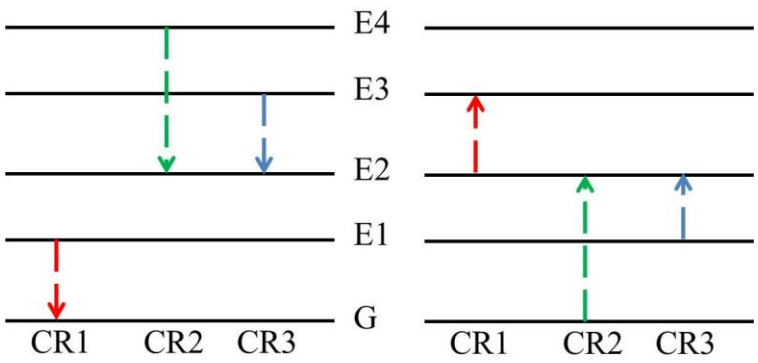

Figure 1.4 The simplified energy level diagram of cross-relaxation between two ions

1.4. Up-conversion process

UC luminescence is a non-linear optical process in which two or more incoming photons are absorbed sequentially and converted into a photon with higher energy. However, it is different from multi-photon process and second harmonic generation (SHG), both of which are also non-linear optical processes but the photons are absorbed simultaneously [14][15]. Moreover, instead of using expensive high-intensity (10^6 – 10^9 W/cm^2) pulsed laser source, a low power (1 – 10^3 W/cm^2) continuous laser can be used as the excitation source for UC process [16]. Due to the ladder-like and intermediate

long-lived energy levels of RE^{3+} [17], different types of UC process are established. They can be divided into three types of processes; ground state absorption (GSA)/excited state absorption (ESA) process, energy transfer up-conversion (ETU) process and photon avalanche (PA).

1.4.1. Ground state absorption (GSA)/ Excited state absorption (ESA)

This is the simplest UC process and occurs typically in a singly-doped system. The energy diagram for the process is shown in Fig. 1.4(a). An electron is excited to a high energy level E2 by sequential absorption of two photons. First, the electron is pumped to the intermediate metastable level E1 via a process called GSA. Then, the electron is further excited to populate a higher energy level E2 by the absorption of a second incoming photon. This process is known as ESA. Finally, the electron returns to the ground level G, giving out an UC emission [15][16].

1.4.2. Energy transfer up-conversion (ETU)

Similar to GSA/ESA, ETU completes the excitation process by sequential absorption of photons. However, it usually occurs in a co-doped system containing activators and sensitizers. The simplified energy level diagram for the process is shown in Fig. 1.4(b), in which the energy levels of the sensitizer are given on the left while those of the activator are on the right. In the process, electrons of the two ions in the ground level G absorb the incoming photons and are excited to a high energy level E1. Then, the excited sensitizer transfers its energy to the activator via a process called energy transfer for further exciting the electron of the activator to a higher energy level E2. Finally, the electron of the activator returns to the ground level G, giving out an UC

emission [14][16]. Since energy transfer between two neighboring ions is involved, the ~~UC~~ efficiency of ETU process is influenced significantly by the doping concentration, which determines the separation between the neighboring ions.

1.4.3. Photon avalanche (PA)

The phenomenon of PA was first reported by Chivian's group in 1979, based on their study of laser-pumped Pr^{3+} infrared quantum counters [18]. The PA process can increase the population of the excited level and thus lead to a strong UC emission. The mechanism of PA is illustrated schematically in Fig. 1.4(c). The electron absorbs the incoming photon and then populates the intermediate level E1 via a weak non-resonant GSA (i.e., the absorption energy is slightly greater than the difference between the two energy levels for the transition). The electron is then further excited to the higher energy level E2 via a resonant ESA process. After that, the electron transfers its energy to an un-excited electron of a neighboring ion through cross-relaxation, causing both electrons populating E1 and ready for the next cross-relaxation or ESA process. As a result, a feedback loop of ESA and cross-relaxation is established, and hence the population of E2 increases exponentially and contributes to a strong UC emission. It is important to note that the pumping intensity should reach a critical value to initiate the PA process by achieving the high population of the excited level. It has been reported that the output intensity increases linearly with the pumping intensity below the critical value, but increases by orders of magnitude beyond the critical value. [16][18][19][20][21].

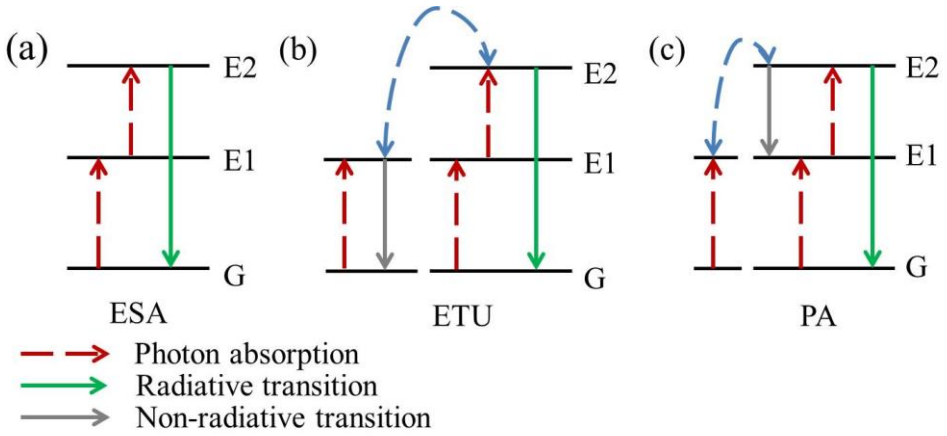

Figure 1.5 Simplified energy level diagram of different type of upconversion processes: (a) excited state absorption (ESA) (b) energy transfer upconversion (ETU) (c) photon avalanche (PA)

1.4.4. Up-conversion efficiency

Owing to the fast response and pump power independence, ETU is the most applicable UC process among the three UC processes. Auzel has also reported that the UC efficiency of ETU is two orders of magnitude higher than that of ESA [22]. Although PA has the highest UC efficiency due to the feedback looping, it suffers from a few drawbacks such as the slow response rate and the higher pumping intensity required for establishing the feedback looping [16].

1.5. Down-conversion process

UC luminescence refers to an emission process for converting low-energy photons to high-energy photons. Conversely, down-conversion (DC) process refers to a conversion process of high-energy photons to low-energy photons [23]. There are usually two types of DC process as shown in Fig. 1.6. First, DC emissions are usually resulted

from MPR followed by radiative relaxation to lower energy levels (Fig. 1.6(a)). For the second type as shown in Fig. 1.6(b), electrons in the high energy level E2 relax to the low energy level E1 through CR and ET. The released energy is absorbed by another electron for the excitation from the ground level G to E1. Finally, all the electrons in E1 relax to G and contribute to DC emissions. The second case establishes only if the energy gaps between G, E1 and E2 are nearly the same. This process divides a high-energy photon into two photons and then is called quantum-cutting, with quantum efficiency more than 100%. The mechanism of quantum-cutting involves one or two luminescent center with different combinations of CR and ET, result in higher population in lower energy level [24][25]. Meijerink and co-workers reported that Yb^{3+}/Pr^{3+} co-doped SrF_2 phosphors show an efficient quantum-cutting of a blue photon (441 nm) into two NIR photons (980 nm) with efficiency of 140 % [26]. Also, it has been reported that Yb^{3+}/Tb^{3+} co-doped YPO_4 phosphors demonstrating an maximum quantum-cutting efficiency of 188% [27].

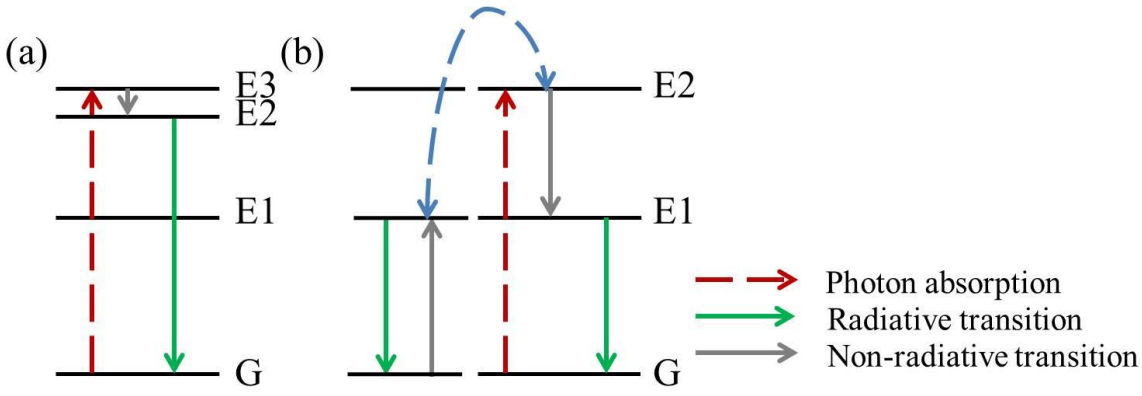

Figure 1.6 The simplified energy level diagram of DC process caused by (a) multi-phonon relaxation or (b) quantum-cutting.

1.6. Rare-earth ions

There are two groups of trivalent RE^{3+}, which also called lanthanide ions. The first one is the ions with closed-shell electron configurations, such as scandium (Sc^{3+}), yttrium (Y^{3+}), lanthanum (La^{3+}) and lutetium (Lu^{3+}), and the other group is the ions with partially filled 4f subshell. The electronic configurations of RE^{3+} in the ground state are shown in Table 1.1. A term symbol $^{2S+1}L_J$ shows the characteristic of each RE^{3+}, where S, L and J refer to the spin angular momentum, orbital angular momentum and total angular momentum, respectively. The electronic transitions between the (partially filled) 4f subshell are responsible for the absorption or emission of light in the range of IR to UV [8]. Accordingly, owing to the closed-shell electron configuration, the first group of RE^{3+} cannot serve as luminescent centers. On the other hand, as the 4f electrons of the second group of RE^{3+} are effectively shielded by the filled 5s and 5p electron shell, the energy levels of their 4f electrons and thus the absorption or emission of light are normally not affected by the surroundings or crystal field [2][28]. The electrostatic interaction between the 4f electrons of the RE^{3+} causes energy level splitting in the order of 10^4 cm^{-1}. Besides, spin-orbit coupling causes further splitting of energy levels in the order of 1000 cm^{-1}, which are determined by the degeneracy (2J+1) or (J+1/2) for J being an integer or a half-integer respectively, whereas degeneracy is an integer. Nevertheless, the energy levels will be split into a number of sublevels after they are doped into a host. The splitting which depends on the symmetry of the crystal field provided by the host is known as Stark effect. The energy range of Stark splitting is about 100-500 cm^{-1} [1][29][30]. The Dieke diagram showing the energy levels for the second group of RE^{3+} is given in Fig. 1.7. In the diagram, the black blocks represent groups of split sublevels, and the red dots indicate the light-emitting levels [1][31]. Owing

to the huge number of energy levels, RE^{3+} is able to absorb or emit light over a wide range from MIR to UV. Moreover, RE^{3+} provides high energy transfer efficiency, chemical and physical stability and low quenching temperature. These make RE^{3+} have been widely investigated and used in various applications, such as solid state laser, spectral convertor, biological imaging, optical telecommunication, remote sensing, military countermeasures, atmospheric pollution monitoring and optical parametric oscillators [16][17][32][33][34][35].

Table 1.1 Electronic configurations of trivalent rare-earth ions in the ground state

Atomic number	Ions	Correspon-ding element	4*f* electrons							S	L	J
21	Sc^{3+}	Ar								0	0	0
39	Y^{3+}	Kr								0	0	0
57	La^{3+}	Xe								0	0	0
58	Ce^{3+}	Xe	↑							1/2	3	5/2
59	Pr^{3+}	Xe	↑	↑						1	5	4
60	Nd^{3+}	Xe	↑	↑	↑					3/2	6	9/2
61	Pm^{3+}	Xe	↑	↑	↑	↑				2	6	4
62	Sm^{3+}	Xe	↑	↑	↑	↑	↑			5/2	5	5/2
63	Eu^{3+}	Xe	↑	↑	↑	↑	↑	↑		3	3	0
64	Gd^{3+}	Xe	↑	↑	↑	↑	↑	↑	↑	7/2	0	7/2
65	Tb^{3+}	Xe	↑↓	↑	↑	↑	↑	↑	↑	3	3	6
66	Dy^{3+}	Xe	↑↓	↑↓	↑	↑	↑	↑	↑	5/2	5	15/2
67	Ho^{3+}	Xe	↑↓	↑↓	↑↓	↑	↑	↑	↑	2	6	8
68	Er^{3+}	Xe	↑↓	↑↓	↑↓	↑↓	↑	↑	↑	3/2	6	15/2
69	Tm^{3+}	Xe	↑↓	↑↓	↑↓	↑↓	↑↓	↑	↑	1	5	6
70	Yb^{3+}	Xe	↑↓	↑↓	↑↓	↑↓	↑↓	↑↓	↑	1/2	3	7/2
71	Lu^{3+}	Xe	↑↓	↑↓	↑↓	↑↓	↑↓	↑↓	↑↓	0	0	0

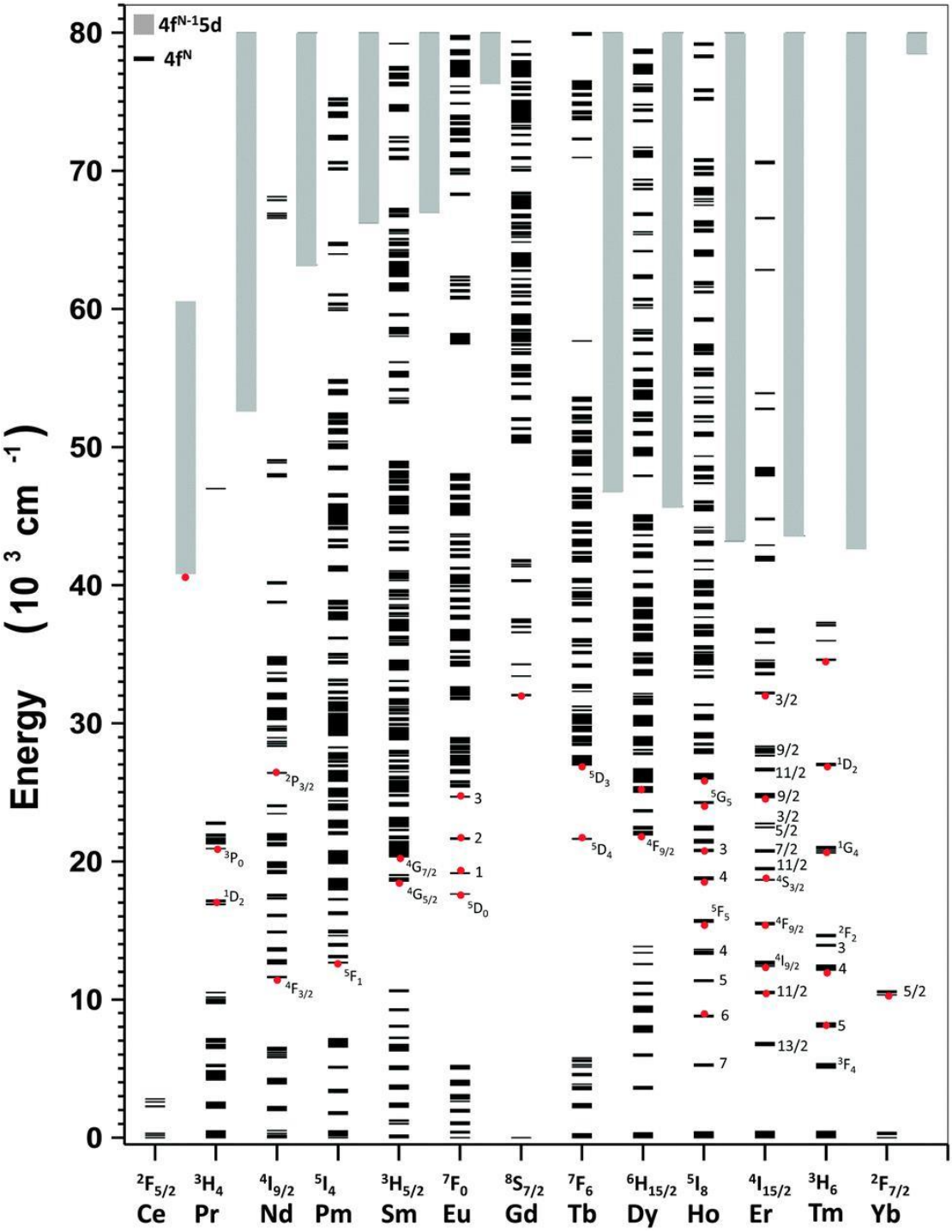

Figure 1.7 The Dieke diagram - energy levels of various rare-earth ions[31]

1.6.1. Erbium ion (Er^{3+})

Erbium (Er) is the 11th member of the lanthanide group. The electron configuration of Er^{3+} is [Xe]$4f^{11}$, where the number 11 indicates Er^{3+} containing 11 electrons in the 4f orbitals. The simplified energy level diagram of a free Er^{3+} and an Er^{3+} doped in a host (showing the Stark splitting) are shown in Fig. 1.8. It can be seen that Er^{3+} has energy levels suitable for giving out green luminescence (530, 550 nm), red luminescence (660 nm), NIR emissions (800, 1550 nm) and MIR emissions (2700 nm), resulting from the transitions $^2H_{11/2}$ / $^4S_{3/2}$ → $^4I_{15/2}$, $^4F_{9/2}$ → $^4I_{15/2}$, $^4I_{9/2}$ / $^4I_{13/2}$ → $^4I_{15/2}$ and $^4I_{11/2}$ → $^4I_{13/2}$, respectively. Although the ions can be excited by UV (450 nm) and NIR (980 nm) light, NIR excitation is preferably used because of the lower energy that can minimize the background autofluorescence, photobleaching and photodamage to specimens [16]. Moreover, Er^{3+} can be singly doped or co-doped with Yb^{3+} in a wide variety of hosts, such as nanoparticles, thin films and ceramics to provide an efficient UC luminescence for different applications [5][22][36][37][38]. Therefore, Er^{3+} is commonly used as luminescent centers for IR to visible up-convertors, NIR amplifiers and MIR photonics. It can also be used to probe physical effects, such as point defects, radiation defects, network structure, optical band structure and so on [39].

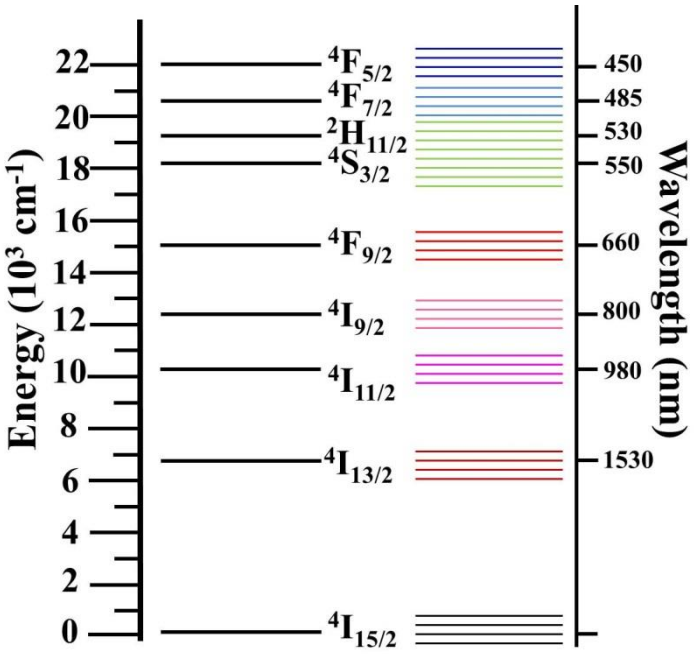

Figure 1.8 The Simplified energy diagram of Er^{3+} under Stark effect.

1.6.2. Praseodymium ion (Pr^{3+})

Pr^{3+} is another common example of luminescent center in the lanthanide group. It has an electron configuration $[Xe]4f^2$ and thus 2 4f electrons. As shown in the simplified energy level diagram (Fig. 1.9), it can give out red and green luminescence under an excitation of blue light (~ 470 nm), which are attributed to the transitions $^3P_0/^1D_2 \rightarrow {}^3F_2/{}^3H_6/{}^3H_4$ and $^3P_1/^3P_0 \rightarrow {}^3H_5$, respectively. Owing to the unique electronic structure, the emission colors and relative intensities of Pr^{3+} under the excitation of vacuum ultraviolet light (~ 185 nm) is strongly dependent on the characteristics of the host. As shown in Fig. 1.9(a), if the lowest 4f5d state is located above the $^1S_0$ state, as in the case of Pr^{3+} doped YF_3, LaF_3 and $NaYF_3$ [40], it can give emissions in violet, red or green luminescence attributing to the two-step $4f^2$-$4f^2$ transitions from the $^1S_0$ state [41]. On the other hand, a broadband luminescence, ranging from UV to blue emission, is

observed for Pr^{3+} doped $LnBO_3$ (Ln= Lu, Y, La). The emission is resulted from the the inter-configurational 4f5d-4f2 transitions. [42].

Owing to the unique performance in PL properties, Pr-doped luminescent materials have been used in various fields, such as a structure transition probe for the ferroelectric [43] or an optical-and-electro multifunctional materials [44][45]. They are also widely used for producing white light via the mixing of the red and green luminescence with the blue excitation source [46][47].

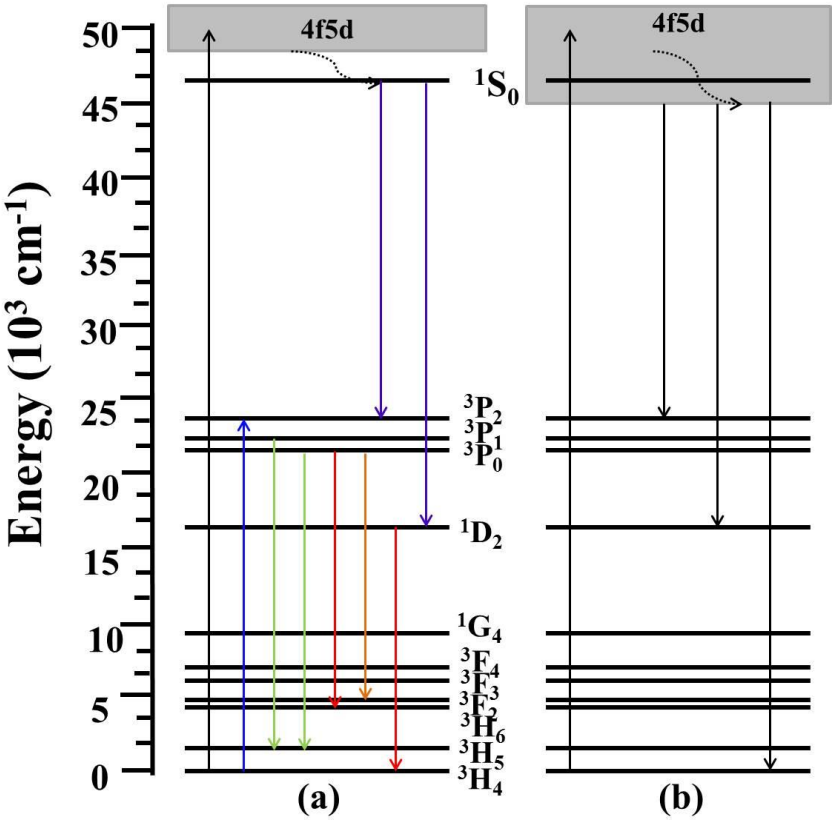

Figure 1.9 The simplified energy level diagram of Pr^{3+} with the lowest 4f5d state is (a) above the $^1S_0$ state. (b) below the $^1S_0$ state.

1.7. Materials

Crystals are divided into 32 point groups depending on their structural parameters, such as center of symmetry, axes of rotation, and mirror planes [48]. The properties of a crystal are determined by its structural parameters [49]. All the members in 32 point groups are dielectrics, 20 of them are centosymmetric while the rest are non-centosymmetrtic. Among the 21 points groups (non-centosymmetric), 20 of them are piezoelectrics due to the lack of center of symmetry and the ability to give an unsymmetric polar result (i.e., polarization). 10 out of 20 piezoelectrics which have a unique polar direction are called pyroelectrics, and for those polar can be reversed are ferroelectrics. Fig. 1.10 shows the relationship of these 32 point groups crystals.

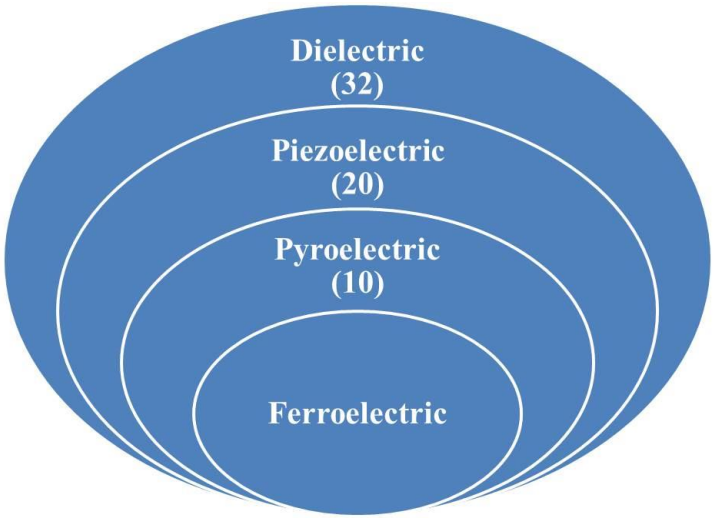

Figure 1.10 Relationship between dielectric, piezoelectric, pyroelectric and ferroelectric materials

1.7.1. Piezoelectricity

Piezoelectricity is a property of certain materials first discovered in 1880 by Jacques and Pierre Curie. For a piezoelectric material, electric charges can be generated on its surface in response to mechanical stress, and this phenomenon is called the direct

piezoelectric effect. The generated charges are resulted from the change in the (spontaneous) polarization, which is arisen from the shifting of positive and negative charges in the unit cells of the material. On the other hand, if an electric field is applied to the material, a strain will be induced. This phenomenon is known as the converse piezoelectric effect. The piezoelectric effects can be described by the constitutive equations as:

$$D = dE + \varepsilon^T E \qquad \text{(Direct piezoelectric effect)}$$

$$S = s^E T + dE \qquad \text{(Converse piezoelectric effect)}$$

where D is the dielectric displacement, T is the stress, E is the electric field, S is the strain, s is the material compliance and d is the piezoelectric constant [48]. The direct and converse piezoelectric effect can be observed in both single crystals and polycrystalline materials. Most of them possess a perovskite structure with chemical formula ABO_3. Fig. 1.11 shows the perovskite structure of ABO_3.

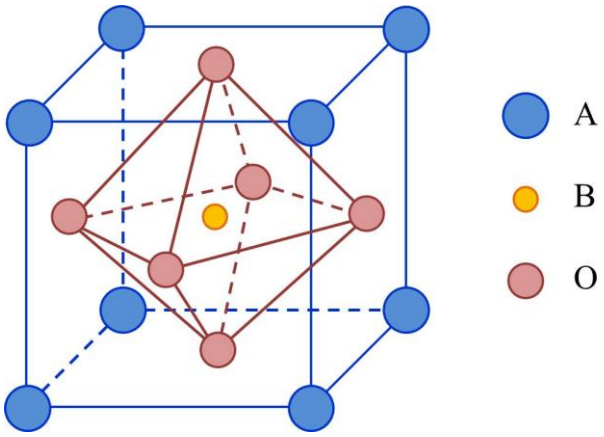

Figure 1.11 Perovskite structure of ABO_3.

1.7.2. Ferroelectricity

Rochelle salt is the firstly discovered material demonstrating ferroelecticity in 1921 [48]. As demonstrated in Fig. 1.10, ferroelectric materials are a sub-group of

piezoelectric materials, thus ferroelectrics must be piezoelectric, but piezoelectrics may not be ferroelectric. Ferroelectrics refer to certain materials that exhibit at least two equilibrium orientations of the spontaneous polarization and the orientation is reversible by applying a strong external E-field across the material [49]. The spontaneous polarizations in polycrystalline materials are not uniformly aligned through the whole material. The homogeneous region in which the spontaneous polarizations are aligned in the same direction is called a ferroelectric domain. The region between two domains is called the domain wall [49][50]. Owing to the random orientations, the spontaneous polarizations of each domain cancel each other, resulting in zero net polarization and thus no observable piezoelectric properties. Therefore, a strong dc electric field is practically needed to re-orient all the spontaneous polarizations (or domains) to the field direction for activating the piezoelectricity of the polycrystalline materials. The process is called poling. Fig. 1.12 shows the orientation of domains in a polycrystalline ferroelectric material before and after poling.

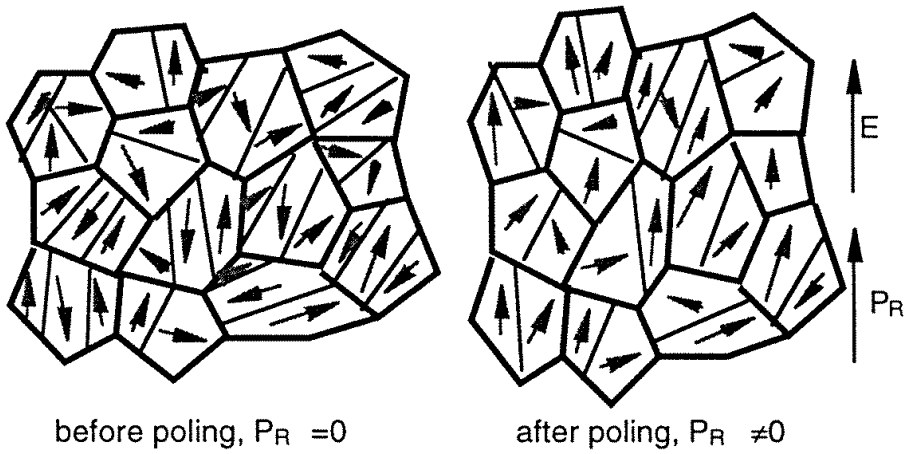

Figure 1.12 The orientation of domains in a polycrystalline ferroelectric material before and after poling.[50]

However, relaxation of the aligned domains (i.e., depolarization) may occur after the removal of dc electric field, especially at high temperatures. The relaxation is caused by point defects in the ferroelectric material, which re-orient the part of the aligned domains back to the direction of the spontaneous polarization. It is described as a relaxation, because the re-orientation takes time to reach an equilibrium [51][52]. Ferroelectric ceramics can be classified into the following four groups:

I. The tungsten-bronze group, such as $Pb_2KNb_5O_{15}$ (PKN) [53], $Ba_2Pr_xNd_{1-x}FeNb_4O_{15}$ [54], $Ba_6M^{3+}Nb_9O_{30}$ (M^{3+}, Ga^{3+}, Sc^{3+} and In^{3+}) [55].
II. The oxygen octahedral group or perovskite group, such as $PbZr_xTi_{1-x}O_3$ (PZT), $K_{0.5}Na_{0.5}NbO_3$ (KNN) and $Bi_{0.5}Na_{0.5}TiO_3$ (BNT).
III. The pyrochlore group, such as $Cd_2Nb_2O_7$ [56], $Ho_2Ti_2O_7$ [57]and La_2ScNbO_7 [58]
IV. The bismuth layer-structure group, such as $Na_{0.5}Bi_{4.5}Ti_4O_{15}$ (NBT) $SrBi_4Ti_4O_{15}$ (SBTi) and $CaBi_4Ti_4O_{15}$ (CBT) [59].

In general, the ferroelectric materials will undergo a structural phase transition from ferroelectric to non-ferroelectric as temperature passes through the Curie temperature (T_c) [48][50]. In the past few decades, ferroelectric materials have been studied and applied extensively in different areas, such as actuators, sensors, ultrasonic imaging devices, transducers capacitors, gas igniters, and positive temperature coefficient sensors and switches [48].

1.7.3. Electrical properties of ferroelectric materials

After the discovery of ferroelectricity and piezoelectricity, polycrystalline ferroelectric ceramics have been studied extensively and applied in numerous applications because of their excellent ferroelectric, pyroelectric, piezoelectric and

dielectric properties. Some ceramics exhibit large piezoelectric constant (d_{33}), electromechanical coupling factor (k_{33}) and dynamic hysteresis characteristics, they are usually used for sensor, actuator and receiver applications. On the other hand, for those can withstand high mechanical stresses and electric fields, they are suitable for high power generator applications, such as ultrasonic cleaners and sonar devices. In the past few decades, lead-based ferroelectric ceramics with a perovskite structure have been widely used in different products due to their excellent piezoelectric properties [60][61].The dominating lead-based ferroelectric materials are the lead zirconate titanate (PZT) ceramics and lead magnesium niobate-lead titanate (PMN-PT) single crystal because of their exhibit excellent piezoelectric properties. It has been reported that PZT ceramics exhibit high d_{33} ~ 289-710 pC/N [62], k_{33} ~ 65% [48] and electric field-induced strain ~0.15% [63]. PMN-PT single crystals also possess ultrahigh d_{33} and $k_{33,}$ >2000 pC/N and >90%, respectively [64]. Although the lead-based ceramics exhibit outstanding piezoelectric properties, they may cause serious harmful effects on human health and environment because of the toxic lead and lead oxides. As a result, there is an urgent demand on lead-free ferroelectric ceramics for replacing the lead-based ceramics.

Barium titanate (BT) is a typical ferroelectric ceramics firstly developed in mid-1940s. It has a tetragonal structure at room temperature, and exhibits a relatively low d_{33} (190 pC/N) and small electromechanical coupling factor k_p (36%). Moreover, its T_c for the structural change from tetragonal phase to cubic phase is low, around 120 °C, which limits the practical use of the ceramics, in particularly for high power applications [65][62]. Accordingly, BT has been supplanted by other ceramics in commercial piezoelectric transducers gradually. Nevertheless, it is still a model

ferroelectric material for capacitors and fundamental investigations because of its high dielectric constant (ε_r) 1700, especially for nanoceramics (ε_r ~10^6) [66].

Barium sodium titanate (BNT) is a promising candidate of lead-free ferroelectric ceramics. It has a perovskite structure with rhombohedral symmetry, and exhibits a high T_c of ~320 °C and a large remnant polarization (P_r) of 38 μC/cm^2. However, it has a high coercive field (E_c) of 7.3 kV/mm at room temperature [67], which makes the poling extremely difficult and thus resulting in a relatively low d_{33} of 70 – 80 pC/N [68]. Moreover, the depolarization temperature of BNT ceramics is low (~187 ℃), limiting its applications at high temperatures. The other drawback of BNT ceramics is the relatively large conductivity [69].

Potassium Sodium Niobate (KNN) is another promising lead-free ferroelectric ceramics. It has orthorhombic sysmmetric at room temperature, and undergoes phase transitions to tetragonal at 200 °C and then to cubic at 420°C (T_c) [70]. However, because of the volatilization of alkaline elements at high temperatures, it is difficult to sinter the ceramics to a high density under the normal condition. As a results, it exhibits weak dielectric and piezoelectric properties, giving ε_r = 290, d_{33} = 80 pC/N and k_p = 35%. It has been reported that hot-pressing is an effective way to improve the sinterability and then the piezoelectric properties of KNN. The dielectric and piezoelectric properties of some hot-pressed KNN ceramics can be enhanced by almost two times, giving ε_r = 500, d_{33} =160 pC/N and k_p = 46% [65][71]. Donor doping has also been shown as another effective way to improve the piezoelectric properties. D. Damjanovic et al. showed that the doping of donor ions such as Li^+ and Ta^{5+} could lead to enhancements of piezoelectric properties of KNN ceramics. The piezoelectric properties of Li^+ and Ta^{5+}-doped KNN ceramics is enhanced by almost four times, giving d_{33} = 310 pC/N,

which is comparable to a commercial PZT ceramics (320 pC/N) [72]. It has also been shown that the d_{33} and k_p of BNT ceramics are enhanced by almost two times via the doping of Li^+ and K^+, exhibiting d_{33} = 160 pC/N and k_p = 16% [73]. Formation of new binary or ternary solid-solution system at or near morphotropic phase boundary (MPB) is an alternative to obtain ceramics with better piezoelectric performance. In general, a solid-solution system possesses an abrupt structural change with various compositions. MPB refers to compositions that two phases coexist and shows best performance [74]. The BNT-BT solid-solution system is one of the promising candidates of lead-free ceramics, which is made up of different compositions of BNT and BT with the general chemical equation of (1-x)(BNT)-x(BT). The piezoelectric and ferroelectric properties enhances as the composition of BT increases and obtain the best performance with d_{33} = 180 pC/N, k_p = 37%, P_r = 16.4 μC/cm^2 and E_c = 3.41 kV/mm at x = 0.06-0.07 (MPB) [67][75][76]. Other than BNBT, KNN-BT [77], KNN-ST [78] and BNT-BZT [43] have also been reported as promising candidates of lead-free ceramics.

1.7.4. Multifunctional ferroelectric materials

Primary ferroics refer to ferroelectrics, ferroelastics, or ferromagnetics, while secondary ferroics refer to ferroelastoelectric, ferromagnetoelastic or ferromagnetoelectric. They are called multifunctional materials as they can respond to more than one external excitation such as electric field, magnetic field or stress. Owing to the multifunctionalities, ferroic materials have attracted considerable interest in recent years, and become important materials for the next-generation of smart devices, sensors and robotic development. There are only a few materials that can exhibit two or more properties, and hence various multifunctional materials have been developed by

combining two or more materials via some special structure design. For example, a magnetoelectric (ME) laminate composite is made by stacking two Terfenol-D disks and one PZT disk together as shown in Fig. 1.13. The resulting ME response is achieved by combining the piezoelectric and magnetostrictive effects. When the composite is subjected to an external magnetic field, the Terfenol-D disk is excited to vibrate in the longitudinal direction (orange arrows) due to the magnetostrictive effect. At the same time, the PZT disk is forced to vibrate in the same direction via mechanical coupling. Finally, a upward polarization is generated by the direct piezoelectric effect [79]. ME laminate composite would be a promising candidate for sensing.

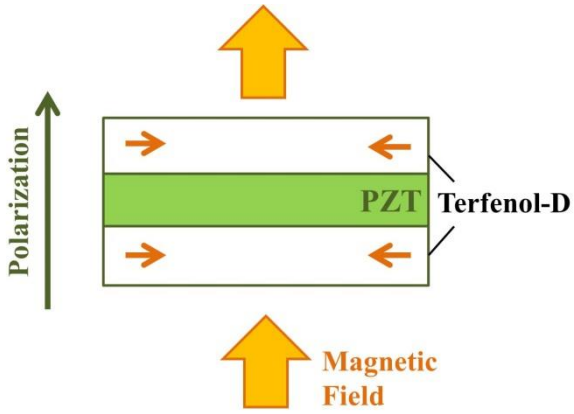

Figure 1.13 A structure of ME laminate composite

Recently, Du et al. have reported that PL and piezoelectric properties can be linked up by doping Er^{3+} into BNT ceramics. The ceramics with small Er^{3+} content (0.01 mol) show the maximum piezoelectric (d_{33} ~90 pC/N) and PL (strongest green emissions) properties under 980 nm excitation [80]. Also, it has been shown that Yb^{3+}/Er^{3+} co-doped BNT ceramics could give stronger emissions than the singly-doped ceramics. The ratio of the emissions at different wavelengths (I_{525}/ I_{550}) varies with temperature from 163K to 613K. They have then suggested that the Er^{3+}-doped and Yb^{3+}/Er^{3+} co-doped BNT ceramics should be a potential candidate of optical temperature sensors [81]. It has also

been reported that electro-mechano-optical conversion could be realized in Pr^{3+}-doped $BaTiO_3$-$CaTiO_3$ and Eu^{3+}-doped $SrAl_2O_4$ ceramics. The mechanical stress and electroluminescence are coupled via the piezoelectric effect. An electrical input could induce mechanical strain and light emission, while a mechanical stress input could induce electric signal and then light emission. They are suggested as a potential candidates for smart-skin and self-diagnosis applications [82][83][84].

1.8. Motivation of work

Because of the increasing desire of the high technology lifestyle such as high-techology products and intelligent systems, there are great demands on multifunctional materials with high performances. PL plays a crucial role on optical applications and researches, in terms of visible UC PL, DC NIR and MIR emissions or colors of emissions. As discussed in above section, the materials combining luminescence and piezoelectric properties can be used in optical temperature sensing or optomechanical applications. In this thesis, we aim to develop a new multifunctional lead-free ceramics possess good PL, dielectric, piezoelectric and ferroelectric properties. Three groups of multifunctional ceramics will be prepared, (1) Er^{3+}-doped BNBT ceramics at various sites, (2) Er^{3+}-doped BNBT ceramics, and (3) Pr^{3+}-doped BNBT ceramics. This work will focus on preparing lead-free piezoelectric ceramics with UC and DC PL via doping Er^{3+} and Pr^{3+}. The dielectric, piezoelectric and ferroelectric properties as well as the PL mechanism of different RE-doped BNBT based ceramics will be discussed under the effect of different doping site and doping concentrations. Also, the effect of (external) E-field on PL properties for the Er^{3+}-doped BNBT ceramics will also be investigated.

1.9. Scope of work

The main objective of this work is to develop a new generation of multifunctional piezoelectric ceramics and study the PL, electrical properties and E-field dependent PL properties of lead-free RE^{3+}-doped BNBT based ceramics. This thesis consists of seven chapters:

In Chapter one, some fundamental information of PL, RE^{3+}, electrical properties of lead-free ceramics and recent development of multifunctional materials are briefly introduced.

In Chapter two, a brief description of the fabrication process of RE-doped BNBT based ceramics and characterization of instruments and techniques, including XRD, Raman, SEM, PL as well as dielectric, piezoelectric and ferroelectric measurements are given.

In Chapter three, the effects of vacancies on PL properties of 1 % of Er-doped BNBT ceramics are investigated, in terms of the UC Vis emissions, DC NIR and MIR emissions. The dielectric, ferroelectric and piezoelectric properties of the ceramics are also studied.

In Chapter four, the concentration effect on UC PL and electrical properties of Er-doped BNBT ceramics are elucidated, based on the characteristics of PL emissions from Vis to MIR regions and electrical measurements.

In Chapter five, DC PL properties of Pr^{3+}-doped BNBT ceramics are reported together with electrical properties. The effect of Pr-doping concentration is also studied in this chapter.

In Chapter six, the E-field dependent PL properties and of Er^{3+}-doped BNBT ceramics are investigated for exploring the potential multifunctional applications of RE^{3+}-doped lead-free ceramics.

Finally, conclusions are given in Chapter seven.

Chapter 2. Ceramics preparation and Characterization

2.1. Classification of ceramics in this thesis

In this thesis, three groups of rare-earth (RE^{3+})-doped ceramics were fabricated by conventional solid state reaction (SSR):

I. 0.01 mol Er^{3+}-doped $0.93(Bi_{0.5}Na_{0.5}TiO_3)$-$0.07(BaTiO_3)$ ceramics at various sites. The ceramics are abbreviated as BNBT-Er(y), where y is Bi, Ti, Ba or Na for denoting the ions replaced by Er^{3+} and 0 for un-doped BNBT.

II. x mol Er^{3+}-doped $0.93(Bi_{0.5-x/0.93}Er_{x/0.93}Na_{0.5}TiO_3)$-$0.07(BaTiO_3)$ with x = 0, 0.005, 0.01, 0.02, 0.03, 0.04, 0.05, 0.06, 0.07. The ceramics are abbreviated as BNBT-xEr.

III. x mol Pr^{3+}-doped $0.93(Bi_{0.5-x/0.93}Pr_{x/0.93}Na_{0.5}TiO_3)$-$0.07(BaTiO_3)$ with x = 0, 0.0025, 0.005, 0.0075, 0.01, 0.0125, 0.015, 0.02. The ceramics are abbreviated as BNBT-xPr.

2.2. Fabrication Process

2.2.1. Conventional solid state reaction

The fabrication process is summarized in Fig. 2.1. The raw materials for making the ceramics are analytical-grade metal oxides or carbonates powders: Bi_2O_3 (99.9%),

Na_2CO_3 (99%), $BaCO_3$ (99.5%), TiO_2 (99.9%), Er_2O_3 (99.99%) and Pr_6O_{11} (99.9%). Powders in the stoichiometric ratio of the compositions were weighed and mixed thoroughly in ethanol using zirconia balls for 8h. After drying, the powders were calcined at 850°C for 2 h in alumina crucible to obtain a chemically and crystallographically uniform structure via the interaction between the ions through the inter-diffusion process. The calcined powders were then ball-milled again for 8h, mixed thoroughly with a 5-wt% polyvinyl alcohol binder solution, and pressed into disk samples with a diameter of 12 mm under a pressure of ~ 300 MPa. The samples were first heated at 650°C for 2 h to remove the binders, and then sintered at 1200°C for 2 h in air to obtain a dense structure.

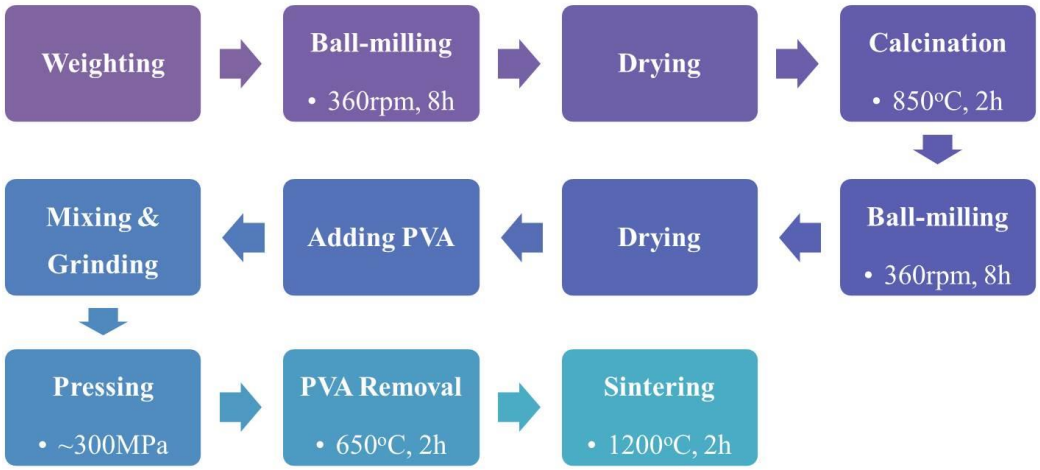

Figure 2.1 Flow diagram of ceramics fabrication process.

2.2.2. Poling Process

As discussed in previous sections, poling is needed for aligning the randomly oriented domains. The sintered ceramics were polished to achieve a flat and smooth surface for poling and other measurements. Before poling, electrodes were deposited on

the surface of ceramics first. The top and bottom surface of ceramics were painted with silver paste and then fired at 750^{o}C for half an hour to form a silver electrode. According to the schematic diagram of the poling system shown in Fig. 2.2, the ceramic sample was submerged in silicone oil and heated to 60^{o}C first. After that, a dc electric field (E-field) of 5.0 kV/mm was applied along the thickness direction for 20 min to fully polarize the sample. Then, the temperature was cooled down to room temperature before the electric field was turned off.

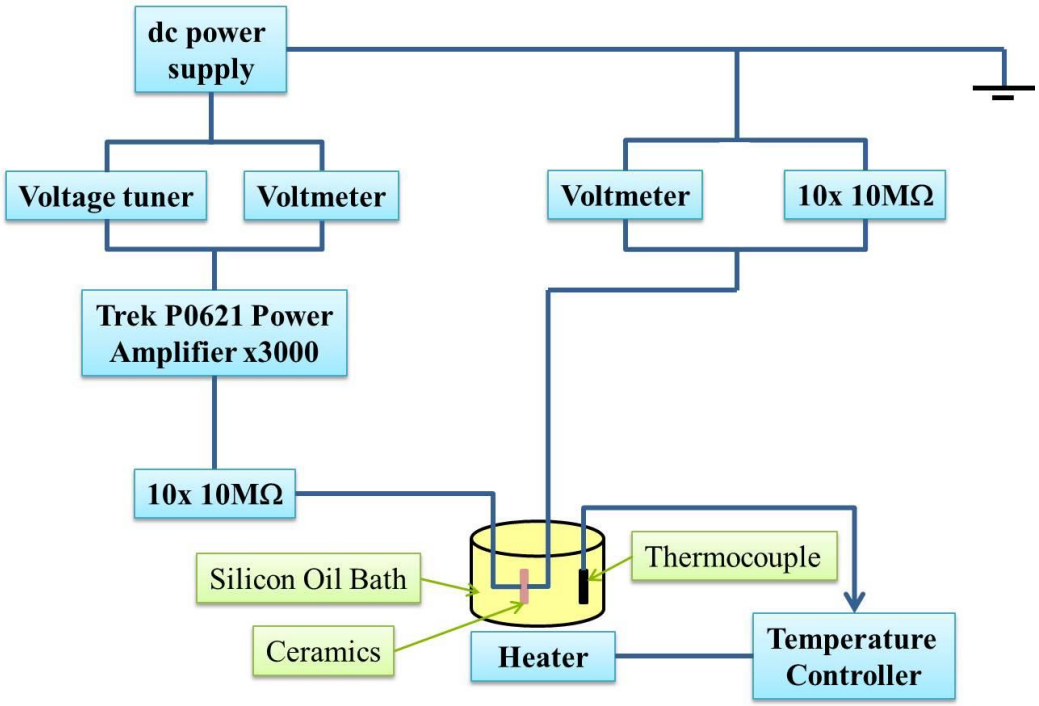

Figure 2.2 The schematic diagram of poling system.

2.3. Characterization of ceramics

In this work, several characterization techniques were used to characterize the structural, photoluminescence (PL) and electrical properties of RE-doped BNBT ceramics. For structural properties, X-ray diffraction (XRD), field-emission scanning

electron microscope (FE-SEM) and Raman spectroscopy were applied. The average grain sizes were determined by the linear intercept method. PL and photoluminescence excitation (PLE) measurements were used to study the PL properties. For electrical properties, dielectric constant (ε_r) and dielectric loss ($tan\ \delta$), piezoelectric constant (d_{33}) and ferroelectric hysteresis loop (PE loop) were measured.

2.3.1. Structural characterization

2.3.1.1. XRD

XRD is an analytical technique to study the structure of crystalline materials. In the measurement, an X-ray beam is incident on the sample surface with an incline angle θ as shown in Fig. 2.3. Owing to the interaction with the crystal lattices, part of the X-rays is scattered to the receiver. Therefore, each crystalline material produces a unique X-ray fingerprint diffraction pattern upon θ that is called an XRD pattern. According to the Bragg's law, maxima occur in the detected intensity (diffraction peaks) when the incident angle satisfies the following condition:

$$2d_{hkl} \sin\theta = n\lambda \tag{3.1}$$

where h, k, l are the Miller indices, d_{hkl} is the interplanar spacing of the $\{hkl\}$ set of lattice planes, θ is the incident angle of the beam, n is the order of diffraction, and λ is the wavelength of the X-ray.

In this study, an X-ray diffractometer (SmartLab, Rigaku Co., Japan) with CuK_α radiation (λ = 0.154 nm) was used to study the crystalline structures of the RE-doped BNBT ceramics.

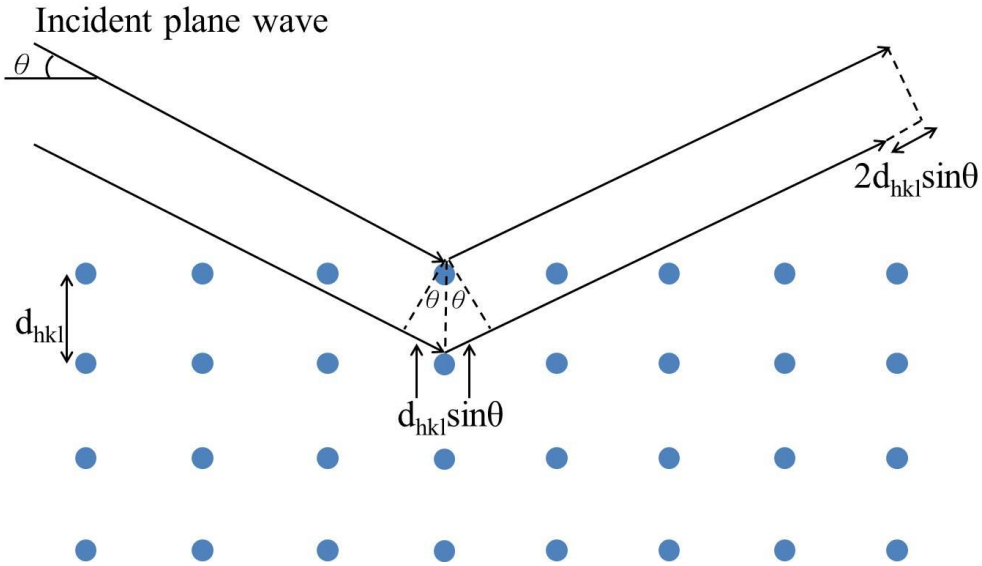

Figure 2.3 The schrmatic diagram of X-ray diffraction in crystal.

2.3.1.2. FE-SEM

In this work, the microstructure of ceramics, such as morphologies and crystalline grain size, were examined by an FE-SEM (JSM-6335F JEOL, Japan). A field-emission gun can produce high-energy electrons without heating the filament, and thus provide better resolution, minimum charging and damage of the sample. The electron beam is focused on the surface, interacting with the atoms and thus producing scattered electrons, back scattered electron and secondary electrons. A receiver is used to collect the secondary electrons that containing information of the surface topography for forming an image. The average grain sizes were determined by the measurements of 250 to 350 grains on the FE-SEM micrographs (x6000) using the linear intercept method.

2.3.1.3. Raman spectroscopy

Raman spectroscopy is a useful spectroscopic technique for detecting the vibrations in molecules based on the IR absorption and Raman scattering. It is widely used to obtain information of the chemical structure and physical form of a substance, and then to identify it. When light interacts with a material, photons may be absorbed or scattered. Absorption takes place only if the photon energy matches with the energy gap of the material. However, scattering is not limited by the energy levels. In scattering, photons are excited to a virtual level and immediately return to the ground level, releasing the energy in the form of scattered radiation. There are two kinds of scatterings: elastic and inelastic scattering. If photons do not hit the nucleus and no energy transfer is taken place, the scattering is regarded as elastic scattering or Rayleigh scattering. However, if nucleus is hit, energy transfer will take place, either from photons to molecules or vice versa. This is called Raman scattering. It is a very weak process because the probability of hitting the nucleus is very small, only one in every 10^6- 10^8 scatterings. The Raman spectroscopy then gives information of a substance by detecting the energy difference between the incident and scattered radiations, which correspond to the energy of vibration of the molecules.

For crystalline materials that atoms are linked by covalent bonds, the interaction with incident radiation induces two modes of vibrations, of which the full description are labeled as L_A, L_O, T_A, and T_O. L refers to the longitudinal mode in which the vibrations are along the radiation direction, while T refers to the transverse mode in which the vibrations are perpendicular to the radiation direction. The subscript A and O stand for acoustic and optical, respectively [85].

In this study, Raman spectra of the ceramics were measured by a grating spectrometer (Jobin-Yvon Horiba HR800, France) using the 488-nm line of an Ar ion laser as the excitation source. In the measurement, the laser beam was focused to form a small spot of diameter ~1 μm on the sample surface so as to study the local information of the sample.

2.3.2. PL characterization

The PL properties of the RE-doped BNBT ceramics, including PL and PLE were measured by a commercial PL spectrometer (FLSP920, Edinburgh Instruments, UK). A photograph of the spectrometer is given in Fig. 2.4.

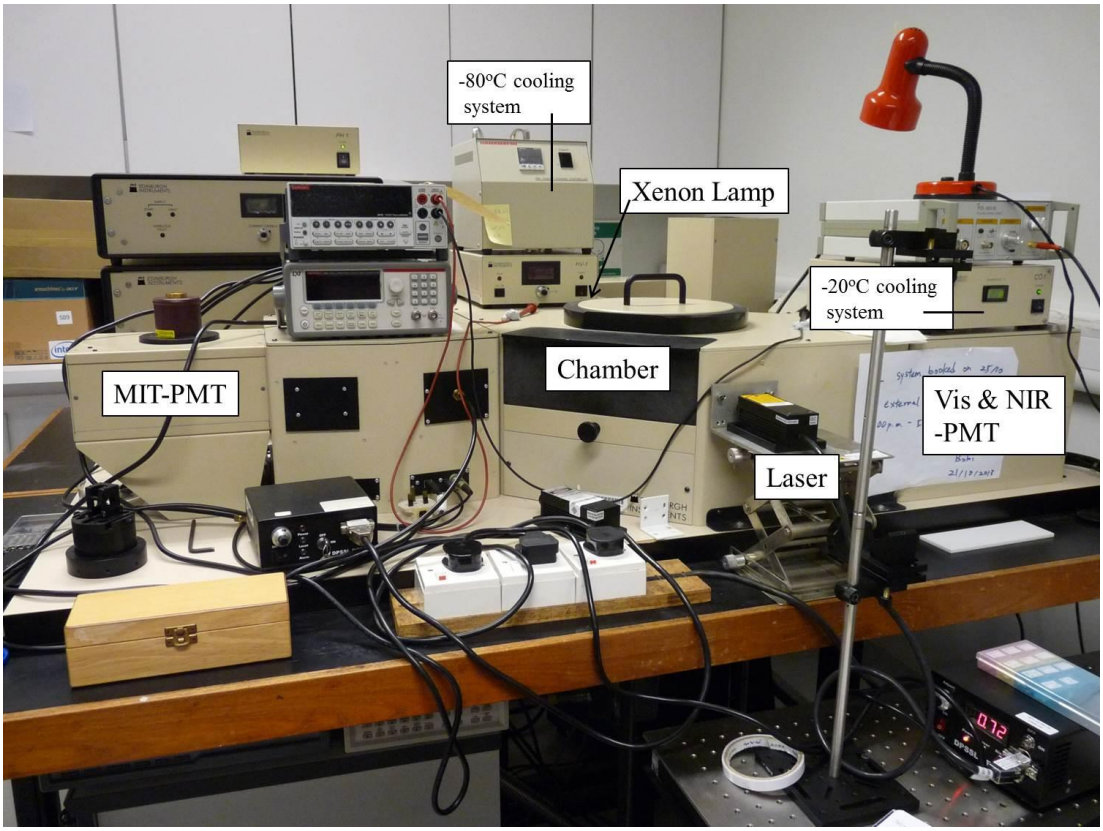

Figure 2.4 Photograph of the PL spectrometer system.

The spectrometer is made up of several detectors and controllers. The components employed in this study are listed below:

I. A continuous 980-nm diode laser (MDL-III, CNI Optoelectronics Tech. Co., China) with a maximum power output of 2 W. It is used as an excitation source for visible up-conversion (UC) PL , down-conversion (DC) (near-infrared) NIR and mid-infrared (MIR) emissions

II. A 450-W steady state xenon arc lamp (Xe900) equipped with ozone generating lamp emits radiation from 200 nm to 2.6 μm. It is used as an excitation source for DC PL and PLE measurements.

III. A red sensitive photomultiplier tubes (PMT) for the measurement of PL spectra from 200 nm to 900 nm.

IV. A NIR PMT for the measurement of PL spectra from 400 nm to 1.7 μm.

V. A MIR PMT for the measurement of PL spectra 2.0 to 3.0 μm.

VI. Peltier-cooled housings for keeping the temperature of the PMT at -20^{o}C, in order to reduce dark noise during the measurement.

VII. A cooling system for keeping the temperature of the NIR PMT at -80^{o}C, in order to reduce dark noise during the NIR measurement.

VIII. A voltage source (2410 1100V Source meter, Keithley Instruments Inc., US) is used to apply ext. E-field for investigate the E-field dependent PL properties.

Fig. 2.5 shows the photograph of the chamber of the PL spectrometer system. The sample holder in the middle of the chamber is free to rotate. During the measurement, the sample was irradiated by the excitation source (either the Xeonon lamp or laser), and the scattered radiation was directed to the PMT by reflection for detection. This setting is aimed to protect the PMT from damage by the excitation source.

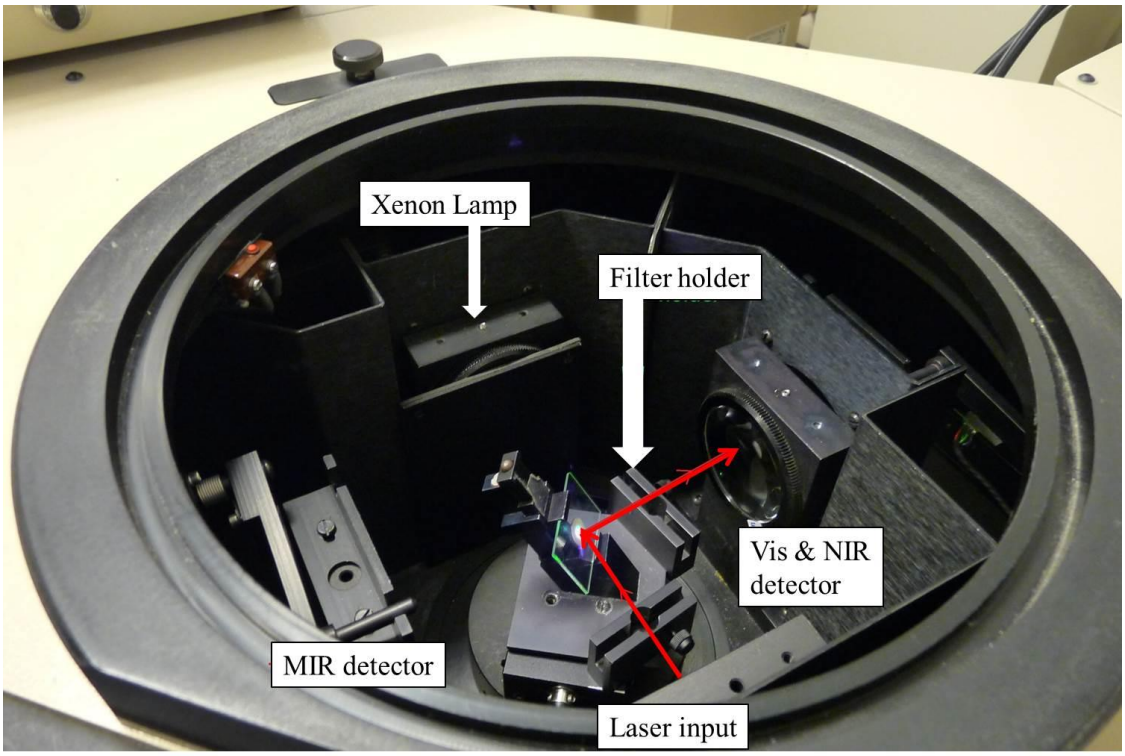

Figure 2.5 Photograph of the chamber of the PL spectrometer system.

2.3.3. Electrical characterization

2.3.3.1. Dielectric measurement

The dielectric properties of the ceramics such as ε_r and *tan* δ were measured at 1 kHz and room temperature. A precision impedance analyzer (HP 4294A, Agilent Technologies Inc., Palo Alto, CA) was used to measure the capacitance (C) and *tan* δ of the samples, from which ε_r was calculated as follows:

$$C = \frac{\varepsilon_0 \varepsilon_r A}{t} \tag{3.2}$$

where ε_0 is the permittivity of vacuum (~8.85×10^{-12} F/m), *A and t are* the electroded area and thickness of the sample. ε_r can be expressed as $\varepsilon_r = \varepsilon_r' - i\varepsilon_r''$, where ε_r' and $i\varepsilon_r''$

are the real and imaginary parts of the relative permittivity, respectively. *tan* δ is then given as:

$$\tan\delta = \frac{\varepsilon_r''}{\varepsilon_r'} \tag{3.3}$$

Besides, ε_r and *tan* δ were also measured as a function of temperature. A Carbolite furnace was used to increase the temperature from 25°C to 480°C. The ceramic sample was placed in a holder and connected to an impedance analyzer (HP 4194A, Agilent Technologies Inc., Palo Alto, CA) for the measurement of C and *tan* δ. The impedance analyzer was connected to a computer and controlled by a LabView program. The sample temperature was measured using a thermocouple together with a Keithley multimeter. The schematic diagram of the experimental setup is shown in Fig. 2.6.

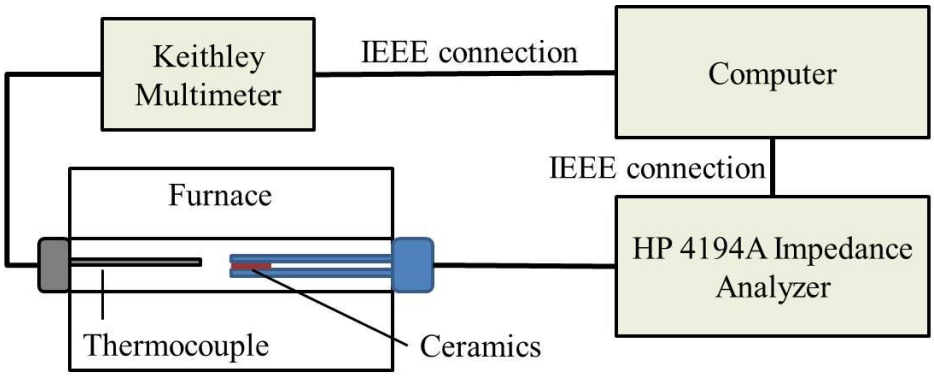

Figure 2.6 The schematic diagram of the experimental setup for measuring dielectric properties in function of temperature.

2.3.3.2. Piezoelectric measurement

The piezoelectric properties of the RE^{3+}-doped BNBT ceramic was measured by a piezo d_{33} meter (model ZJ-3D, Beijing Institute of Acoustic, China). The ceramic sample was placed between two probes of the piezo d_{33} meter and vibration was

triggered. Surface charge was then generated by direct piezoelectric effect and measured by the piezo d_{33} meter directly.

2.3.3.3. Ferroelectric measurement

In ferroelectric materials, the relationship between applied E-field and (net) polarization can be illustrated by PE loop. Many important ferroelectric properties can be determined from the PE loop, such as spontaneous polarization (P_s), saturation polarization (P_{sat}), remnant polarization (P_r) and coercive field (E_c). In this study, the PE loop of the ceramics were measured by a modified Sawyer-Tower circuit [86]. The schematic diagram of the experimental setup is shown in Fig. 2.7. In the measurement, a reference capacitor was used to collect the charges generated by the sample under the electric field. For neglecting the voltage drop at it in the calculation of the electric field applied to the sample, the capacitance of the reference capacitor (C_F) was chosen at least 1000 times smaller than that of the ceramic sample (C_R). The ceramic sample was immersed in silicone oil during the experiment to prevent electrical breakdown. A 100-Hz alternative-current (ac) voltage was generated by a function generator (HP 8116A) and amplified for 2000 times using an amplifier (Trek 609D-6). The voltage across the reference capacitor V_o was measured by a digital oscilloscope (HP 54645A), and the polarization P was then calculated as:

$$P = \frac{C_R V_o}{A} \tag{3.4}$$

where A is the area of the ceramic sample.

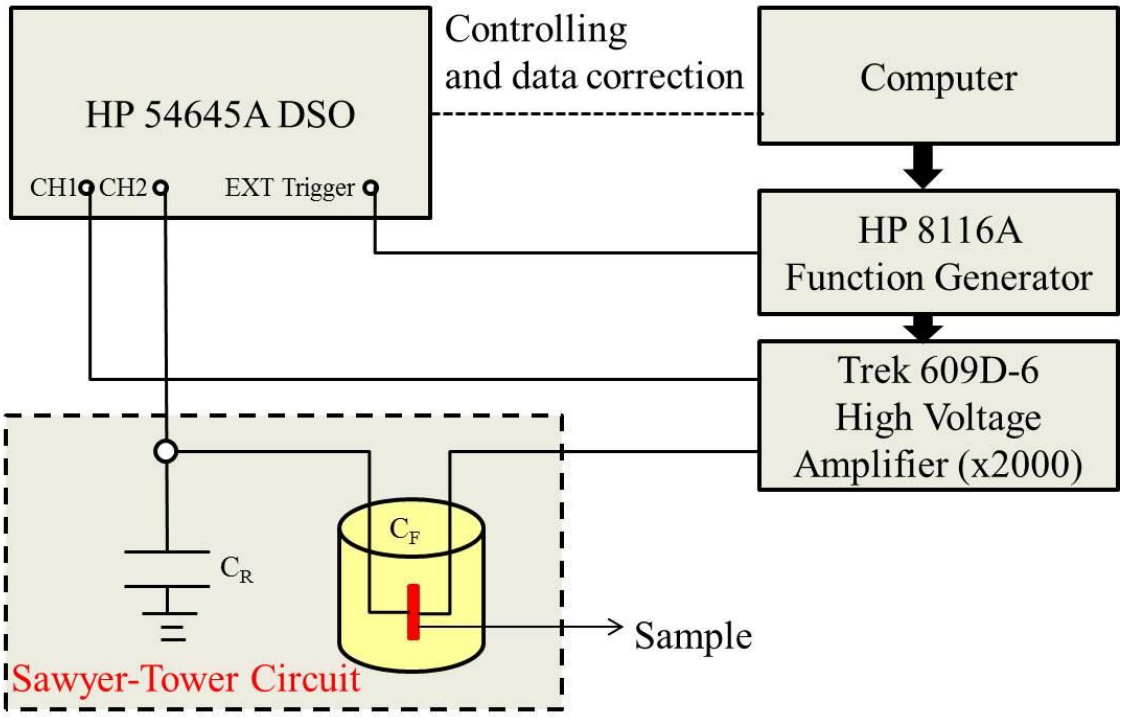

Figure 2.7 The schematic diagram of the experimental setup for the PE loop measurement.

Chapter 3. Er^{3+}-doped BNBT ceramics at various sites

3.1. Introduction

As discussed in Chapter 1, there are numerous research works of developing new multifunctional materials possessing both the photoluminescence (PL) and ferroelectric properties. The effects of rare-earth (RE) dopants and the resulting oxygen vacancies (V_o) on PL properties have been extensively investigated. It has been shown that, because of the trapping of electrons to lower energy levels and terminating the PL emissions via non-radiative transitions, the luminescent materials containing V_o generally exhibit weaker emissions. [87][88][89]. However, there is little discussion of the effects of cation vacancies (V_c). In most of the works, there are almost no comparisons of samples with either type of vacancies directly to those with no vacancies, and their focuses are mainly on the visible PL emissions. In this chapter, $0.93(Bi_{0.5}Na_{0.5}TiO_3)$-$0.07(BaTiO_3)$ ceramics doped with 0.01 mol Er^{3+} at various sites have been fabricated, and the effects of the resulting vacancies, including both V_o and V_c, have been investigated. The samples are abbreviated as BNBT-Er(y), where y is Bi, Ti, Ba or Na for denoting the ions replaced by Er^{3+}. Un-doped BNBT, i.e., BNBT-Er(y) with y = 0, ceramic has also been fabricated for comparison purposes. The reason for choosing BNBT as the host material is not only the numerous ions for substitution but also its composition near the morphotropic phase boundary (MPB) [68]. As compared to

BNT, BNBT ceramics exhibit better piezoelectric and ferroelectric properties, giving higher piezoelectric constant (d_{33}) (180 pC/N vs 70 – 80 pC/N) [75], electromechanical coupling factor (k_p) (37% vs 16%) [67], remnant polarization (P_r) (16.4 μC/cm^2 vs 2.55 μC/cm^2) [76] and lower coercive field (E_c) (3.41 kV/mm vs 5.69 kV/mm) [67]. Besides, there are four sites for doping Er^{3+} and thus either V_o or V_c may be formed, depending on the charge difference from the ion being replaced for retaining the charge neutrality [90]. V_o is formed in the BNBT-Er(Ti) ceramics whereas V_c is formed in the BNBT-Er(Ba) and BNBT-Er(Na) ceramics. Owing to the different valence states (+1 vs +2), the number of V_c in the BNBT-Er(Na) ceramics should be twice of that in BNBT-Er(Ba). On the other hand, because of the same valence state, no vacancies will be formed in the BNBT-Er(Bi) ceramics.

The optimum sintering temperature for obtaining dense BNBT-Er(y) ceramics has been determined as 1200^{o}C. The PL properties of the ceramics, including the visible up-conversion (UC), near-infrared (NIR) and mid-infrared (MIR) down-conversion (DC) emissions have been systemically investigated. The effects of the vacancies on the PL intensity have been studied and the corresponding PL mechanisms and energy transfer (ET) processes have been deduced. As a type of ferroelectric ceramics, the dielectric, piezoelectric and ferroelectric properties of the BNBT-Er(y) ceramics have also been studied.

3.2. Structural properties

3.2.1. XRD

The XRD patterns of the BNBT-Er(y) ceramics, in crushed fine powder form, are shown in Fig. 3.1. The results, in particular for the BNBT-Er(0), are consistent with those published elsewhere [91][92]. All the ceramics possess a perovskite structure, and no secondary impurity phase is observed, indicating that Er^{3+} has diffused into and entered the corresponding sites of BNBT lattices successfully. A splitting of the (002)/(200) peaks at 46.6^{o} is observed for all ceramics. This suggests that all the ceramics reside near the MPB, containing both the rhombohedral and tetragonal phases.

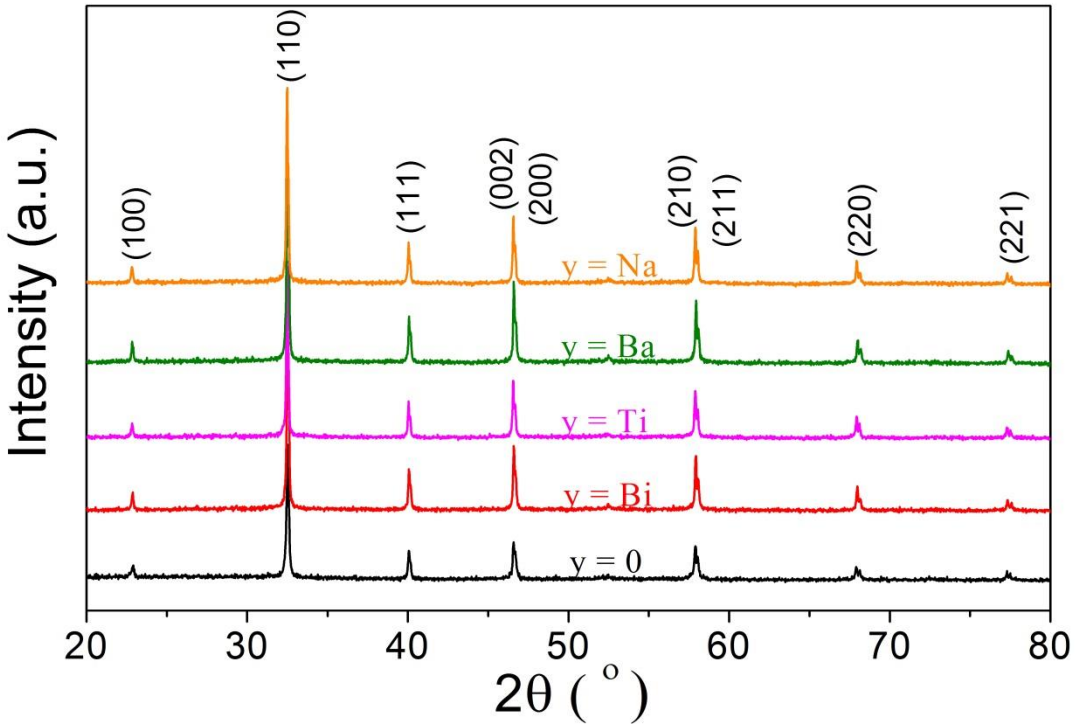

Figure 3.1 XRD patterns of the BNBT-Er(y) ceramics.

3.2.2. FE-SEM

The FE-SEM micrographs of the BNBT-Er(y) ceramics are shown in Fig. 3.2. All ceramics possess a well-sintered and dense structure. The average grain sizes of the ceramics are given in Table 3.1. After the doping of Er^{3+} (at any sites), the average grain size decreases from 1.07 μm to 0.90 - 0.84 μm, or by 16 to 21%. This should be attributed to the inhibition of grain growth caused by the Er^{3+}-doping. As shown in Fig. 3.2, the grain size distribution is non-uniform. Similar to the previous works on Dy^{3+}-doped BT and BNT ceramics, this should be attributed to the relatively large size of the starting powders [93][94].

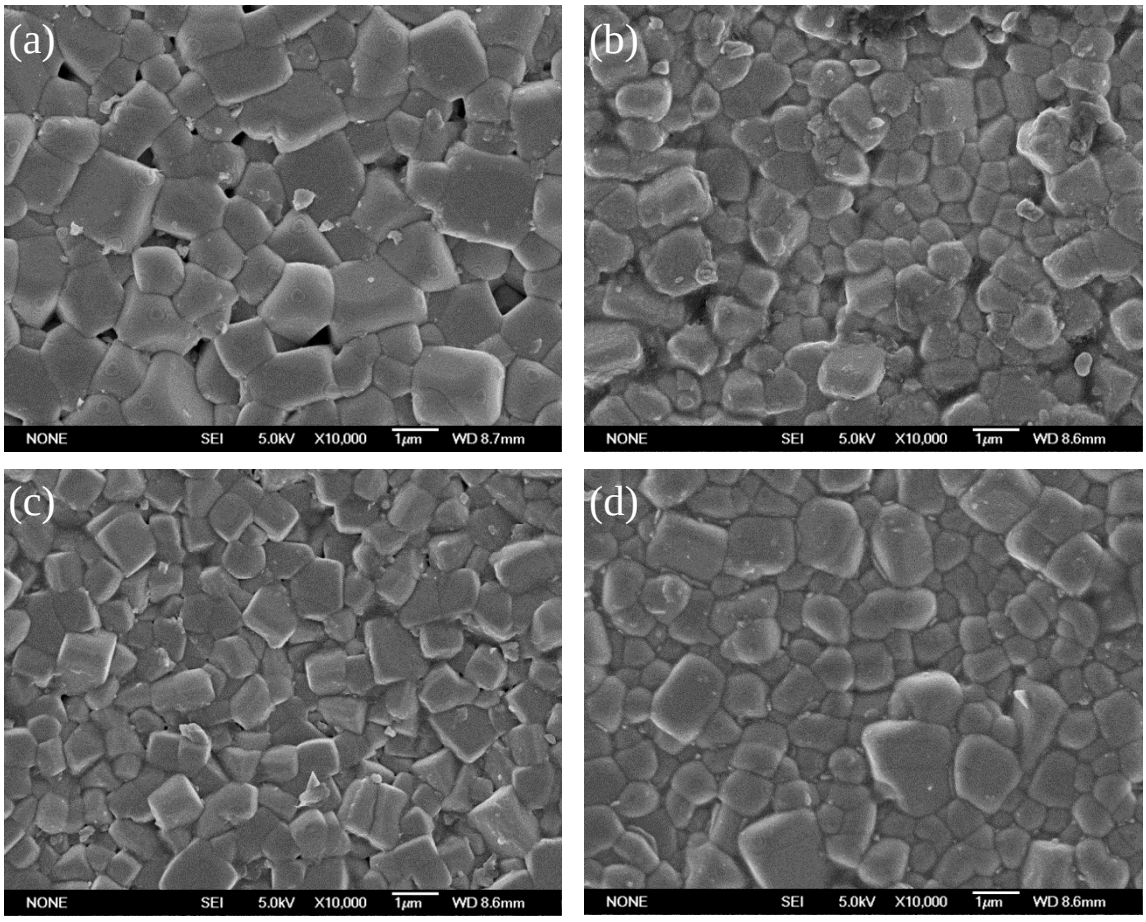

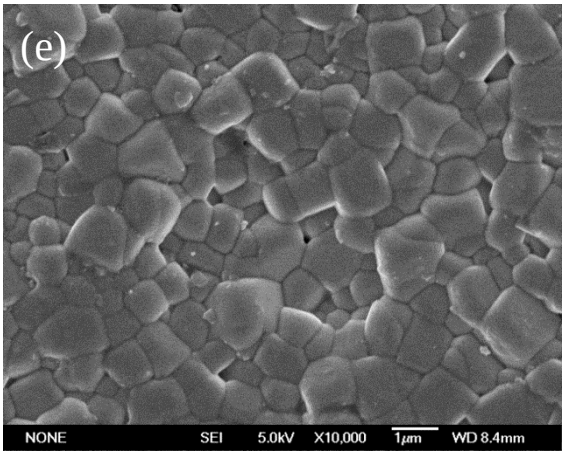

Figure 3.2 FE-SEM micrographs of the BNBT-Er(y) ceramics: (a) y = 0, (b) y = Bi, (c) y = Ti, (d) y = Ba and (e) y = Na.

Table 3.1 Average grain sizes of the BNBT-Er(y) ceramics.

y	**0**	**Bi**	**Ti**	**Ba**	**Na**
grain size (μm)	1.07	0.87	0.84	0.84	0.90

3.2.3. Raman spectroscopy

According to Eerd et al. [95] and Parija et al. [68], BNBT ceramics with rhombohedral structure will exhibit 5 Raman-active modes in the range of 100 to 1000 cm^{-1}, due to the distorted octahedral clusters. The first Raman-active mode is A1 (TO1), which locates at ~146 cm^{-1} and is related to the distorted octahedral [BiO_6] and [NaO_6] clusters. The second mode is E (TO2) mode which locates at ~279 cm^{-1} and is related to the octahedral [TiO_6] clusters. The third Raman-active mode ((LO2) mode) is generally weak and unobvious because it is related to the short-range electrostatic forces of the lattice ionicity. The forth mode locates at ~ 542 cm^{-1} and is called (TO3), which is related to the stretching symmetric vibrations of the [TiO_6] clusters. The last mode is

(LO3) mode at 812 cm^{-1} which is related to the distorted octahedral [TiO_6] clusters in the rhombohedral structure.

The Raman spectra of the BNBT-Er(y) ceramics are shown in Fig. 3.3. All the ceramics show the characteristic peaks at 141 cm^{-1} (A1(TO1) mode), 283 cm^{-1} (E(TO2) mode), 546 and 602 cm^{-1} ((TO3) mode) and 800 cm^{-1} ((LO3) mode), which are consistent with the results of Parija et al. [68]. It should be noted that the (TO3) mode has split into two bands at 546 cm^{-1} and 602 cm^{-1}. The splitting indicates the coexistence of the rhombohedral and tetragonal phases, confirming that the ceramics reside near the MPB (Fig. 3.1). It has also been observed that the peaks become broadened after the doping of Er^{3+}. This should be attributed to the different valence states of the ions, which causes the formation of vacancies and thus deteriorates the crystallinity [88]. It is also expected that the different valence states of Na^{+}, Ba^{2+} and Ti^{4+} would cause different numbers of vacancies, such that the number of vacancies in the BNBT-Er(Na) ceramic should be double of those in the BNBT-Er(Ba) and BNBT-Er(Ti) ceramics [90]. Due to the larger number of defects in the lattices, the BNBT-Er(Na) ceramic has the lowest crystallinity, and thus exhibits the broadest characteristic peaks in the Raman spectra.

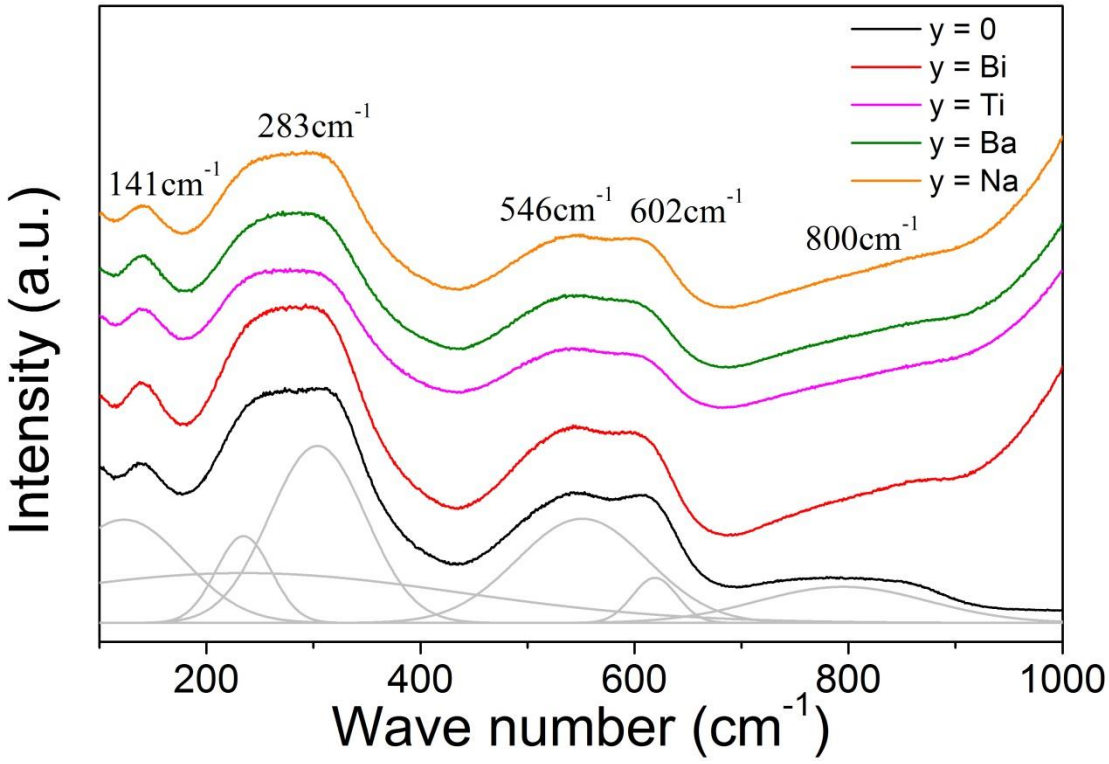

Figure 3.3 Raman spectra of the BNBT-Er(y) ceramics.

3.3. PL properties

The visible UC, NIR and MIR DC emission spectra of the BNBT-Er(y) ceramics are shown in Fig. 3.4 - 3.6 respectively. Under an excitation of 980 nm, the visible emission for all the ceramics is very strong such that a bright green spot can be easily observed on the irradiated surfaces. All the BNBT-Er(y) ceramics show three characteristic emission bands at 512 – 536 nm (green), 536 – 569 nm (green), and 640 – 681 nm (red), respectively (Fig. 3.4). They are attributed to the transitions $^{2}H_{11/2} \rightarrow {}^{4}I_{15/2}$, $^{4}S_{3/2} \rightarrow {}^{4}I_{15/2}$ and $^{4}F_{9/2} \rightarrow {}^{4}I_{15/2}$, respectively (Fig. 3.7). Besides, as shown in Fig. 3.5 and 3.6, all the ceramics exhibit a broad NIR emission band in the range of 1.44 to 1.66 μm

and a broad MIR emission band in the range of 2.62 to 2.84 μm. The emissions are attributed to the transitions $^4I_{13/2} \rightarrow {}^4I_{15/2}$ and $^4I_{11/2} \rightarrow {}^4I_{13/2}$, respectively (Fig. 3.7).

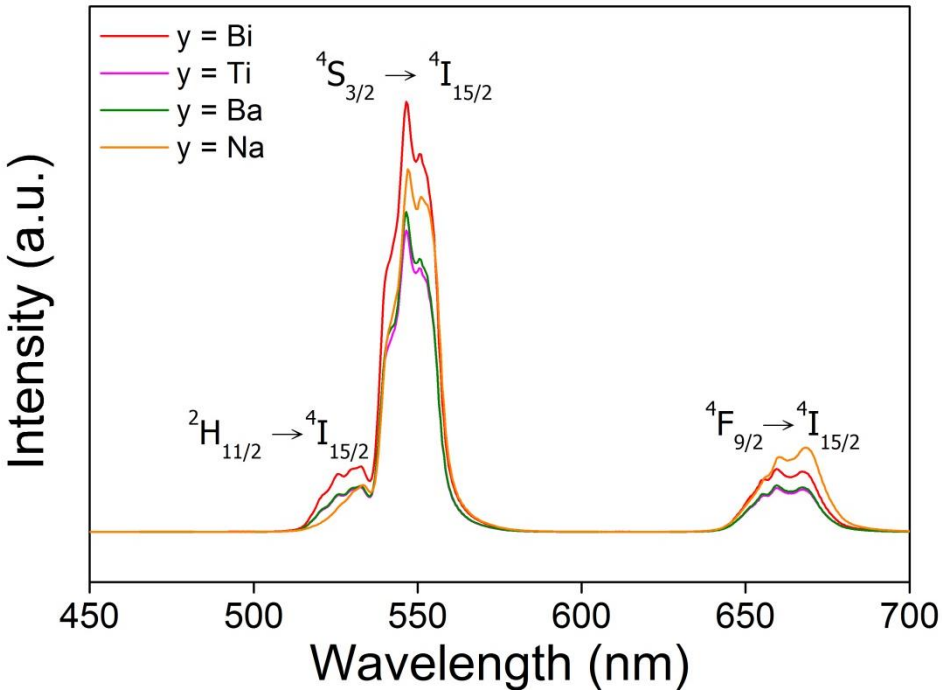

Figure 3.4 Visible UC emission spectra of the BNBT-Er(y) ceramics.

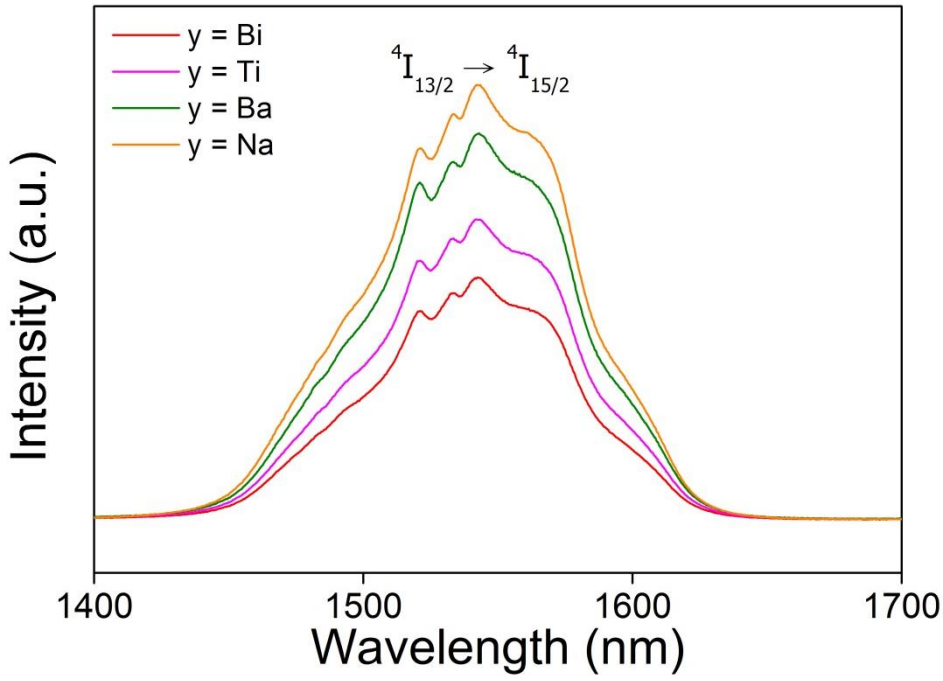

Figure 3.5 NIR DC emission spectra of the BNBT-Er(y) ceramics.

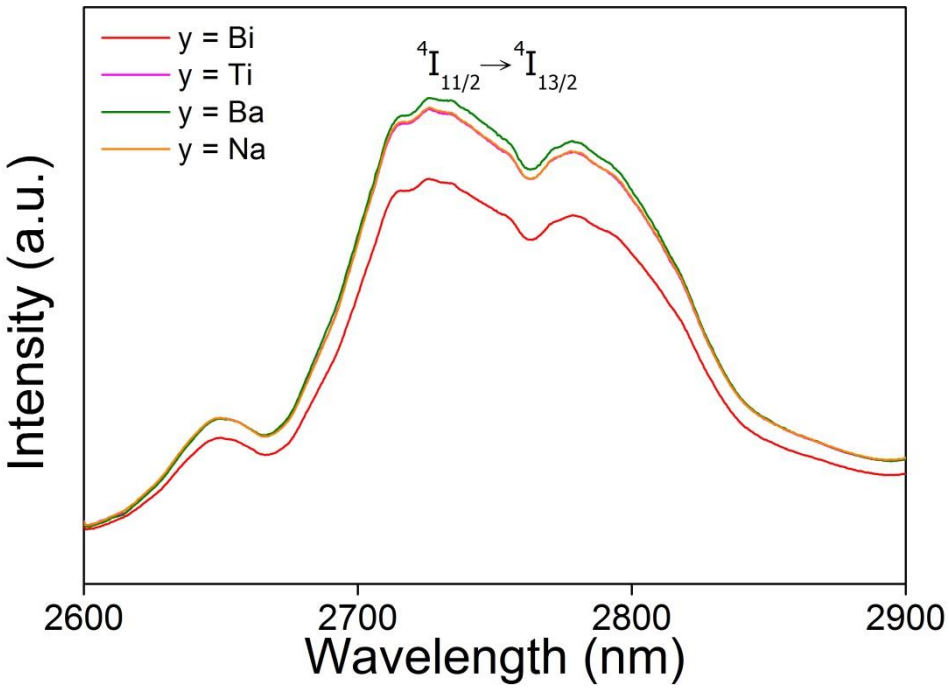

Figure 3.6 MIR DC emission spectra of the BNBT-Er(y) ceramics.

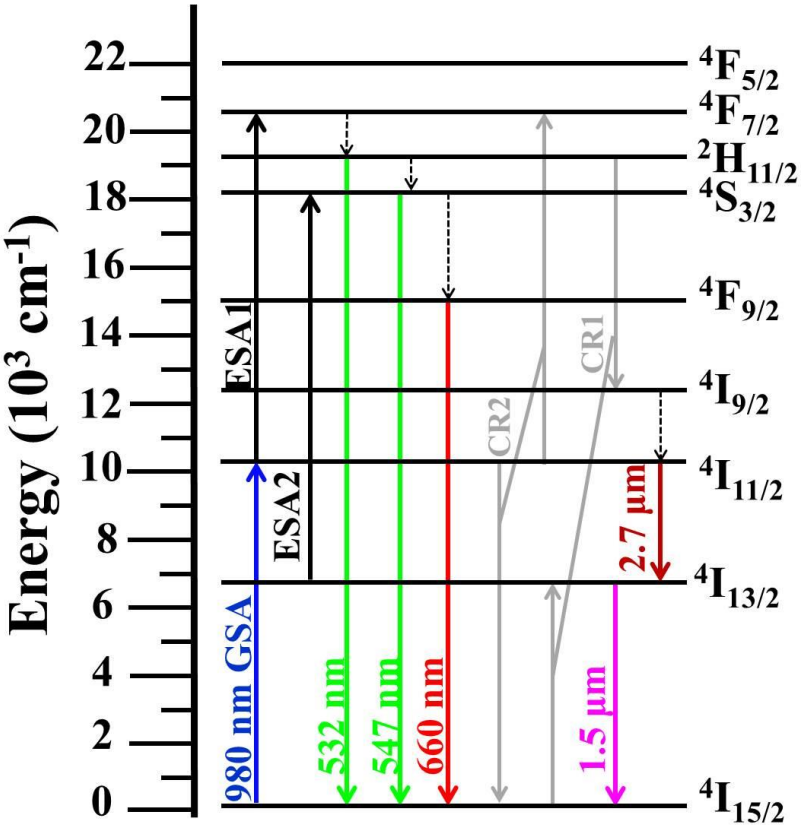

Figure 3.7 Schematic diagram for the PL mechanism of Er^{3+} under an excitation of 980 nm.

3.3.1. PL mechanism

As illustrated in Fig. 3.7, electrons are first excited by the 980-nm photons to the $^4I_{11/2}$ level through the ground state absorption (GSA). Some of the excited electrons may be further excited to the $^4F_{7/2}$ level through the excited state absorption (ESA1). The excited electrons will then relax non-radiatively to the $^2H_{11/2}$, $^4S_{3/2}$ and $^4F_{9/2}$ levels subsequently via multi-phonon relaxation (MPR), followed by the radiative relaxation to the $^4I_{15/2}$ ground level and thus the production of the green and red UC emissions, respectively (Fig. 3.4). Probably due to the fast relaxation rate resulting from the small energy gap, the population of the $^2H_{11/2}$ level is low, and hence the green emission at 532 nm is much weaker than that at 547 nm. On the other hand, due to the large energy gap and then low relaxation rate, the population of the $^2F_{9/2}$ level is also low and the red emission is relatively weak. In general, for the ceramics with low concentrations of Er^{3+} (e.g., $\leqq$ 0.01 mol), the cross relaxation (CR) processes (such as CR1 and CR2 shown in Fig. 3.7) are not efficient and hence will not occur for the UC process. Some of the excited electrons on the $^4I_{11/2}$ level relax radiatively to the $^4I_{13/2}$ level and then to the $^4I_{15/2}$ ground level, producing the NIR and MIR DC emission (Fig. 3.5 and 3.6), respectively.

3.3.2. Effects of vacancies on PL properties

The integrated PL intensities of the green (507 – 580 nm), red (635 – 695 nm), NIR (1.44 - 1.66 μm) and MIR (2.62 - 2.84 μm) emission bands of the BNBT-Er(y) ceramics have been evaluated and are compared with those of the BNBT-Er(Bi) ceramic in Fig. 3.8. Because of the same valence states of Bi^{3+} and Er^{3+}, there should be no vacancies formed in the BNBT-Er(Bi) ceramic. On the other hand, owing to the charge imbalance, the BNBT-Er(Na) and BNBT-Er(Ba) ceramics contain V_c after the substitution for Na^{1+} and Ba^{2+}, respectively, while the BNBT-Er(Ti) ceramic contains V_o because of the Ti^{4+}-substitution. It is also suggested that the number of vacancies is dependent on the difference in the valence states. That is, the number of V_c in the BNBT-Er(Na) ceramics should be twice of that in the BNBT-Er(Ba), while the BNBT-Er(Ba) and BNBT-Er(Ti) ceramics should have the same amount of vacancies, indeed of opposite polarities. As shown in Fig. 3.8, the observed integrated PL intensities of the green and red emission bands generally decrease while those of the NIR and MIR emission bands increase for the ceramics containing either V_c or V_o. Both V_c and V_o are kinds of defects in the lattices that can deteriorate the crystallinity of ceramics, and thus affecting the probabilities of MPR, CR as well as radiative transitions [88][96]. As a result, most of the excited electrons relax non-radiatively to the lower energy levels and then contribute to the NIR and MIR emissions, at the expense of the UC visible emissions.

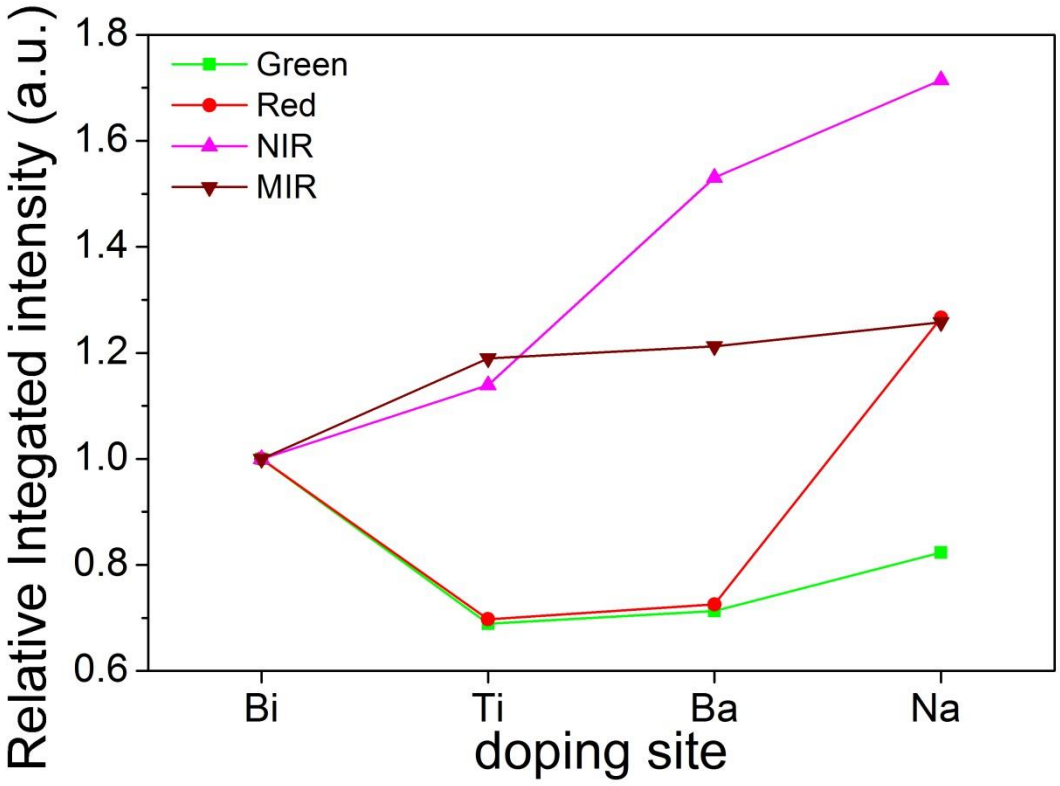

Figure 3.8 Variations of the relative integrated intensities of the green, red, NIR and MIR emissions with y for the BNBT-Er(y) ceramics

It has been shown that V_o have a lower energy level, which locates about 10,000 cm^{-1} below the bottom of the conduction band of the ceramic [97]. For the BNBT-Er(Ti) ceramic, it is reasonable to estimate that the energy level of V_o should locate in lower level of the energy level diagram of Er^{3+}. Therefore, V_o are considered as quenchers, which can trap the excited electrons to lower energy levels and complete the transition through other transition routes [87][88][98]. On the other hand, V_c are regarded as non-radiative recombination centers (NRCs) [99][100], which increase the probabilities of CR1 and CR2. The population of the $^4I_{13/2}$ level thus increases as a looping mechanism is established between the $^4F_{7/2}$, $^2H_{11/2}$, $^4I_{9/2}$ and $^4I_{11/2}$ levels [23]. As a result, the observed

integrated intensities of all the emission bands for the BNBT-Er(Ba) ceramic are higher than those for the BNBT-Er(Ti) ceramic, especially for the intensity of NIR emission band (about 40%) (Fig. 3.8). Obviously, similar to the effects of V_o, the looping mechanism decreases the green and red emissions owing to the lower populations of the corresponding energy levels.

Apparently, due to the larger amount of V_c, the population of the $^4I_{13/2}$ level for the BNBT-Er(Na) ceramic should be higher than that for the BNBT-Er(Ba), and thus giving a stronger emission in NIR region. However, it is interesting to note that there are also increases in the observed integrated intensity of the green and red emission band for the BNBT-Er(Na) ceramics (Fig. 3.8). These should be due to the further enhancement of CRs. As the population of the $^4I_{13/2}$ level is increased by enhanced CR1, some of the excited electrons are excited back to the $^4S_{3/2}$ level via ESA2 [101]. However, probably due to the enhanced MPR, most of them will not relax radiatively to give green emission. Instead, they will relax non-radiatively to the $^4F_{9/2}$ level and then radiatively to the $^4I_{15/2}$ ground level, and thus giving a (relatively) larger enhancement in the red emission as compared to that in the green emission. Although the red emission of all the ceramics are weak (as compared with the green emission), it is noted that the red emission of the BNBT-Er(Na) ceramic (with more V_c) is even stronger than that of the BNBT-Er(Bi) ceramic.

3.4. Electrical properties

3.4.1. Dielectric and piezoelectric properties

Fig. 3.9 shows the temperature dependences of dielectric constant (ε_r) and dielectric loss (*tan* δ) measured at 1 kHz, 10 kHz and 100 kHz for the BNBT-Er(0) ceramic. Similar to the results published elsewhere [75], the transition peak is broad and frequency dependent, confirming the relaxor-like characteristics of the ceramic. However, probably due to a slightly change in composition arisen from the fabrication processes, the depolarization temperature (T_d), which can be determined as the first inflection point (or peak) in the *tan* δ-temperature curve [102], cannot be observed in the temperature range studied. This suggests that the ceramic may possess a low T_d, e.g., < 25°C, and thus exhibits relaxor-like characteristics at room temperature and gives a high ε_r (1813 at 1 kHz) at room temperature.

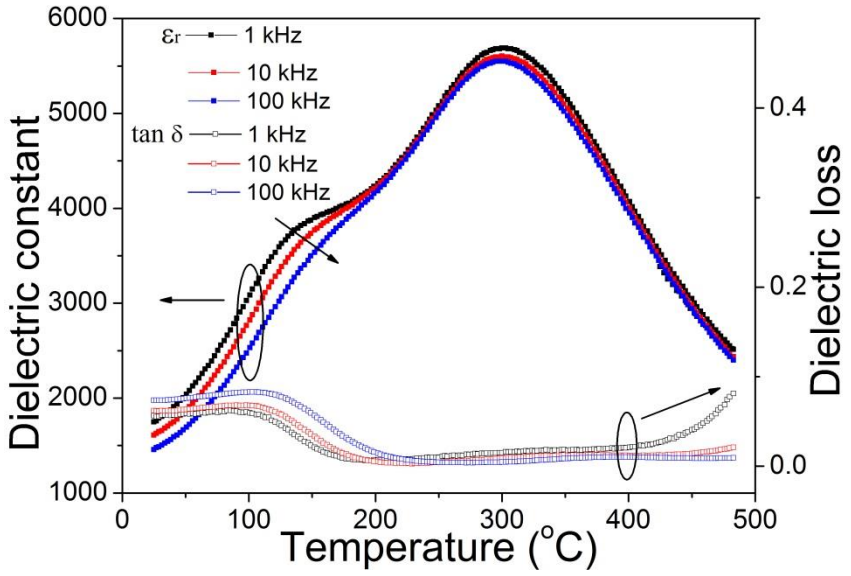

Figure 3.9 Temperature dependences of ε_r and *tan* δ measured at 1 kHz, 10 kHz and 100 kHz for the BNBT-Er(0) ceramic.

Fig. 3.10 shows the temperature dependences of the observed ε_r and *tan* δ (measured at 100 kHz) for the BNBT-Er(y) ceramics, while their values measured at 1 kHz and room temperature are listed in Table 3.2. After the doping of Er^{3+} (at any sites), the transition peak becomes further broadened and the observed ε_r in the whole temperature range decreases. This should be attributed to the disruption of the long-range ferroelectric order by the Er-doping, which is similar to the previous work on KNN-modified BNT-BT ceramics [103]. It can also be seen that the vacancies had further deteriorated the dielectric properties, whereas the effects of the cation vacancies are higher and dependent on the number of the vacancies. These should be partly attributed to the lower crystallinity[88][104][105]. On the other hand, the Er-doping improves the leakage of the ceramics, giving a smaller *tan* δ for all the doped ceramics (Table 3.2).

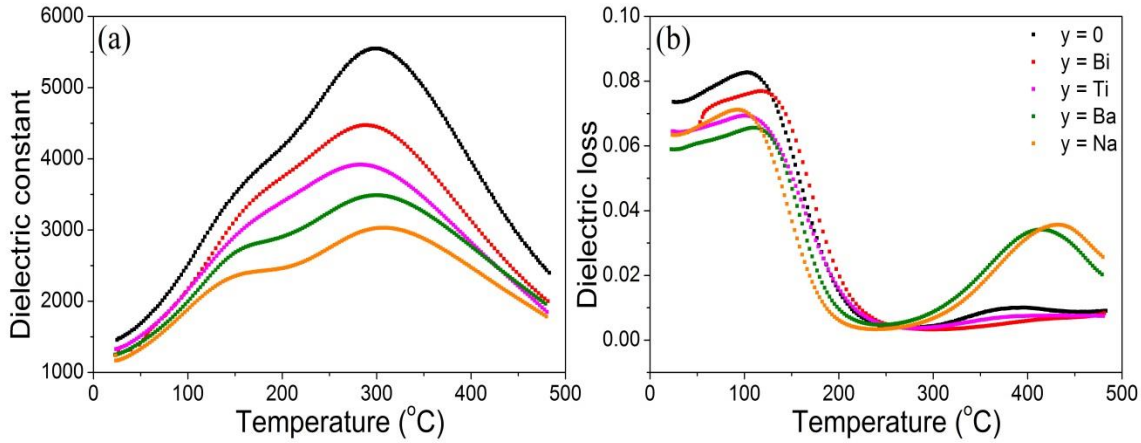

Figure 3.10 Temperature dependence of (a) ε_r (b) *tan* δ measured at 100kHz for the BNBT-Er(y) ceramics

The observed d_{33} of the BNBT-Er(y) ceramics are also listed in Table 3.2. After the doping of Er^{3+}, it decreases significantly from 194 pC/N to less than 30 pC/N,

depending on the doping sites. Similarly to ε_r, this should be attributed to the disruption of the long-range ferroelectric order by Er^{3+}-doping [103].

Table 3.2 Dielectric constant, dielectric loss, and piezoelectric constant of the BNBT-Er(y) ceramics

BNBT-Er(y)	ε_r @ 1kHz	tan δ@ 1kHz	d_{33} (pC/N)
0	1813	0.057	194
Bi	1616	0.050	27
Ti	1564	0.048	26
Ba	1485	0.045	13
Na	1596	0.049	8

3.4.2. Ferroelectric properties

Fig. 3.11 shows the ferroelectric hysteresis loops (PE loops) of the BNBT-Er(y) ceramics measured under an electric field of 5.5 kV/mm at 100 Hz. After the doping of Er^{3+}, the PE loop becomes further slanted, and the observed remanent polarization (P_r) decreases. These indicate that the ferroelectric properties are deteriorated, which should also be attributed to the disruption of the long-range ferroelectric order by Er^{3+}-doping [103]. According to the phenomenological theory, d_{33} is related to ε_r, the permittivity of vacuum ε_o, the spontaneous polarization P_s (which may be approximated by P_r) and the electrostrictive coefficient Q_{11} via a general equation $d_{33} = 2\varepsilon_o\varepsilon_r Q_{11} P_s$ [103]. The significant decrease in d_{33} of the doped ceramics should hence be partly attributed to the decreases in both ε_r and P_r.

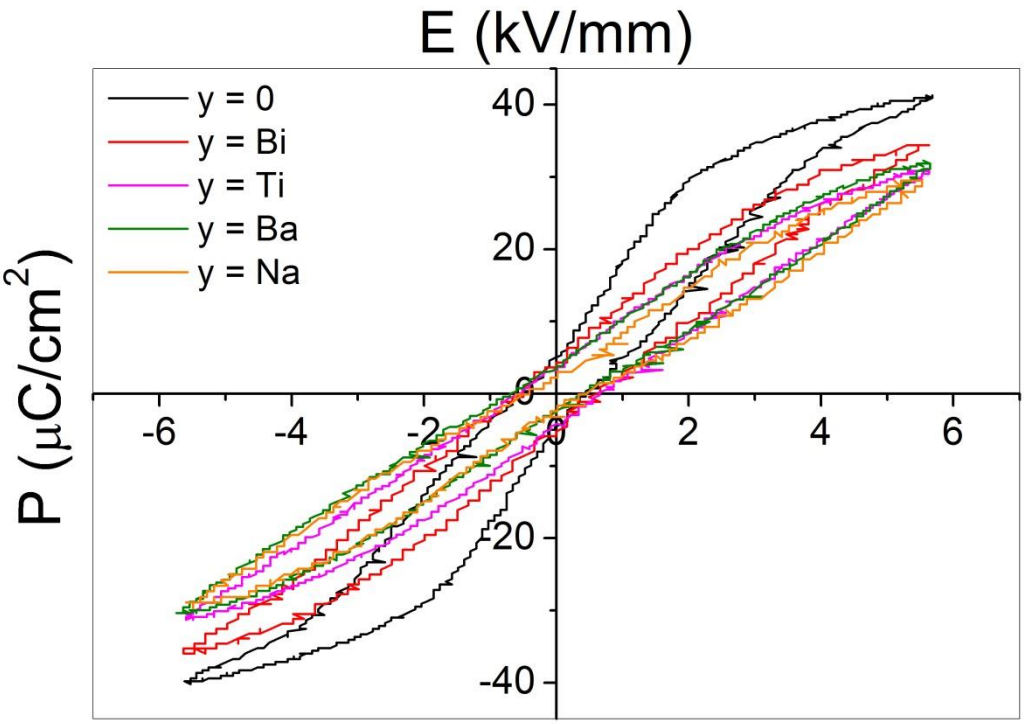

Figure 3.11 PE loops of the BNBT-Er(y) ceramics

3.5. Conclusion

BNBT-Er(y) photoluminescent ceramics have been fabricated and their PL and electrical properties have been studied. All the ceramics possess a single-phase perovskite structure, suggesting that Er^{3+} has diffused into the corresponding sites of the BNBT ceramics successfully. Under an excitation of 980 nm, the ceramics exhibit visible UC emissions at 532 nm (green), 547 nm (green) and 660 nm (red), as well as broadband NIR and MIR DC emissions in range 1.44 to 1.66 μm and 2.62 to 2.84 μm, respectively. Our results also reveal that the vacancies arisen from charge imbalance between the dopants and the replaced ions could increase the PL intensity of the NIR and MIR emission bands at the expense of the visible emissions. For the BNBT-Er(Ba)

ceramic containing V_c, a looping mechanism is established such that the PL intensity of the NIR emission band increases significantly by more than 50%. The resulting effects of the looping mechanism is stronger in the BNBT-Er(Na) ceramic which contains more V_c. The ceramics also exhibit good dielectric, ferroelectric and piezoelectric properties, and hence they should have great potentials in multifunctional optoelectronic applications.

Chapter 4. Er^{3+}-doped BNBT ceramics

4.1. Introduction

As discussed in Chapter 3, vacancies arisen from different oxidation numbers of the dopants and replaced ions would affect the photoluminescence (PL) properties by providing lower energy levels for alternative transitions or increasing the probability of non-radiative transitions. For minimizing the effects of vacancies, Bi^{3+} has been selected for being replaced by the dopants in the following studies. In this chapter, BNBT ceramics doped with various contents of Er^{3+} at the Bi-site have been prepared by the conventional solid state reaction (SSR) method. The ceramics have a chemical formula of $0.93(Bi_{0.5-x/0.93}Er_{x/0.93}Na_{0.5}TiO_3)$-$0.07(BaTiO_3)$ and are abbreviated as BNBT-xEr, with the molar fraction x varying from 0 to 0.07. The optimum sintering temperature has been determined as 1200°C. The aim of this work is to develop a multifunctional material with good electrical and PL properties. The effects of Er^{3+} on PL properties, including visible up-conversion (UC), near-infrared (NIR) and mid-infrared (MIR) down-conversion (DC) emissions, emission colors have been investigated, and the corresponding PL mechanisms have been discussed. The electrical properties, such as dielectric, piezoelectric and ferroelectric properties, of the ceramics have also been studied.

4.2. Structural properties

4.2.1. XRD

The XRD patterns of the BNBT-xEr ceramics, in crushed powder form, are shown in Fig. 4.1(a). All the ceramics possess a single-phase perovskite structure, suggesting that Er^{3+} has diffused into and entered the Bi^{3+} sites of the BNBT lattices. Fig. 4.1(b) shows the enlarged XRD patterns of the ceramics in the range of 2θ from 46° to 47.3°. A splitting of the (002)/(200) characteristics peaks is observed for all ceramics, indicating the coexistence of the rhombohedral and tetragonal phases. This confirms that the BNBT-xEr ceramics reside near the morphotropic phase boundary (MPB) [91][106]. As also shown in Fig. 4.1(b), the (002)/(200) characteristics peaks shift toward higher angles with increasing x (the Er^{3+}-concentration), indicating a shrinkage of the lattices. This should be attributed to to the smaller radius of Er^{3+} (1.22 Å , CN = 12) as compared to Bi^{3+} (1.32 Å , CN = 12) [87].

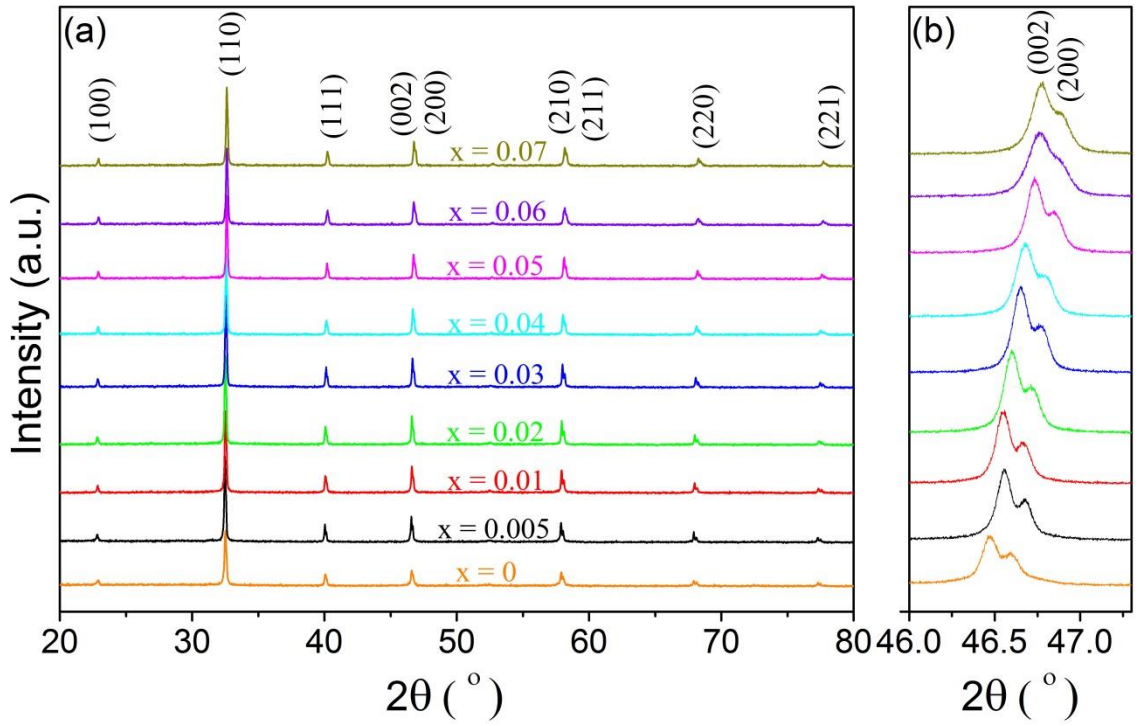

Figure 4.1 XRD patterns of the BNBT-xEr ceramics (a) from 20° to 80°, (b) 46° to 47.3°.

4.2.2. FE-SEM

Fig. 4.2 shows the FE-SEM micrographs of the BNBT-xEr ceramics. Pores are observed in the BNBT-0Er ceramic (Fig. 4.2a), while the Er-doped ceramics become well-densified (Fig. 4.2b-i). All the ceramics possess small grains, with a size ranging from 0.5 to 2 μm. The non-uniformity of grain size should be attributed to the relatively large starting powders as reported in some RE^{3+}-doped BT and BNT ceramics [93][94][107]. The average grain sizes of the ceramics are given in Table. 4.1. The average grain size of the BNBT-0Er ceramic is about 1.07 μm. After the doping of Er^{3+}, it decreases by 10-20% in most of the ceramics. The BNBT-0.07Er ceramic has the smallest grains, with an average size of 0.81 μm.

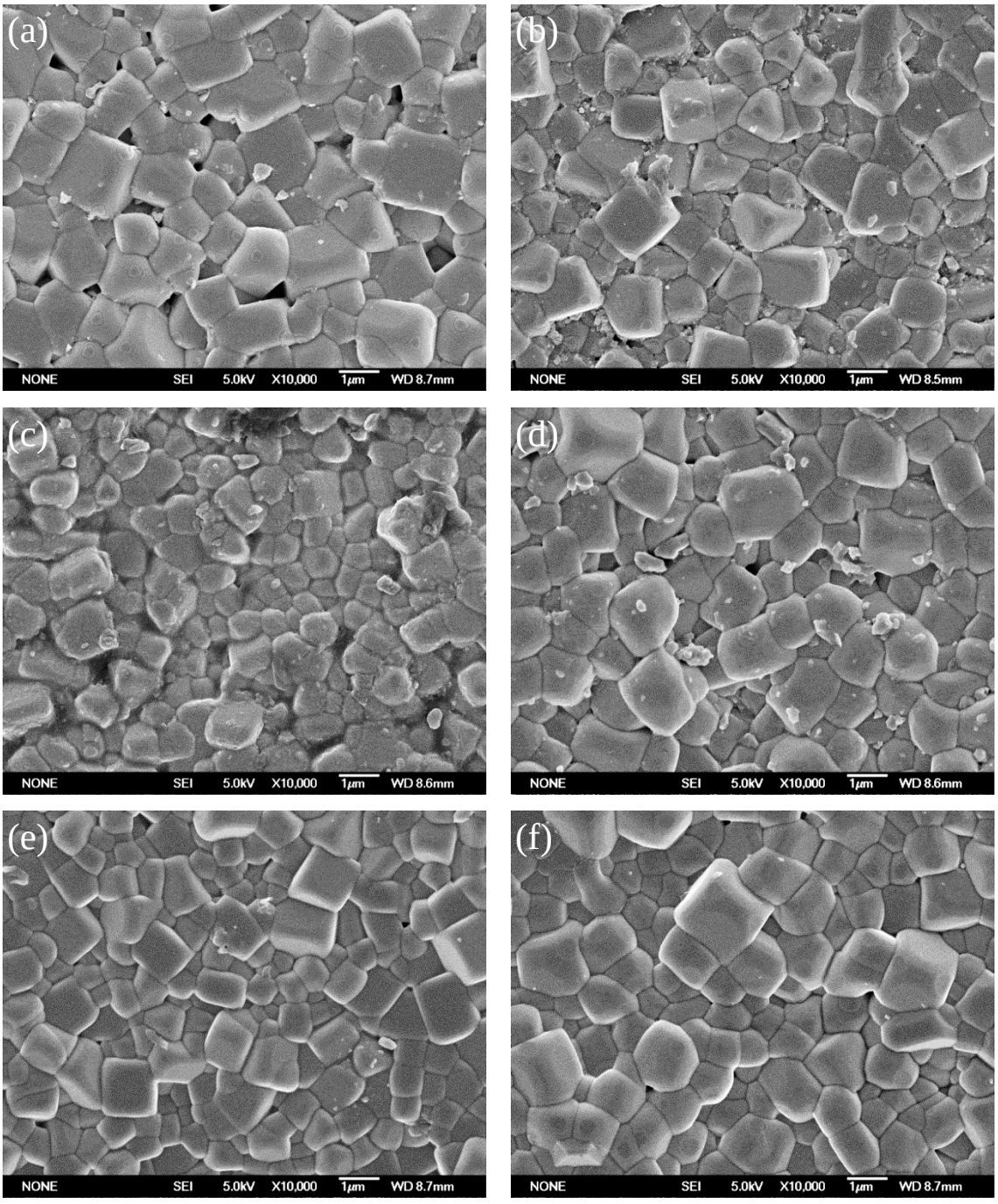
(a)
NONE SEI 5.0kV X10,000 1μm WD 8.7mm
(b)
NONE SEI 5.0kV X10,000 1μm WD 8.5mm
(c)
NONE SEI 5.0kV X10,000 1μm WD 8.6mm
(d)
NONE SEI 5.0kV X10,000 1μm WD 8.6mm
(e)
NONE SEI 5.0kV X10,000 1μm WD 8.7mm
(f)
NONE SEI 5.0kV X10,000 1μm WD 8.7mm

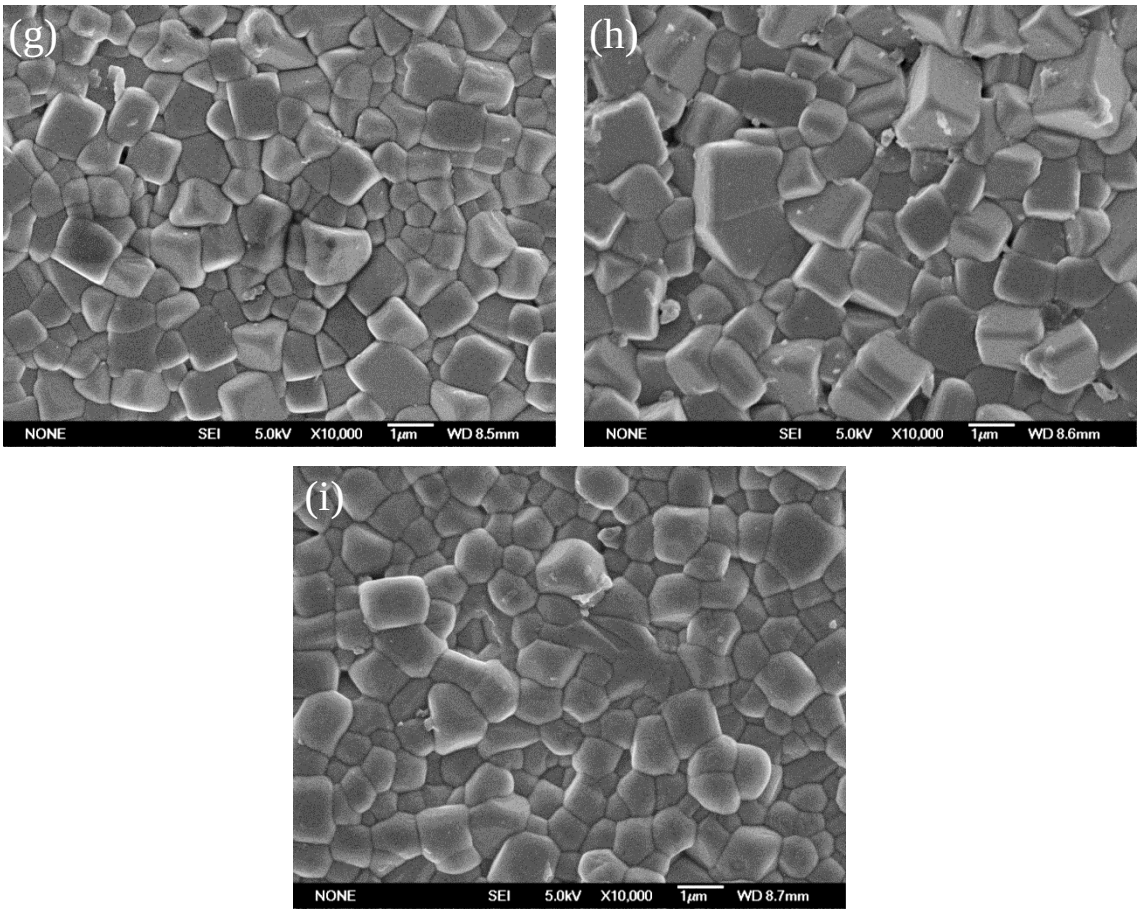

Figure 4.2 FE-SEM micrographs of the BNBT-xEr ceramics, (a) x=0, (b) x=0.005, (c) x=0.01, (d) x=0.02, (e) x=0.03, (f) x=0.04, (g) x=0.05, (h) x=0.06, (i) x=0.07.

Table 4.1 Average grain sizes of the BNBT-xEr ceramics.

x	**0**	**0.005**	**0.01**	**0.02**	**0.03**	**0.04**	**0.05**	**0.06**	**0.07**
average grain size (μm)	1.07	0.95	0.87	0.97	0.86	0.86	0.87	1.01	0.81

4.3. PL properties

4.3.1. Visible UC emissions

The visible UC emission spectra of the BNBT-xEr ceramics are shown in Fig. 4.3. Under an excitation of 980 nm, the visible emission is very strong and a bright (green or yellowish green) spot on the irradiated surface of the ceramics can be easily observed by the naked eye during the measurement. As shown in Fig. 4.3, all the BNBT-xEr ceramics exhibit three characteristic luminescent emission bands in 512 - 536 nm (green), 536 - 569 nm (green) and 640 - 681 nm (red), respectively. They are attributed to the transitions $^{2}H_{11/2} \rightarrow {}^{4}I_{15/2}$, $^{4}S_{3/2} \rightarrow {}^{4}I_{15/2}$ and $^{4}F_{9/2} \rightarrow {}^{4}I_{15/2}$, respectively. Among them, the green emission band at 532 nm is very weak, while the PL intensities of the other two are affected strongly by the Er^{3+}-doping.

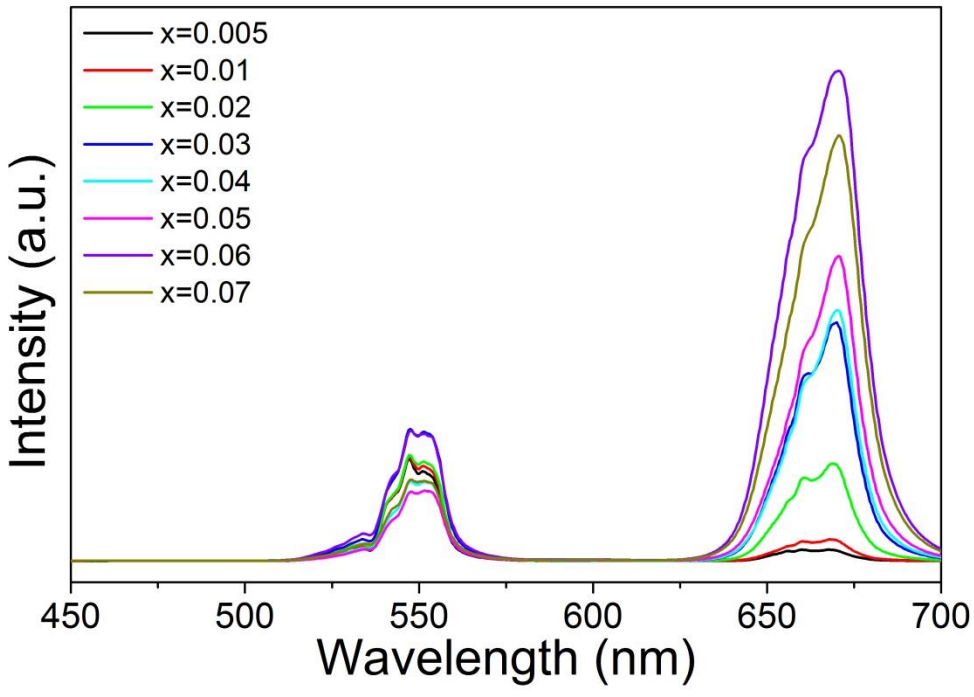

Figure 4.3 Visible UC emission spectra of the BNBT-xEr ceramics.

The ratio of the peak intensities of the red (660 nm) and green (547 nm) emission bands (R/G) has been calculated, giving the results shown in Fig. 4.4. As x increases from 0.005 to 0.07, the calculated R/G increases significantly from 0.152 to 6.58. Accordingly, the Commission Internationale de L'Eclairage (CIE) chromaticity coordinates (X, Y) show a red shift (Fig. 4.5), changing from (0.29, 0.69) at x = 0.005 to (0.49, 0.50) at x = 0.07, and the emission color changes from green to yellowish green (Fig. 4.6).

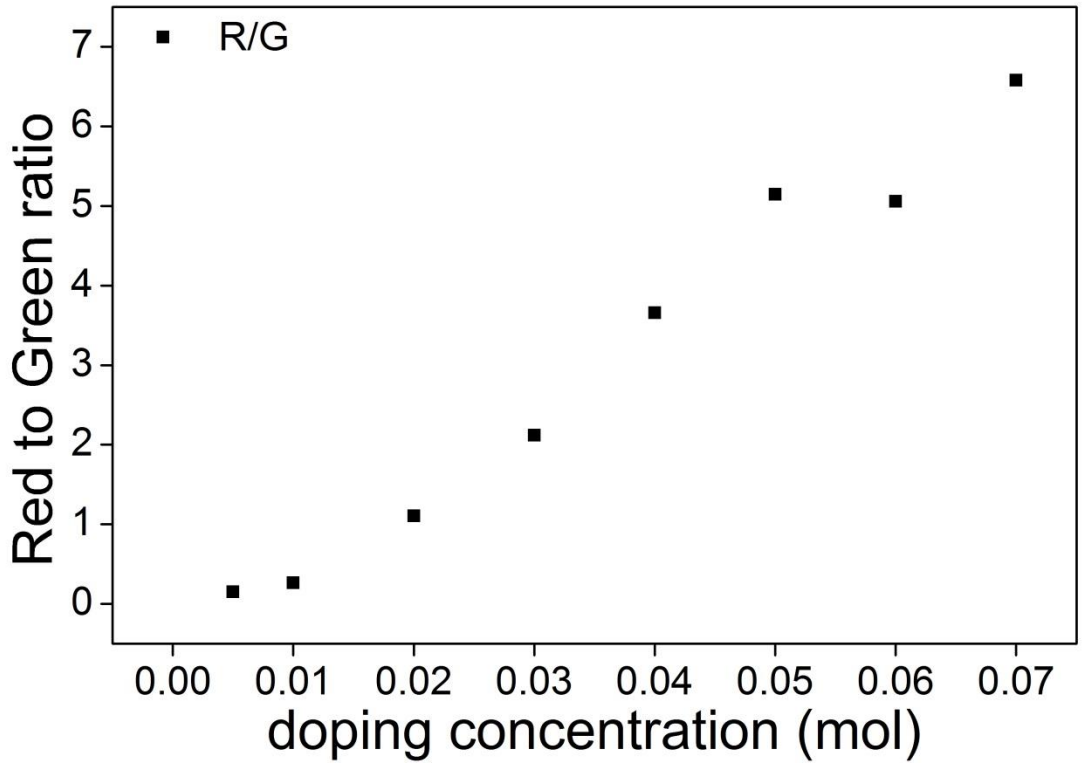

Figure 4.4 R/G of the BNBT-xEr ceramics.

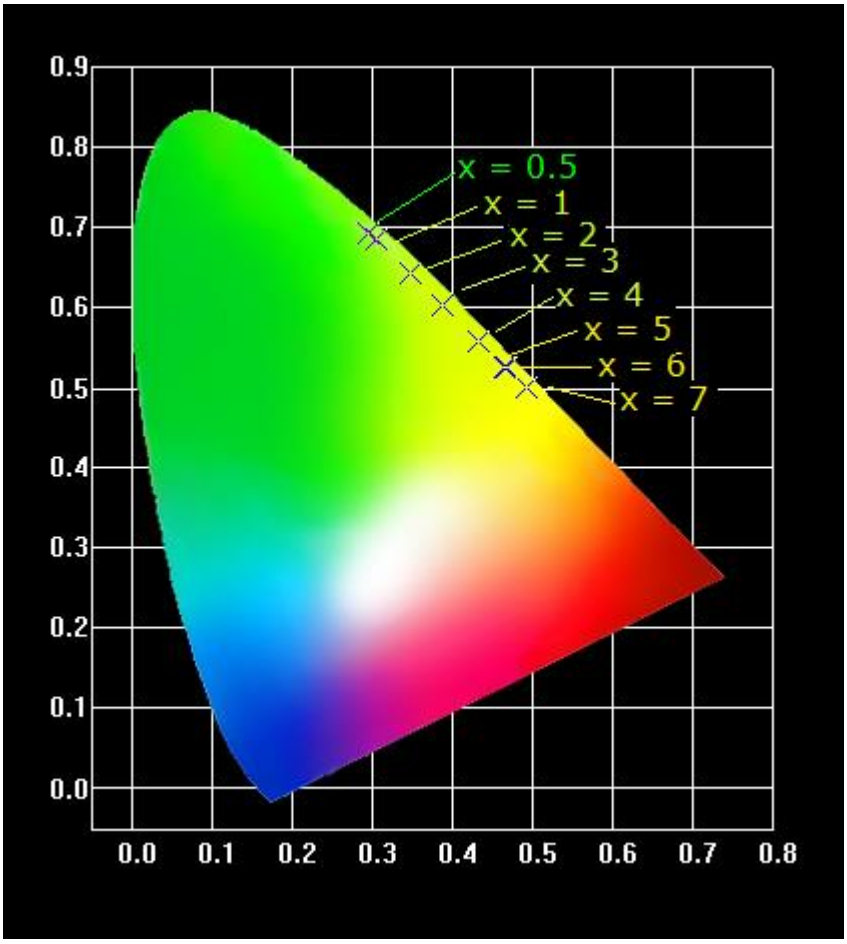

Figure 4.5 CIE chromaticity diagram of the BNBT-xEr ceramics.

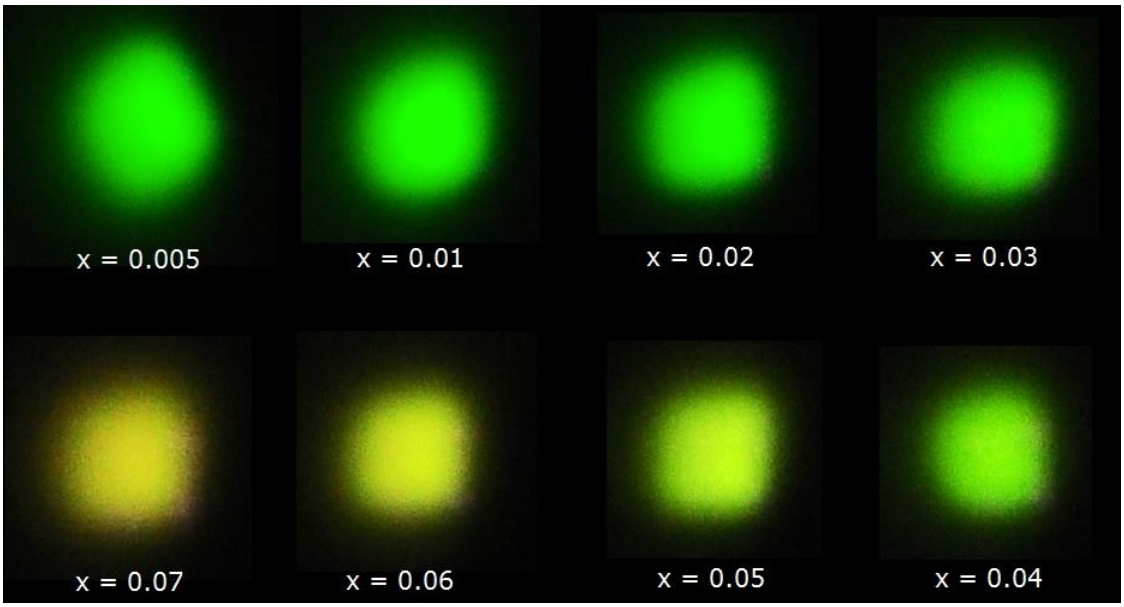

Figure 4.6 Photographs of the visible emissions of the BNBT-xEr ceramics.

4.3.2. NIR and MIR DC emissions

The NIR and MIR DC emission spectra of the BNBT-xEr ceramics are shown in Fig. 4.7 and Fig. 4.8 respectively. All the ceramics exhibit a broad NIR emission band in the range of 1.44 μm to 1.66 μm (Fig. 4.7) and a broad MIR emission band in the range of 2.62 μm to 2.84 μm (Fig. 4.8). The emissions are attributed to the transitions $^4I_{13/2} \rightarrow {}^4I_{15/2}$ and $^4I_{11/2} \rightarrow {}^4I_{13/2}$, respectively. Similar to the visible emissions, the PL intensity of both the NIR and MIR emissions are affected by the Er^{3+}-doping.

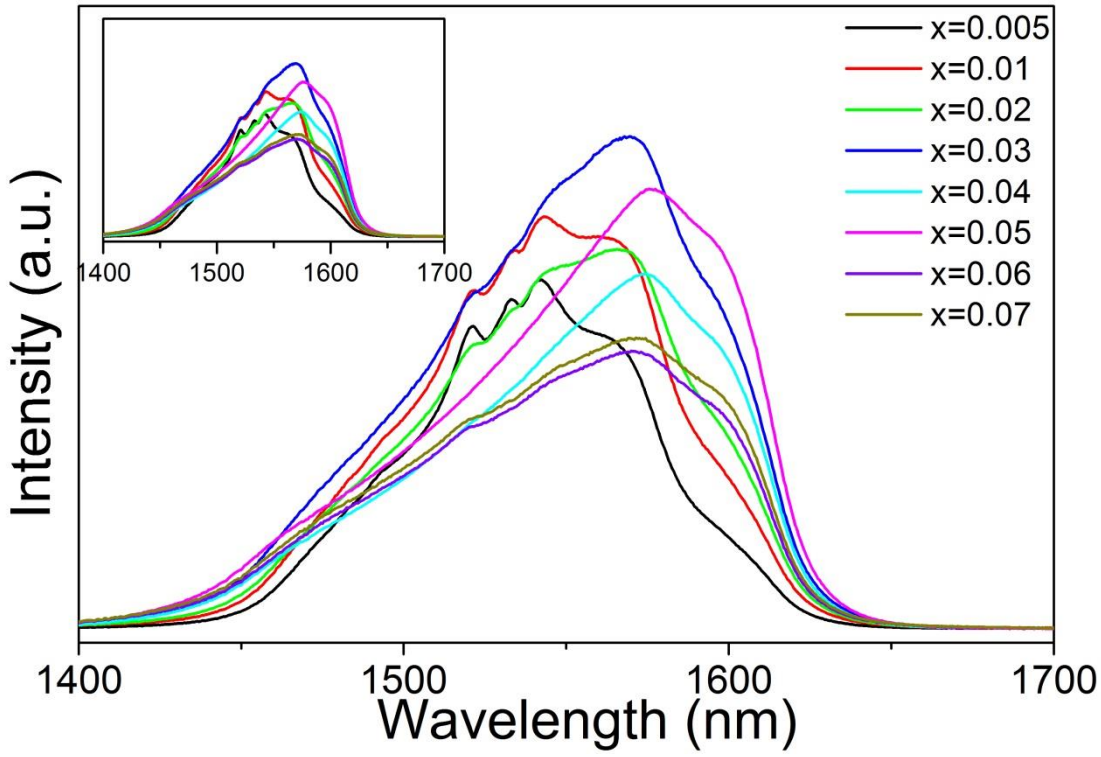

Figure 4.7 NIR DC emission spectra of the BNBT-xEr ceramics.

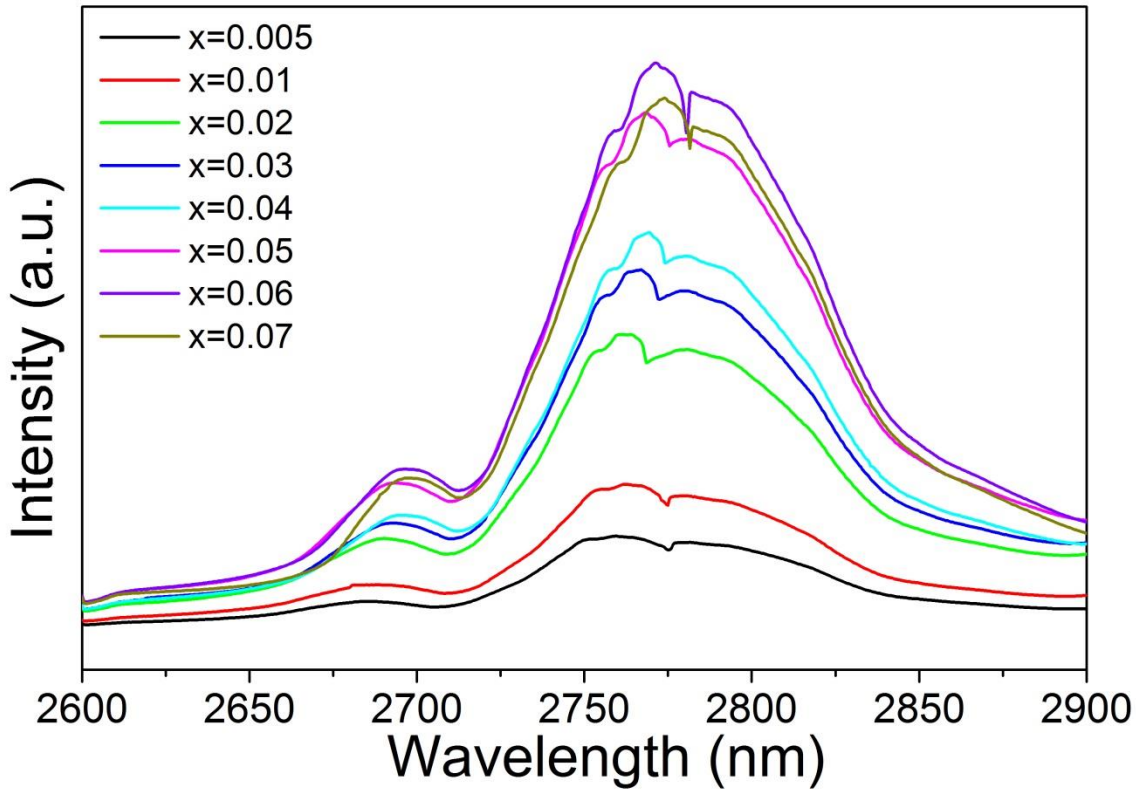

Figure 4.8 MIR DC emission spectra of the BNBT-xEr ceramics.

The peak wavelength (i.e., the wavelength at which the PL intensity reaches a maximum) for both the NIR and MIR emission bands are also affected by the Er^{3+}-doping. For the ease of observation, the NIR emission spectra are re-plotted in the inset of Fig. 4.7, with their baseline shifted upwards by various amounts. Fig. 4.9 shows the variations of the peak wavelength with x. It can be seen that both the NIR and MIR emission bands exhibit a red-shift, giving an increase in the peak wavelength of 19 nm and 15 nm, respectively. Moreover, it is noted that the shape of the NIR mission spectrum become broadened and more asymmetric with increasing x. As x increases from 0.005 to 0.07, the full width half maximum (FWHM) of the spectrum increases from 84 nm to 122 nm.

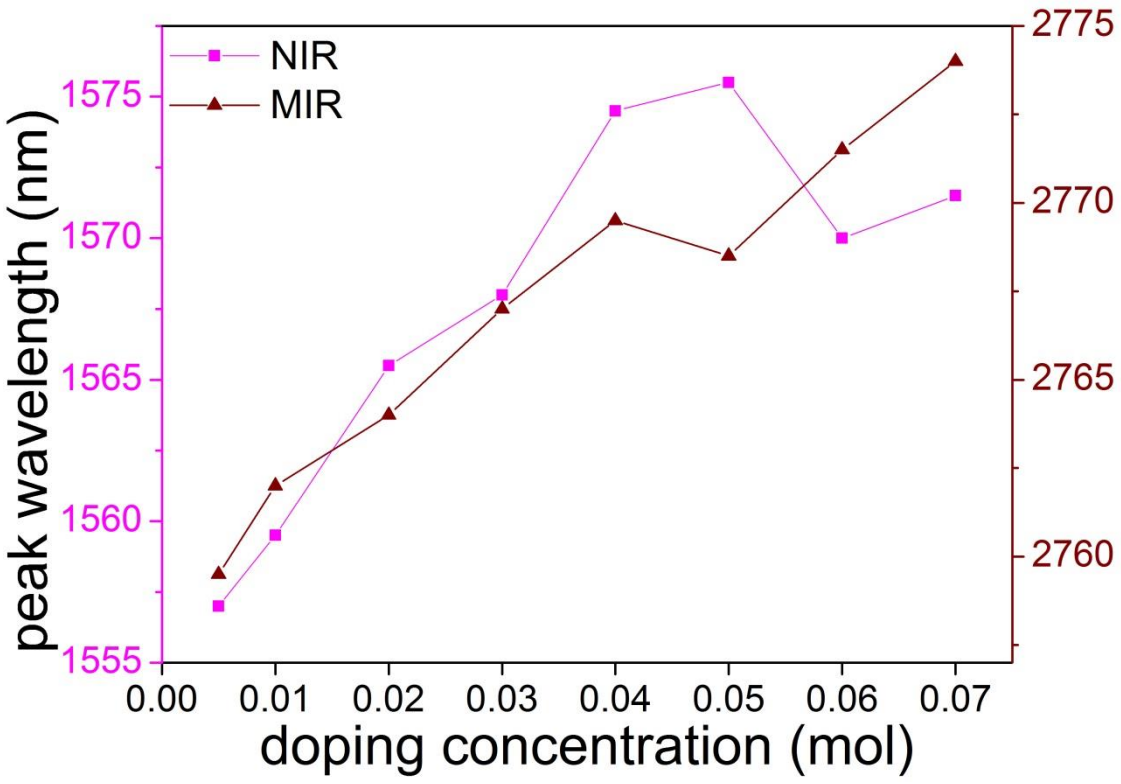

Figure 4.9 Peak wavelength of NIR and MIR DC emissions of the BNBT-xEr ceramics.

4.3.3. PL mechanism

For studying the effects of Er^{3+} concentration on PL properties, the PL intensities of the green (547 nm), red (660 nm), NIR and MIR emission bands have been integrated, giving the results shown as a function of x (the Er^{3+} concentration) in Fig. 4.10. It can be seen that the red and MIR emission bands exhibit a stronger dependence of the (relative) integrated intensities on x: both of them increase by more than 47 and 4 times, respectively, with increasing x. On the other hand, the observed relative intensities of the green and NIR emission bands vary slightly with increasing x, and

generally exhibit a decrease at x > 0.03. Probably due to the concentration-quenching effect, the observed PL intensity for all the emission bands decreases at x > 0.06.

According to the simplified energy level diagram of Er^{3+} as shown in Fig. 4.11, electrons are first excited by the 980-nm photons to the $^4I_{11/2}$ state through the ground state absorption (GSA). Owing to the long-lived state, some of the excited electrons may be further excited to the $^4F_{7/2}$ state through either the excited state absorption (ESA1) or cross relaxation (CR3). The excited electrons will relax non-radiatively to the $^2H_{11/2}$, $^4S_{3/2}$ and $^4F_{9/2}$ states subsequently by the multi-phonon relaxation (MPR), and then relax radiatively to the $^4I_{15/2}$ ground state, producing the green and red emissions, respectively (Fig. 4.3). Probably due to the fast relaxation rate resulted from the small energy gap, the population of the $^2H_{11/2}$ state is low, and hence the green emission at 532 nm becomes very weak. On the other hand, due to the large energy gap and then low relaxation rate, the population of the $^4S_{3/2}$ state remains high while that of the $^2F_{9/2}$ level is low, and thus leading to the strong green emission at 547 nm and weak red emission at 660 nm, respectively, in the ceramics with x < 0.03.

In general, the CR and energy transfer (ET) processes are inefficient for the ceramics with low Er-concentrations. As x increases, the distance between Er^{3+} ions is shortened and the CR and ET processes become more efficient [8][13]. Accordingly, due to the efficient CR3 process, the PL intensity of the green and red emission bands increases as x increase from 0.005 to 0.03. The increase in intensity should also be partly attributed to the increase of the Er-luminescent centers. However, there are other CR processes, such as CR1 ($^4F_{7/2} + {}^4I_{11/2} \rightarrow {}^4F_{9/2}$) and CR2 ($^2H_{11/2} + {}^4I_{15/2} \rightarrow {}^4I_{9/2} + {}^4I_{13/2}$) which reduce the populations of the $^4F_{7/2}$ and $^2H_{11/2}$ levels. As a result, the green emission becomes weakened for the ceramics with x > 0.03 (Fig. 4.10). Nevertheless,

the population of the $^4F_{9/2}$ level is increased at the same time, and thus leading to the continuous increase of the PL intensity of the red emission [108].

As illustrated in Fig. 4.11, the CR4 process ($^4I_{13/2} \rightarrow {}^4I_{9/2} + {}^4I_{15/2}$) together with ET1 and ET2 form a dynamic circulatory energy process, which reduce the population of the $^4I_{13/2}$ level and increase that of the $^4I_{9/2}$ level at the same time. Thus, a population inversion between these two levels is achieved. As a result, the MIR emission increase continuously at the expense of the NIR emission [101]. Instead of participating in the circulatory process, some of the excited electrons in the $^4I_{13/2}$ level may be further excited to the $^4S_{3/2}$ level via ESA2. This will then enhance the green emission of the ceramics with high x. On the other hand, the excited electrons may lose energy, e.g., via the re-absorption by the neighboring ions, during the CR and ET processes, and thus leading to an increase in wavelength of the subsequent radiative transitions [109][110]. Owing to the extensive involvement of the CR and ET processes, in particular the circulatory process, a shift of the emission wavelengths has been observed in the NIR and MIR emission bands, rather than in the visible emission bands (Fig. 4.9). Apparently, not all the electrons will lose energy in the CR and ET processes and the energy losses may not be the same for each electron. As a result, the shape of the emission band that is composed of numerous Stark components will change, for example, to asymmetric as the one observed in the NIR emissions (Fig. 4.7).

The ET and CR processes become dominant at higher x, e.g., > 0.06, and then the luminescent centers act as killers or quenchers to complete the transitions through non-radiative transitions. As a result, the luminescence decrease and it is known as the concentration-quenching effect [1].

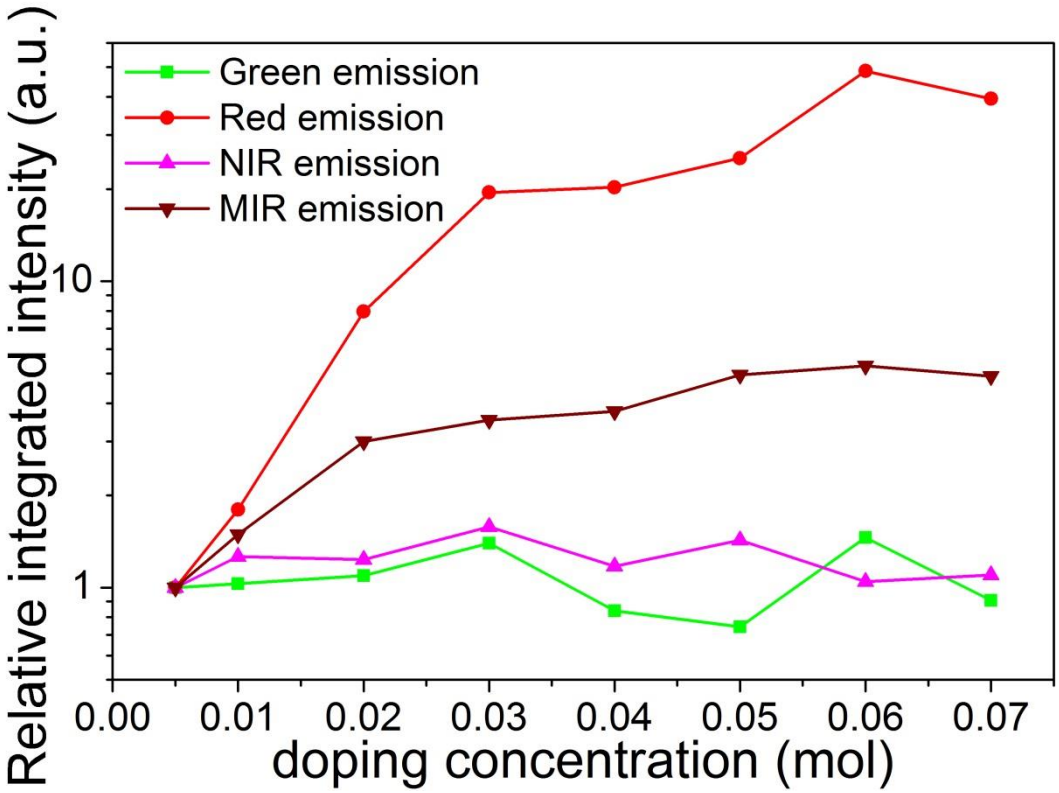

Figure 4.10 Relative integrated intensity of the BNBT-xEr ceramics.

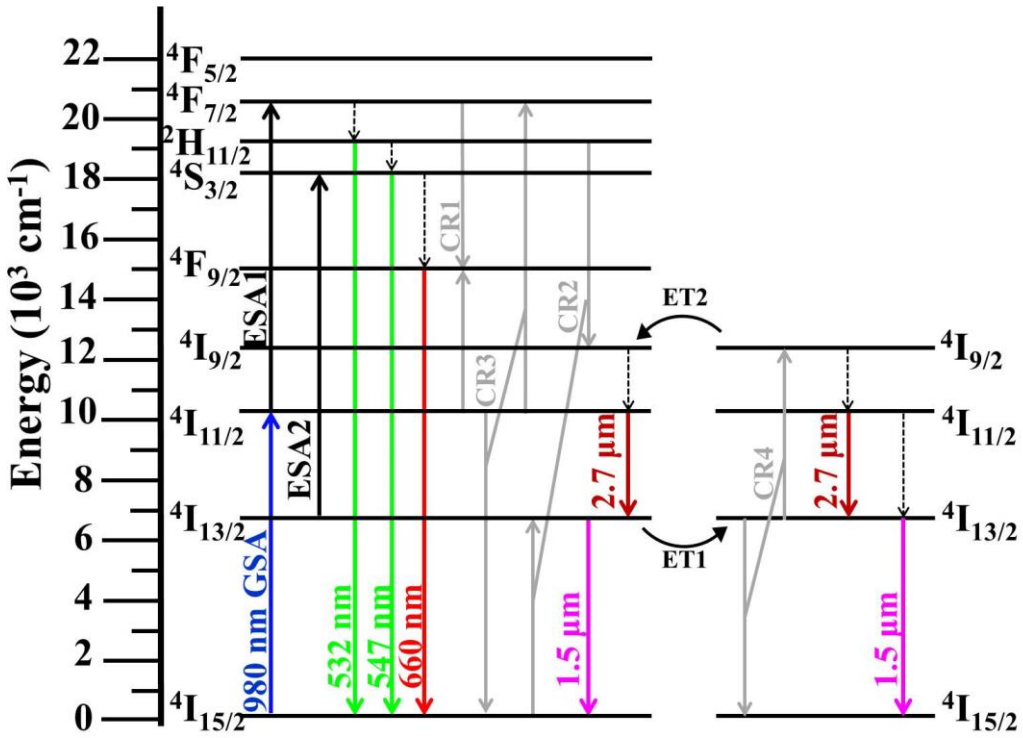

Figure 4.11 Schematic diagram for the PL mechanism of Er^{3+} under an excitation of 980 nm.

4.4. Electrical properties

4.4.1. Dielectric and piezoelectric properties

As discussed in Chapter 3, probably due to the slightly change in composition arisen from the fabrication processes, the BNBT-0Er ceramic (i.e., BNBT-Er(0) in Chapter 3) possesses a low depolarization temperature (T_d, < 25°C) and thus exhibits relaxor-like characteristics at room temperature. Fig. 4.12 shows the temperature dependence of dielectric constant (ε_r) and dielectric loss ($tan\ \delta$) measured at 100 kHz for the BNBT-xEr ceramics with x = 0, 0.01, 0.03, 0.05, 0.07, while their values measured at 1 kHz and room temperature are listed in Table 4.2. The transition peak becomes further broadened and the observed ε_r in the whole temperature range decreases with increasing x (Fig. 4.12 and Table 4.2). The suppression of dielectric properties should be attributed to the disruption of the long-range ferroelectric order by the Er-doping, which is similar to the previous work on KNN-modified BNT-BT ceramics [103]. Nevertheless, the Er-doping improves the leakage of the ceramics. As shown in Table 4.2, the observed room-temperature $tan\ \delta$ (at 1 kHz) reaches a very small value of 0.026 at x = 0.07.

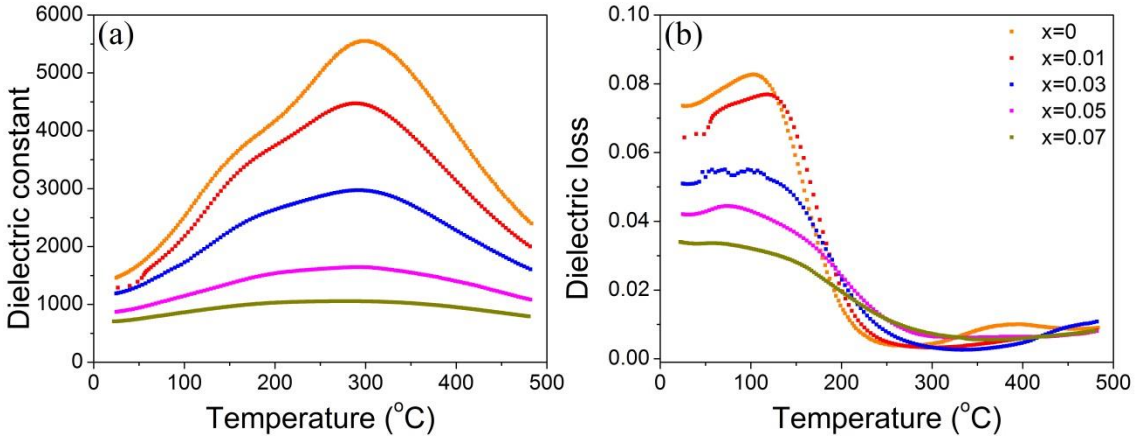

Figure 4.12 Temperature dependence of (a) ε_r (b) *tan* δ measured at 100kHz of the BNBT-xEr ceramics.

The piezoelectric constant (d_{33}) of the ceramics are also listed in Table 4.2 for comparison. As x increases from 0 to 0.07, the observed d_{33} decreases significantly from 194 pC/N to 4 pC/N. Similarly to ε_r, this should be attributed to the disruption of the long-range ferroelectric order by Er^{3+}-doping [103].

Table 4.2 Dielectric constant, dielectric loss and piezoelectric constant of the BNBT-xEr ceramics.

x	***ε_r @ 1kHz***	***tan δ@ 1kHz***	***d_{33} (pC/N)***
0	1813	0.057	194
0.005	1653	0.051	43
0.01	1616	0.050	27
0.02	1421	0.044	11
0.03	1229	0.046	5.7
0.04	1111	0.035	11
0.05	997	0.032	6.8
0.06	944	0.029	6.5
0.07	787	0.026	4.1

4.4.2. Ferroelectric properties

Fig. 4.13 shows the ferroelectric hysteresis loops (PE loops) of the BNBT-xEr ceramics with x = 0, 0.01, 0.03, 0.05, 0.07. After the doping of Er^{3+}, the PE loop becomes further slanted, and the observed remanent polarization (P_r) decreases continuously with increasing x. These indicate that the ferroelectric properties are deteriorated, which should also be attributed to the disruption of the long-range ferroelectric order by Er^{3+}-doping [103]. According to the phenomenological theory, d_{33} is related to ε_r, the permittivity of vacuum ε_o, the spontaneous polarization P_s (which may be approximated by P_r) and the electrostrictive coefficient Q_{11} via a general equation $d_{33} = 2\varepsilon_o\varepsilon_r Q_{11} P_s$ [103]. The significant decrease in d_{33} of the doped ceramics should hence be partly attributed to the decreases in both ε_r and P_r.

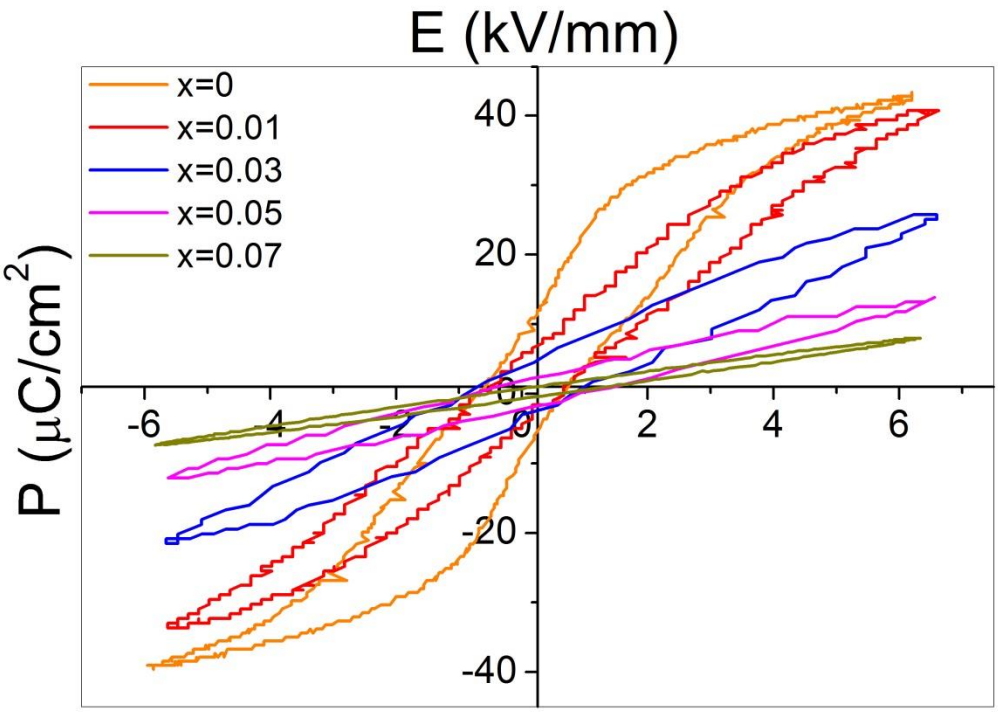

Figure 4.13 PE loops of the BNBT-xEr ceramics.

4.5. Conclusion

BNBT-xEr ceramics have been prepared and their PL, dielectric, piezoelectric and ferroelectric properties have been investigated. The ceramics possess a single-phase perovskite structure, and the densification is improved by the Er^{3+}-doping. Under an excitation of 980 nm, the ceramics exhibit visible UC emissions at 532 nm (green), 547 nm (green) and 660 nm (red), as well as NIR and MIR DC emissions. As x increases from 0.005 to 0.07, the PL intensity of the red emission increases significantly by more than 47 times. As a result, the CIE chromaticity coordinates shift from (0.29, 0.69) to (0.49, 0.50) and the emission color shows an obvious change from green to yellowish green color. Probably due to the establishment of a dynamic circulatory energy process, the PL intensity of the MIR emission increases significantly by more than 4 times at the expense of NIR emission. The quenching concentration for the ceramics is high, about 6%. The BNBT-xEr ceramics also exhibit good dielectric, piezoelectric and ferroelectric properties, and hence they should have great potential for multifunctional applications.

Chapter 5. Pr^{3+}-doped BNBT ceramics

5.1. Introduction

As discussed in Chapters 3 and 4, Er^{3+}-doped BNBT ceramics have been fabricated and their up-conversion (UC) photoluminescence (PL) properties have been investigated. Other than Er^{3+}, Pr^{3+} is another efficient activator for giving out various luminescence in the visible light and near-infrared (NIR) regions under a blue-light or ultraviolet (UV) excitation [111]. Owing to the unique PL performances, Pr^{3+}-doped luminescent materials should have great potentials in optical-and-electro multifunctional applications [44][45] as well as the white-light production via the mixing of the red and green emissions with the blue excitation light [46][47].

In this chapter, Pr^{3+}-doped ferroelectric ceramics $0.93(Bi_{0.5-x/0.93}Pr_{x/0.93}Na_{0.5}TiO_3)$-$0.07(BaTiO_3)$ (abbreviated as BNBT-xPr, where x denotes the molar fraction and varies from 0 to 0.02) have been prepared by the conventional solid state reaction (SSR) method. As shown in the chemical formula, Bi^{3+} is substituted by Pr^{3+} for minimizing the unnecessary effects of oxygen or cation vacancies on the PL and electrical properties. The optimum sintering temperature for obtaining dense BNBT-xPr ceramics has been determined as 1200°C. The down-conversion (DC) PL emissions have been studied and the corresponding mechanisms have been deduced. The effects of Pr^{3+} on the PL emissions in the visible and NIR regions have been investigated. Moreover, their dielectric, piezoelectric and ferroelectric properties have been studied.

5.2. Structural properties

5.2.1. XRD

Fig. 5.1 shows the XRD patterns of the BNBT-xPr ceramics, in crushed powder form. The XRD pattern of the BNBT-0Pr ceramic is consistent with the results published elsewhere [91][92]. All the ceramics possess a single-phase perovskite structure, suggesting that Pr^{3+} has diffused into and entered the Bi^{3+} sites of the BNBT lattices. A splitting of the (002)/(200) characteristics peaks at 46.6° has been observed for all the ceramics, indicating that they reside near the morphotropic phase boundary (MPB) and contains both the rhombohedral and tetragonal phases. Unlike Er^{3+}, the ionic radii of Pr^{3+} and Bi^{3+} are very similar (~1.32 Å) [112], and hence no significant shifting of the characteristic peaks has been observed for the BNBT-xPr ceramics.

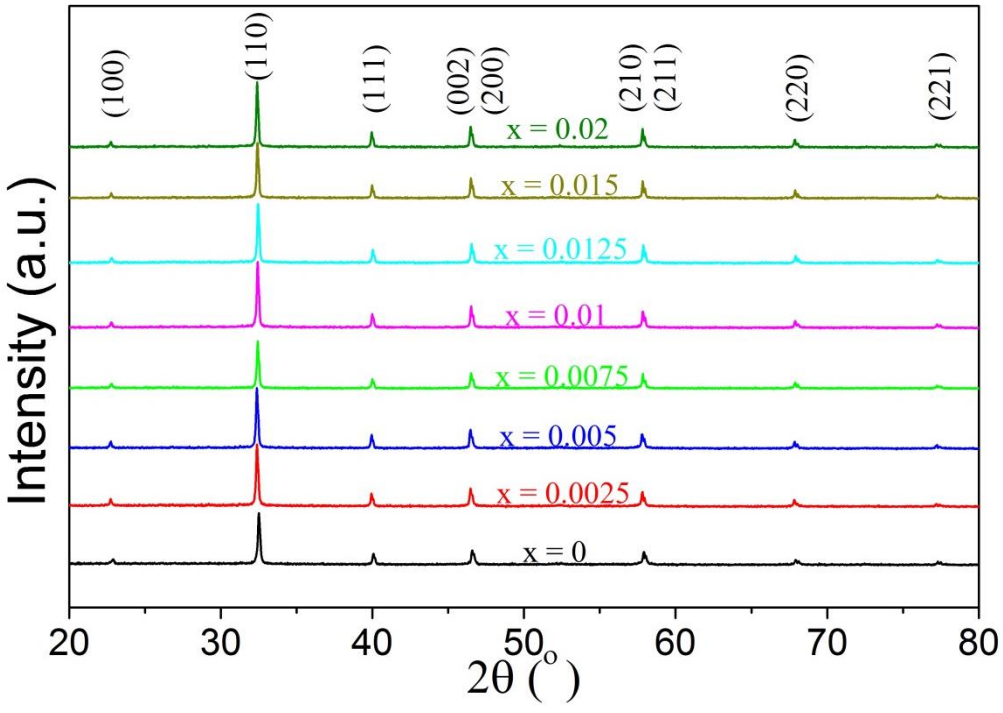

Figure 5.1 XRD patterns of the BNBT-xPr ceramics.

5.2.2. FE-SEM

The FE-SEM micrographs of the BNBT-xPr ceramics are shown in Fig. 5.2 and their average grain sizes are listed in Table 5.1. All the ceramics possess a well-sintered and dense structure. The densification improves as x (the Pr^{3+} concentration) increases from 0 to 0.02. As shown in Fig. 5.2(a-f) and Table 5.1, the average grain sizes of the ceramics decreases from 1.07 μm to 0.77 μm as x increases from 0 to 0.0125, and then increases to 1.2 μm at x = 0.02. The decrease in grain size should be attributed to the inhibition of grain growth caused by the Pr^{3+}-doping. However, it has been observed that the grain size distribution for each ceramic is not uniform. This should be attributed to the various particle sizes of the starting powders that have different priorities in the sintering process [94][107].

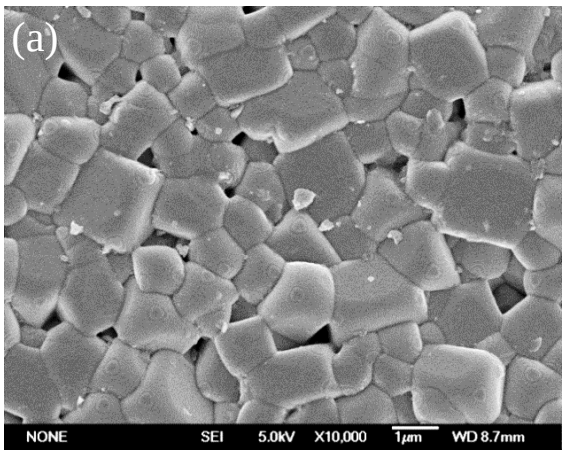

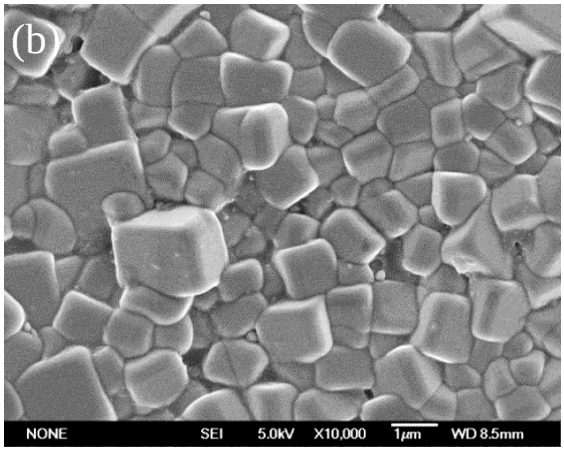

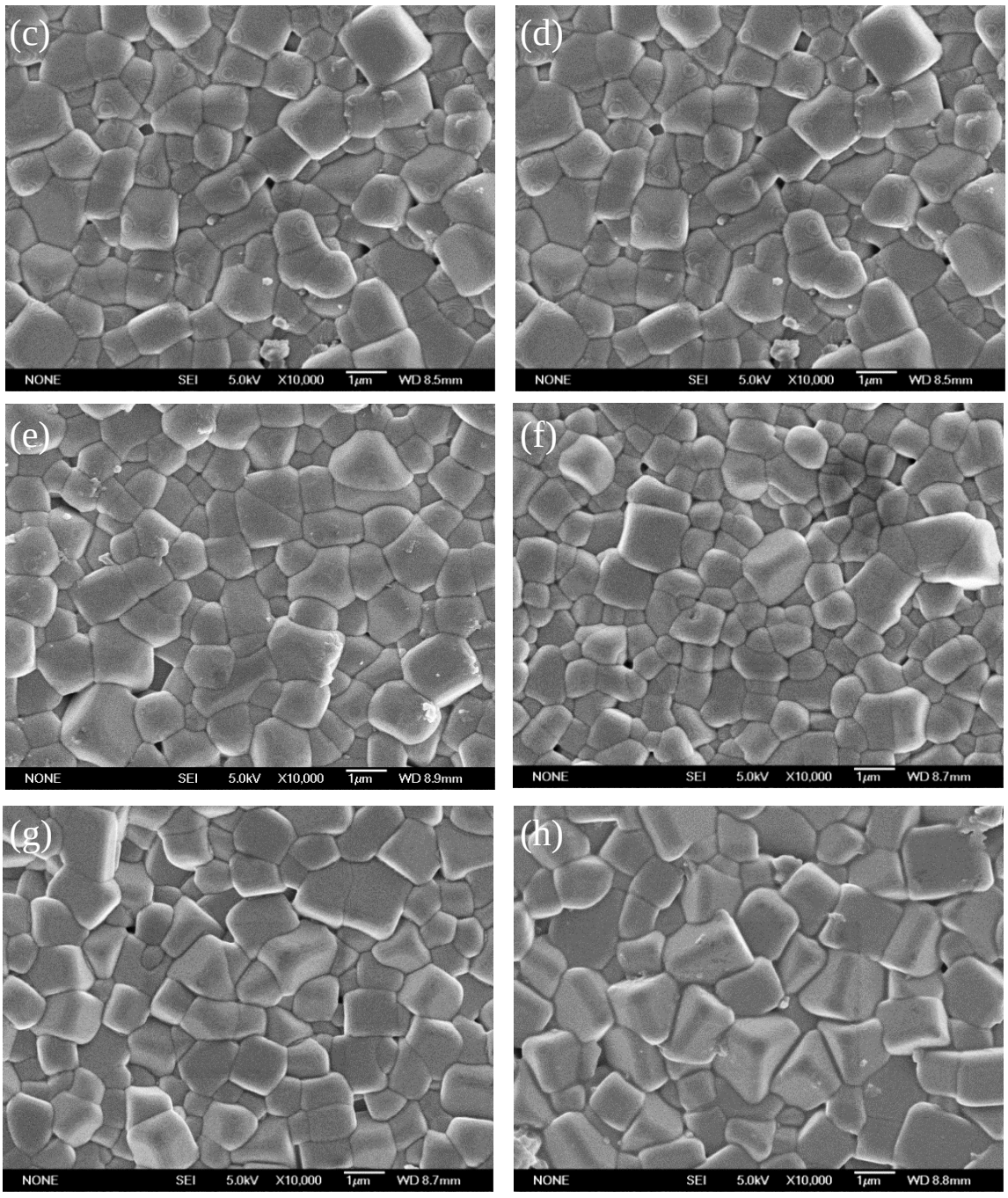

Figure 5.2 FE-SEM micrographs of the BNBT-xPr ceramics, (a) x=0, (b) x=0.0025, (c) x=0.005, (d) x=0.0075, (e) x=0.01, (f) x=0.0125, (g) x=0.015, (h) x=0.02.

Table 5.1 Average grain sizes of the BNBT-xPr ceramics.

x	**0**	**0.0025**	**0.005**	**0.0075**	**0.01**	**0.0125**	**0.015**	**0.02**
average grain size (μm)	1.07	1.03	1.01	0.98	0.94	0.77	0.92	1.20

5.3. PL properties

5.3.1. Photoluminescence Excitation (PLE)

The PLE spectrum of the BNBT-0.01Pr ceramic monitoring at 610 nm (the typical red emission of Pr^{3+}) is shown in Fig. 5.3. The ceramic exhibits a weak and broad excitation band at 350 - 410 nm and strong excitation peaks at 453 nm, 474 nm and 490 nm, respectively. The weak excitation band should be resulted from the charge transfer transition ($Pr^{3+} \rightarrow Ti^{4+}$) and the excitation band of Bi^{3+} ($^1S_0 \rightarrow {}^3P_1$) [113][114][115]. The strong peaks are attributed to the excitations of Pr^{3+} from the $^3H_4$ ground level to the $^3P_2$, $^3P_1$ and $^3P_0$ excited levels, respectively [113][116]. Owing to the strongest excitation peak, an excitation source at 474 nm has been chosen for investigating the PL emissions of the BNBT-xPr ceramics.

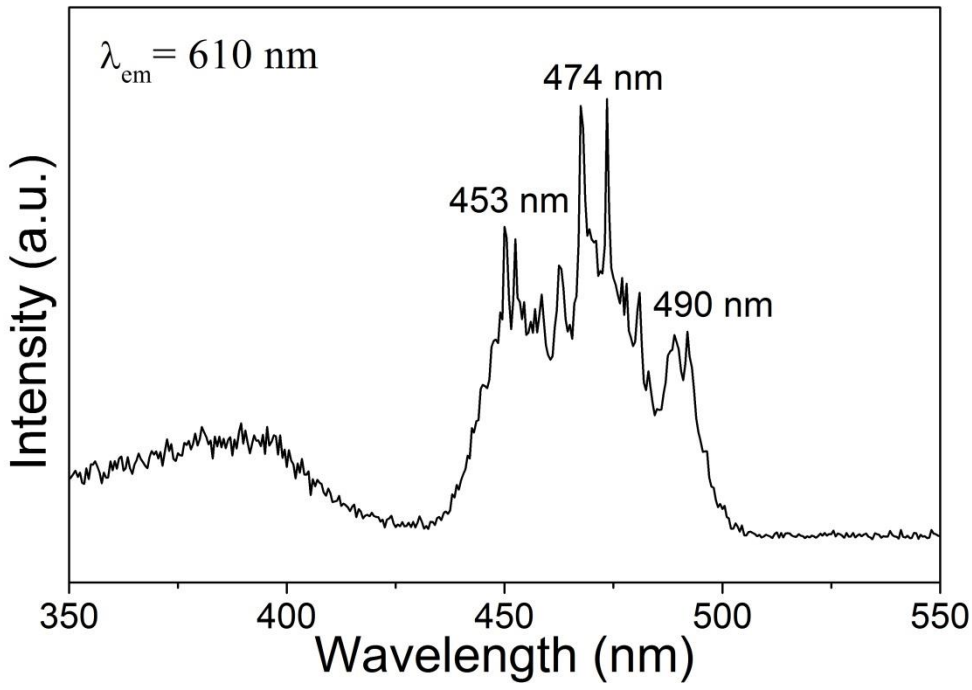

Figure 5.3 PLE spectrum of the BNBT-0.01Pr ceramics.

5.3.2. Visible to NIR emissions

The visible-NIR and NIR DC emission spectra of the BNBT-xPr ceramics are shown in Fig. 5.4 and 5.5, respectively. Under an excitation of 474 nm, all the ceramics show the characteristic DC emissions of Pr^{3+} at 532 nm ($^3P_1 \rightarrow {}^3H_5$), 547 nm ($^3P_0 \rightarrow {}^3H_5$), 610 nm ($^3P_1 \rightarrow {}^3H_6$), 620 nm ($^3P_0 \rightarrow {}^3H_6$), 625 nm ($^3P_1 \rightarrow {}^3F_2$), 654 nm ($^3P_0 \rightarrow {}^3F_2$), 695 nm ($^3P_1 \rightarrow {}^3F_4$), 710 nm ($^3P_0 \rightarrow {}^3F_3$), 741 nm ($^3P_0 \rightarrow {}^3F_4$), 810 nm ($^1D_2 \rightarrow {}^3H_6$), 1030 nm ($^1D_2 \rightarrow {}^3F_4$), 1047 nm ($^1G_4 \rightarrow {}^3H_4$) and 1485 nm ($^1D_2 \rightarrow {}^1G_4$) (Fig. 5.7). The results are similar to the previous works of Pr^{3+}-doped fiber laser and fluoroindate glasses [117][118]. Due to the small energy difference between the $^3P_0$ and $^3P_1$ levels, the emissions arisen from the transitions $^3P_0 \rightarrow {}^3H_6$ (620 nm) and $^3P_1 \rightarrow {}^3F_2$ (625 nm) combine as a characteristic peak at 620 nm as shown in Fig. 5.4. It should also be noted that the emission peaks at 1220 nm, 1240 nm and 1308 nm are the second-order scattering of the emission peaks at 610 nm, 620 nm and 654 nm respectively (Fig. 5.5). The scattering should be attributed to the scattering at the grating of the PL spectrometer [119].

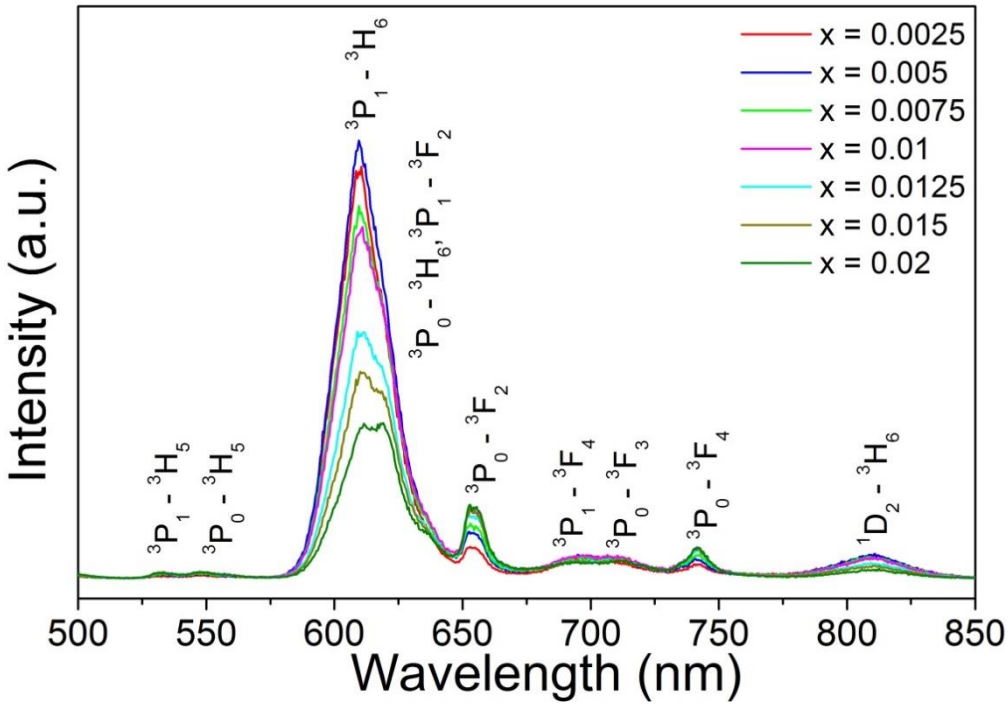

Figure 5.4 Visible-NIR DC emission spectra of the BNBT-xPr ceramics.

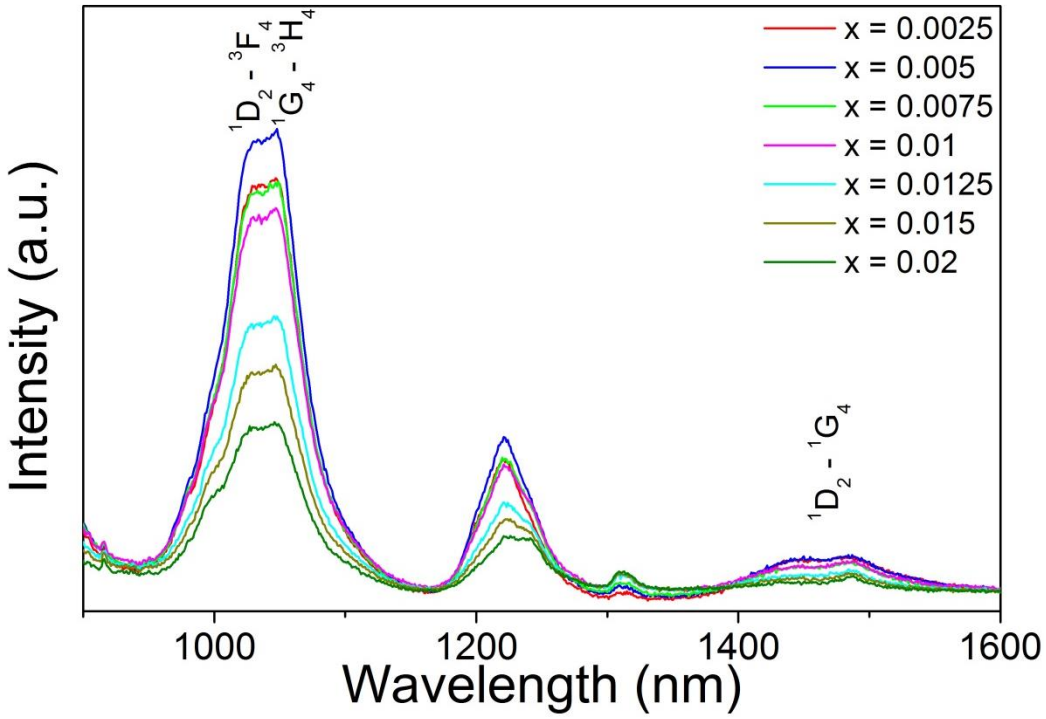

Figure 5.5 NIR DC emission spectra of the BNBT-xPr ceramics.

The peak PL intensities of the emissions at different wavelengths have been plotted as functions of x in Fig. 5.6. Owing to the weakness, those of the emissions at 532 nm, 547 nm, 695 nm and 710 nm have not been included for the comparison. It can be seen that the PL intensities of all the emissions, in particular those at 654 nm and 741 nm, increase as x increases from 0.0025 to 0.005. It can be seen that the PL intensities of the red emissions at 654 nm and 741 nm increase by 2.3 and 2.2 times, respectively, as x increases from 0.0025 to 0.02. On the other hand, the PL intensities of all the other emissions increase only slightly as x increases to 0.005, and then decrease significantly with further increasing x. Although the quenching concentration for these emissions is low (0.005), the major emissions at 620 nm (red) and 1047 nm (NIR) are very strong for practical applications.

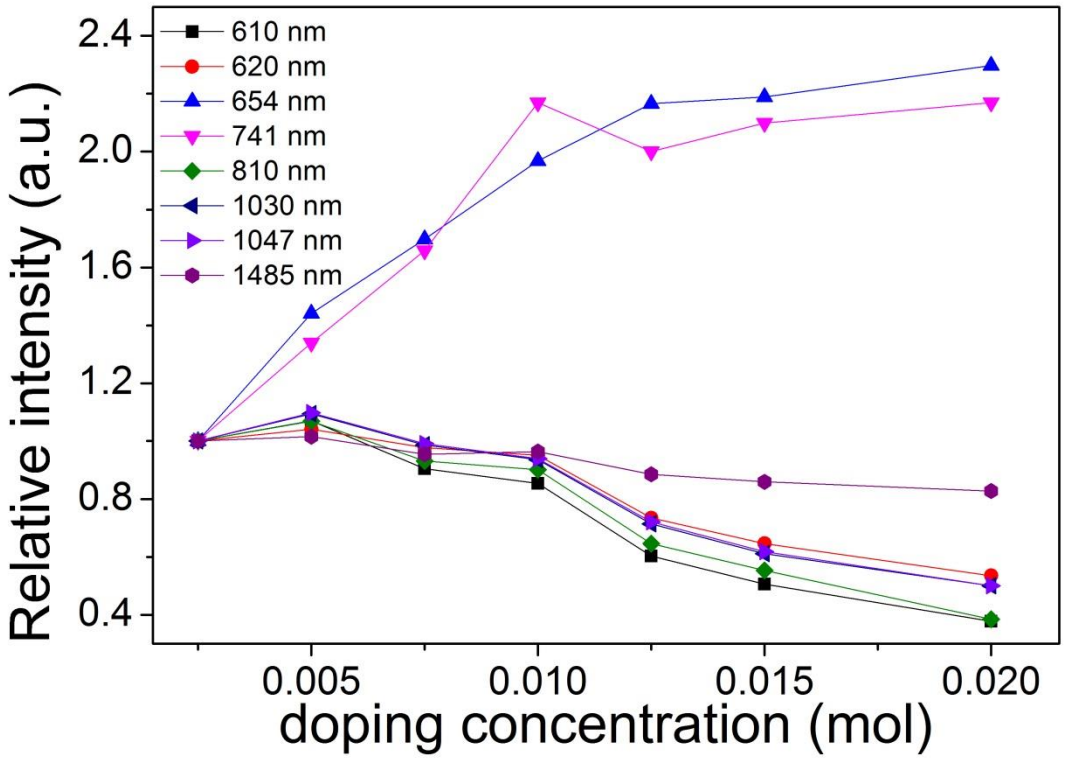

Figure 5.6 Relative peak intensities of the BNBT-xPr ceramics.

5.3.3. PL mechanism

As illustrated in Fig. 5.7, electrons are excited by the 474-nm photons to the $^3P_1$ level through the ground state absorption (GSA). Owing to the small energy difference, some of the excited electrons may relax quickly to the $^3P_0$ level non-radiatively via the multi-phonon relaxation (MPR), and then relax radiatively to the $^3H_5$, $^3H_6$, $^3F_2$, $^3F_3$ and $^3F_4$ levels, producing the emissions at 547 nm, 625 nm, 654 nm, 710 nm and 741 nm, respectively. The excited electrons may also relax radiatively from the $^3P_1$ level directly to those lower energy levels, producing emissions at slightly shorter wavelengths: 532 nm, 610 nm, 620 nm and 695 nm, respectively. Probably due to the large energy gap and then low relaxation rate, the population of the $^1D_2$ level is low. As a result, all the emissions originating from this level are weak, i.e., $^1D_2 \rightarrow {}^3H_4$ at 600 nm, $^1D_2 \rightarrow {}^3H_5$ at 685 nm, $^1D_2 \rightarrow {}^3H_6$ at 810 nm, $^1D_2 \rightarrow {}^3F_2$ at 847 nm, $^1D_2 \rightarrow {}^3F_3$ at 1025 nm, $^1D_2 \rightarrow {}^3F_4$ at 1030 nm, and $^1D_2 \rightarrow {}^1G_4$ at 1485 nm (Fig. 5.4). Some of them are even unobservable in the spectra. It should be noted the PL intensities of the NIR emissions are generally much weaker than those of the visible emissions.

Due to the low interaction between Pr^{3+}, the cross relaxation (CR) processes are generally inefficient at low Pr^{3+} concentrations. As the concentration increases, the distance between the neighboring Pr^{3+} decreases and then the CR processes become more efficient [3]. Owing to the efficient CR1 at $x > 0.005$, the population of the $^3P_1$ level is lowered, and thus leading to the weakening of the emissions at 610 nm, 620 nm and 695 nm. This should also be attributed to the migration of energy to the quenching centers due to the shortened distance between Pr^{3+} [113][120]. On the other hand, the population of the $^3P_0$ level in increased by the CR2 process. As a result, the emissions at

654 nm and 741 nm become stronger, and hence their observed PL intensities increase continuously with increasing x as shown in Fig. 5.6. As also shown in Fig. 5.7, the CR3 and CR4 processes decrease the populations of the $^1D_2$ and $^1G_4$ levels, and thus leading to the decrease in emissions at 810 nm, 1030 nm, 1047 nm and 1485 nm [111]. Although both the emissions at 610 nm and 620 nm involve the electronic transition from the $^3P_1$ level, the PL intensity of the emission at 610 nm decreases more significantly as compared to that at 620 nm (62% vs 47% as x increases from 0.0025 to 0.02). This confirms that the emission at 620 nm are combined from the transitions $^3P_0 \rightarrow {}^3H_6$ (620 nm) and $^3P_1 \rightarrow {}^3F_2$ (625 nm) because of the similar energy levels as mentioned in the previous section. The efficient CR2 process increases the population of the $^3P_1$ level, and thus enhancing the transition $^3P_1 \rightarrow {}^3F_2$ and then reducing the decrease in the observed PL emission (at 620 nm).

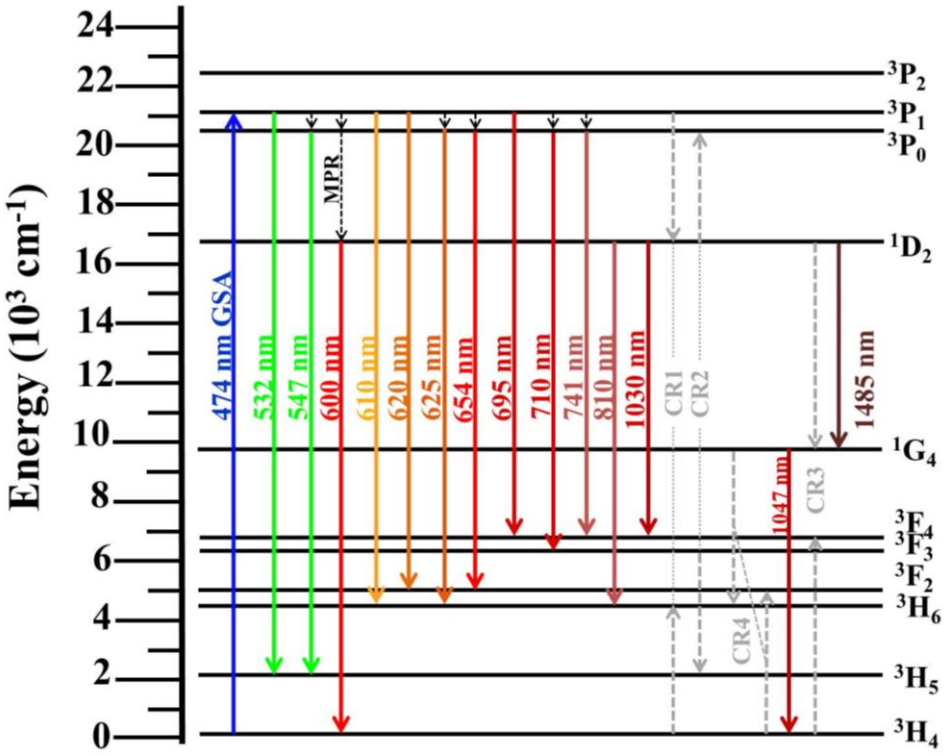

Figure 5.7 Schematic diagram for the PL mechanism of Pr^{3+} under an excitation of 474 nm Xenon lamp.

5.4. Electrical properties

5.4.1. Dielectric and piezoelectric properties

Fig. 5.8 shows the temperature dependence of the observed dielectric constant (ε_r) and dielectric loss ($tan\ \delta$) (measured at 100 kHz) for the BNBT-xPr ceramics. Similar to the BNBT-xEr ceramics, all the BNBT-xPr ceramics show a broad phase transition peak, confirming their relaxor-like characteristics. Their depolarization temperatures (T_d) are also below 25°C, and thus they should exhibit relaxor-like characteristics at room temperature.

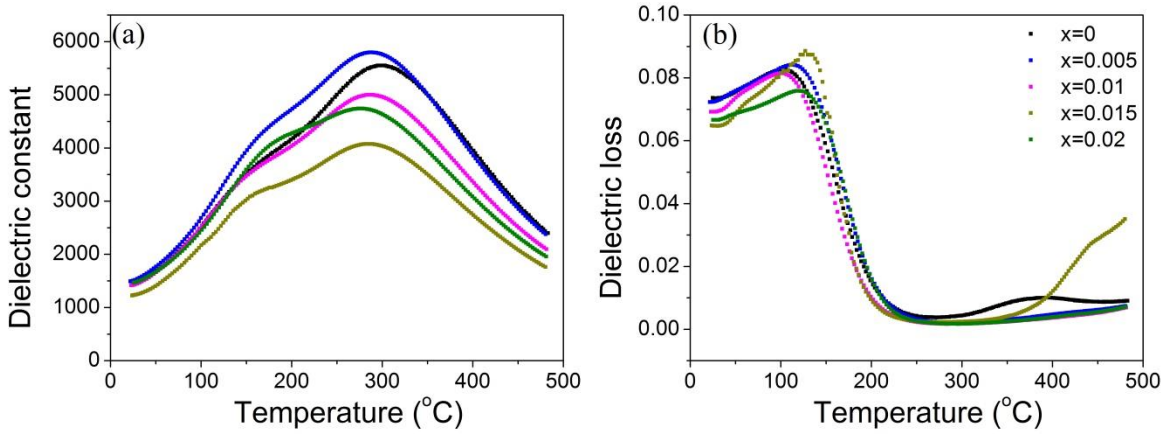

Figure 5.8 Temperature dependence of (a) ε_r (b) $tan\ \delta$ measured at 100kHz of the BNBT-xPr ceramics.

The dielectric and piezoelectric properties of the BNBT-xPr ceramics are listed in Table. 5.2. Although the observed ε_r decreases with increasing Pr^{3+}-concentration, it retains at a high value (> 1600). On the other hand, the observed $tan\ \delta$ remains almost unchanged at a low value of ~0.057. It can also been seen that the observed piezoelectric constant (d_{33}) for the BNBT-xPr ceramics with x ≤ 0.005 remains almost unchanged at ~190 pC/N. Probably due to the disruption of the long-range ferroelectric order by the Pr-doping [103], it decreases rapidly to 14 pC/N with further increasing x. As

the ionic radii of Pr^{3+} and Bi^{3+} are similar (~1.32 Å), the disruption may not be significant at low Pr^{3+}-concentrations, and hence the dielectric and piezoelectric properties of the ceramics with $x \leq 0.005$ remain almost unchanged [112].

Table 5.2 Dielectric constant, dielectric loss and piezoelectric constant of the BNBT-xPr ceramics.

x	***ε_r @ 1kHz***	**tanδ*@ 1kHz***	**d_{33} (pC/N)**
0	1813	0.057	194
0.0025	1829	0.057	188
0.005	1852	0.058	189
0.0075	1745	0.059	38
0.01	1737	0.058	26
0.0125	1677	0.059	23
0.015	1669	0.056	17
0.02	1695	0.058	14

5.4.2. Ferroelectric properties

The ferroelectric hysteresis loops (PE loops) of the BNBT-xPr ceramics measured under an electric field of 5.5 kV/mm at 100 Hz are shown in Fig. 5.9. Similar to d_{33}, the PE loops of the ceramics with x = 0 and 0.005 are similar, suggesting that the small Pr^{3+}-concentration does not affect the ferroelectric as well as piezoelectric properties significantly. As x increases, the PE loop becomes further slanted, indicating the enhanced relaxor-like characteristics. This should also be attributed to the disruption of ferroelectric order by the Pr-doping [103].

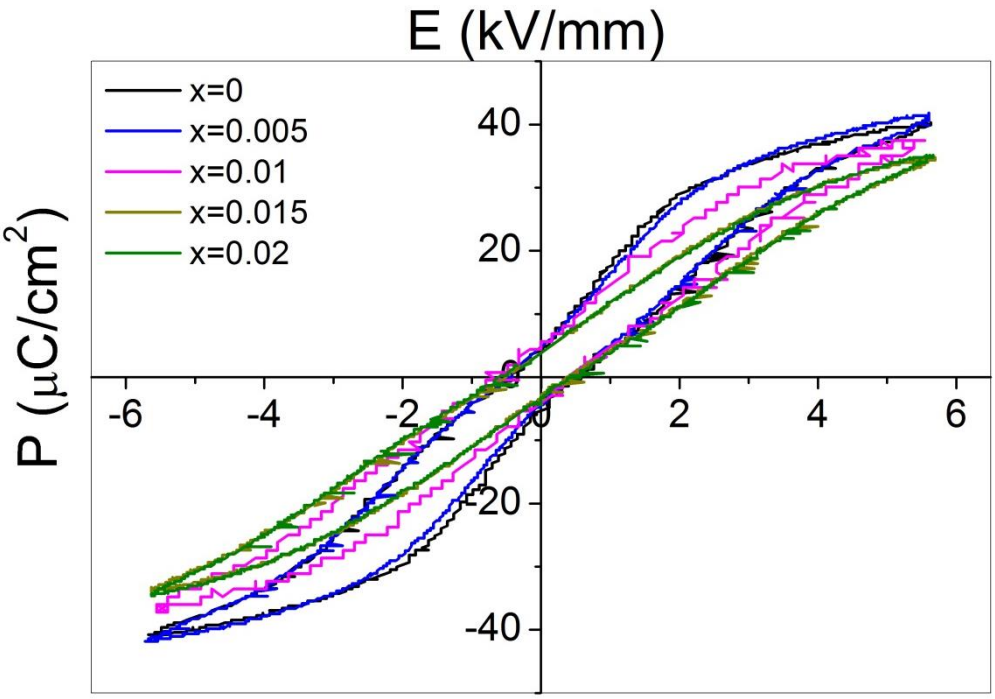

Figure 5.9 PE loops of the BNBT-xPr ceramics.

5.5. Conclusion

BNBT-xPr photoluminescent ceramics have been prepared and their PL and electrical properties have been studied. Our results reveal that Pr^{3+} has diffused into the Bi^{3+} sites to form a single-phase perovskite structure. Under an excitation of 474 nm, the ceramics exhibit various DC emissions in visible light (green and red) and NIR regions. The quenching concentration is low, about a molar fraction of 0.005. Owing to the enhancement of CR, the PL intensity of the emissions at 654 nm and 741 nm increase significantly with increasing x. On the other hand, the enhanced CR processes decrease the PL intensities of the other emissions, both in the visible and NIR regions. For the BNBT-xPr ceramics with $x \leq 0.005$, both the PL properties and the dielectric, piezoelectric and ferroelectric properties are very good. Therefore, they should be a promising candidate for multifunctional optoelectronic applications.

Chapter 6. E-field-dependent PL properties of RE^{3+}-doped BNBT ceramics

6.1. Introduction

As discussed in Chapter 1, the PL properties of an rare-earth ion (RE^{3+}) will vary in different hosts with different crystal symmetries due to the Stack effect [121][122]. Also, it has been reported that the photoluminescence (PL) emissions of some RE^{3+}-doped ferroelectric hosts, such as Er^{3+}-doped BNT ceramics [80], Pr^{3+}-doped $(1-x)(Na_{0.5}Bi_{0.5})TiO_3$-$xCaTiO_3$ ceramics [45], Pr^{3+}-doped KNN ceramics [116] and Yb^{3+}/Er^{3+}-co-doped BT thin films [121], can be enhanced via the poling process or a bias voltage. The enhancement of PL emissions is attributed to the displacement of positive charges along the external electric field (or E-field) that decreases the crystal symmetry and thus affects the local field around the RE^{3+} [121][80][45]. Besides, it has been reported that the formation of ferroelectric polarization in an BNBT ceramic can cause an structural change from rhombohedral symmetry (at un-poled state) to tetragonal symmetry (at poled state) [123][124]. Therefore, it would be interesting to study the E-field-dependent PL properties of RE^{3+}-doped BNBT ceramics. Although the effects of poling process on PL properties have been extensively investigated, there is little work studying the E-field dependences of the PL properties, especially for bulk ceramics. In this chapter, the effects of (external) E-field on PL properties for the BNBT-0.005Er ceramic have been studied.

6.2. Preparation of transparent electrode

For the PL measurements under an E-field, a transparent electrode was deposited on one surface of the ceramic samples for allowing them to be irradiated with the excitation light. For the ease of establishing a high E-field, the ceramic samples were thinned down to about 0.12 mm thick. A silver electrode was first fired on one of the surfaces. After that, an indium tin oxide (ITO) transparent electrode was deposited on the other surface by a physical vapour deposition method called magnetron sputtering. Fig. 6.1 shows the schematic diagram of the sputtering system. The sample was heated up to 350^{o}C for better crystallization of ITO. The sputtering was then carried out in a gas mixture of argon and oxygen (Ar/O_2 = 60/1) at a pressure of 5 mTorr. During sputtering, Ar plasma was generated by RF source, and the ITO target was bombarded by the Ar ions. ITO atoms were then knocked off and attracted to deposit on the sample surface for 30 min. After sputtering, the temperature was cooled down to room temperature before the chamber was opened.

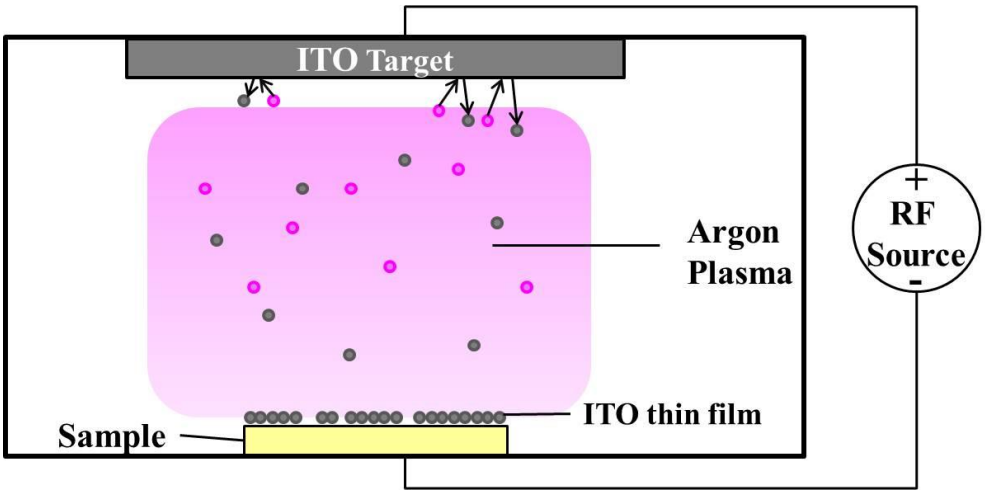

Figure 6.1 The schematic diagram of magnetron sputtering.

6.3. E-field induced PL property

In order to study the E-field-induced PL properties, an (static) E-field in the range of 0 – 3.6 kV/mm has been applied to the BNBT-0.005Er ceramic at room temperature, and the corresponding visible up-conversion (UC) spectra under an excitation of 980 nm have been measured, giving the results shown in Fig. 6.2. The ceramic would electrically break down if an E-field higher than 3.6 kV/mm was applied. For the ease of observation, the baselines of the spectra were shifted upwards by different amounts. The spectra have almost the same shape, and no obvious shifting in the peak wavelengths has been observed. This suggests that the E-field does not affect the splitting of the energy levels of Er^{3+} in the BNBT host.

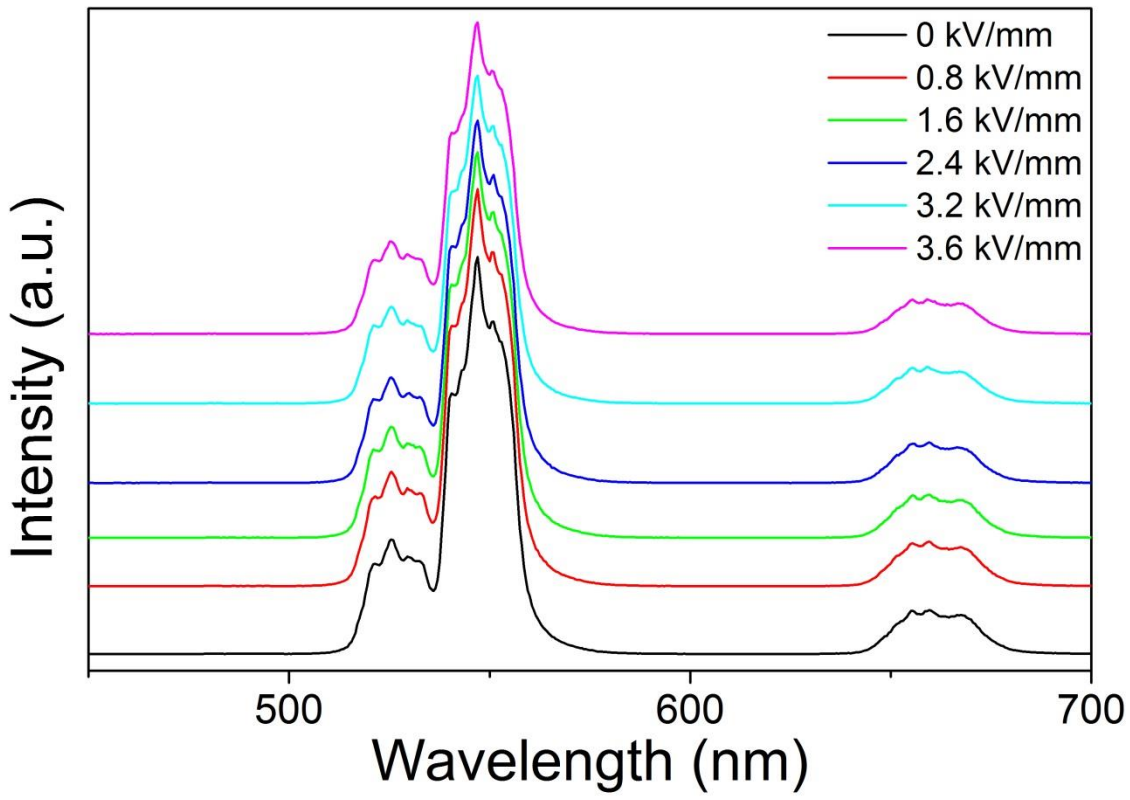

Figure 6.2 Visible UC emission spectra of the BNBT-0.005Er ceramic.

Fig. 6.3 shows the (relative) PL intensity at 547 nm of the BNBT-0.005Er ceramic under different E-fields. The observed PL intensity remains almost unchanged as the E-field increases from 0 to 1 kV/mm, and then decreases significantly with increasing E-field. At 3.6 kV/mm, the PL intensity retains only about 78% of the original value (i.e., the PL intensity before the application of any E-field). This should be partly attributed to the increase in structural symmetry and then the change in crystal field around Er^{3+} arisen from the alignment of dipoles [80][45][123]. The decrease in PL intensity may also be resulted from the increase in structural symmetry induced by the E-field [121]. As discussed in the previous chapters, the BNBT-0.005Er ceramic resides near the MPB, containing both the rhombohedral and tetragonal phases. As the E-field increases to a low value of 2 kV/mm , part of the rhombohedral structure starts to transform into the tetragonal structure [124], and thus leading to an increase in structural symmetry.

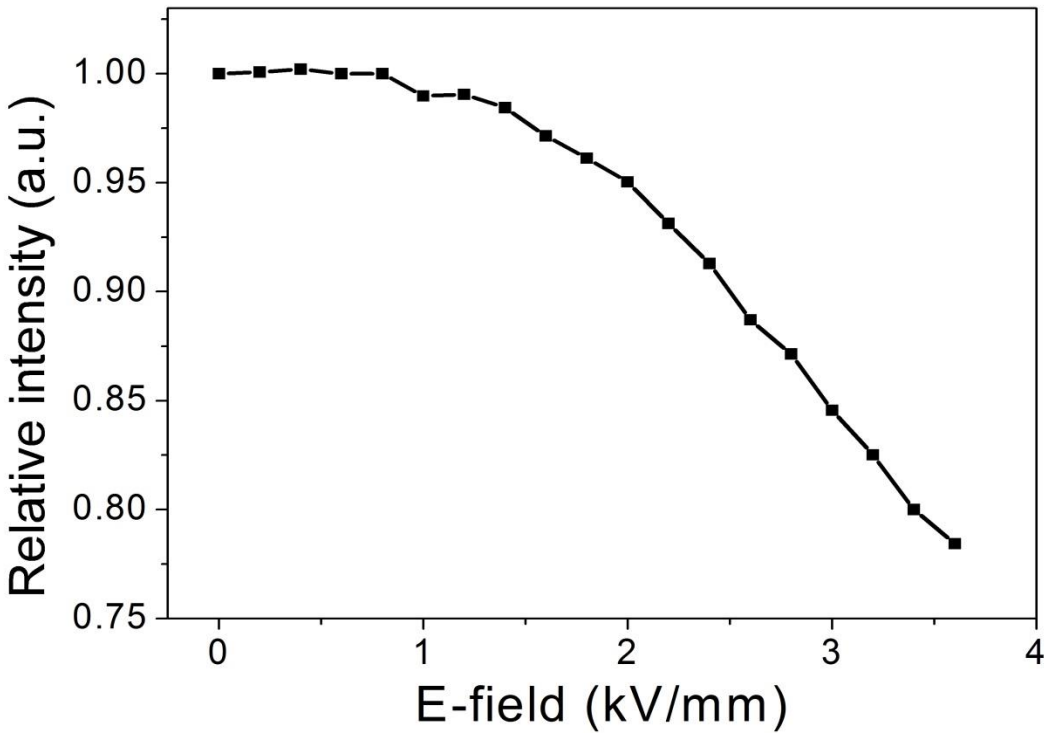

Figure 6.3 E-field dependence of relative intensity (547 nm) of the BNBT-0.005Er ceramic.

For studying the reversibility of the change in PL intensity, a series of (static) E-fields, varying in a step of 0.9 kV/mm between 0 to 3.6 kV/mm several times (Fig. 6.4a), has been applied to the ceramics, and the corresponding PL intensities at 547 nm have been measured, giving the results shown in Fig. 6.4b. At each step, the E-field has been applied for 10 min before the PL measurement. It has been noted that the PL intensity changes rapidly in the first 3 min and becomes saturated after 10 min. This may be partly attributed to the slow switching process of dipoles. As shown in Fig. 6.4(b), the change in PL intensity is not completely reversible in the first E-field cycle. As the E-field decreases from the highest value of 3.6 kV/mm to 0 kV/mm, only about half of the decrease in PL intensity is recovered. This may be partly due to the remanent polarization and partly due to the irreversible crystal transformation [124]. However, it is interesting to note that the reversibility is improved in the consecutive cycles, and the observed PL intensity restores almost back to the preceding value (i.e., the PL intensity before the increase of E-field from 0 kV/mm), suggesting that most of the dipole switching and crystal transformation in those cycles are reversible. Probably due to the increase in remanent polarization, the PL intensities decrease continuously at each minimum E-field (0 kV/mm) and maximum E-field (3.6 kV/mm), respectively (inset of Fig. 6.4b). It should be noted that the maximum E-field (3.6 kV/mm) used in this reversibility study is lower than the E-field (5 kV/mm) used for fully polarize the samples at 60°C.

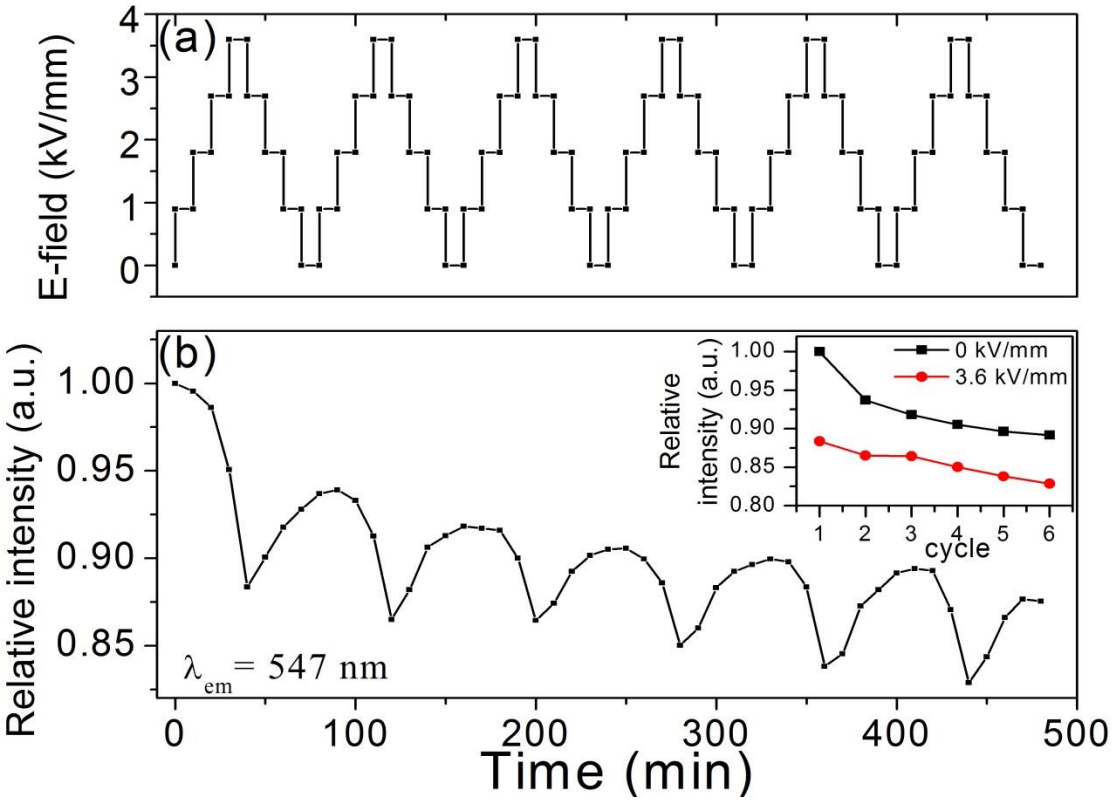

Figure 6.4 (a) Variation of applied E-field and (b) E-field dependence of relative PL intensity (547 nm) of the BNBT-0.005Er ceramic. The inset presents the relative PL intensity (547 nm) at 0 and 3.6 kV/mm in the consecutive E-field cycles.

It can also be seen from Fig. 6.4b that the decrease in the observed PL intensity (for the first increase of E-field from 0 to 3.6 kV/mm) is not as large as that in Fig. 6.3. This suggests that the change in PL intensity may also be affected by the way how the E-field is applied, e.g., the change step and duration. All the measurement conditions, such as the power of the excitation source were kept the same for all the PL measurements. For the results shown in Fig. 6.3, the E-field was increased in a step of 0.2 kV/mm to 3.6 kV/mm, and the total duration (at different E-fields) was about 180 min. Fig. 6.5 shows the observed PL intensity at 547 nm of the BNBT-0.005Er ceramic

subjected to a constant E-field (3.6 kV/mm) for different durations. It can be seen that the decrease in PL intensity is again not the same as the previous ones. Indeed, the discrepancy may be attributed to the variations of samples prepared from different times (about ±5% in terms of ε_r). There may also be other factors affecting the PL intensity, and more investigations may then be needed.

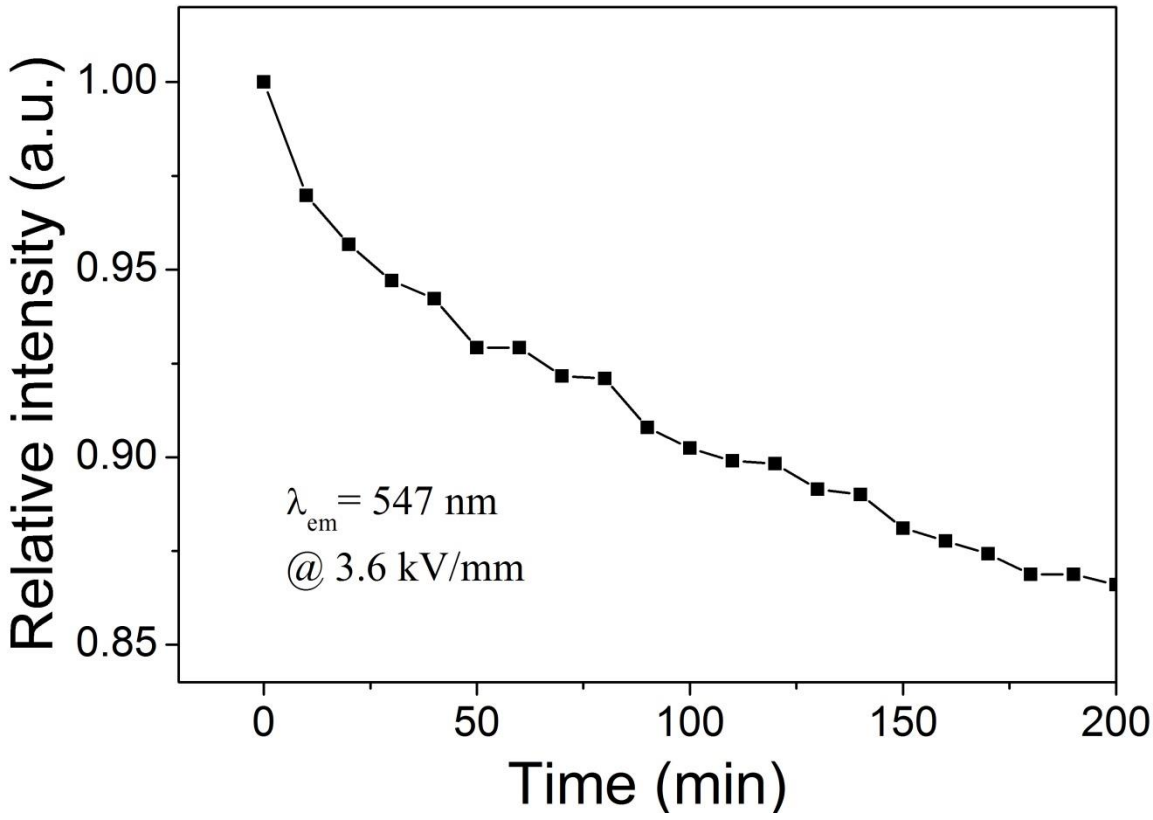

Figure 6.5 Relative PL intensity (547 nm) of the BNBT-0.005Er ceramics under constant E- field.

It has been noted that although the exact PL intensity as well as the changes induced by the E-field of different samples may be different, the different between the PL intensities at the maximum and minimum E-field remains almost the same (about 5%), especially for the consecutive E-field cycles (Fig. 6.4b). Fig. 6.6 shows the PL intensities at 0 kV/mm and 3.6 kV/mm in different E-field cycles for another

BNBT-0.05Er ceramic sample. For this case, a constant E-field of 3.6 kV/mm was applied to the sample for about 300 min. before the measurements. Similarly the changes in PL intensity in different E-field cycles are different from those shown in Fig. 6.4b. Nevertheless, the difference between the PL intensities at the maximum and minimum E-field is almost the same as before (~5%). This suggests that the E-field-induced change in PL intensity may be employed for control or sensing applications.

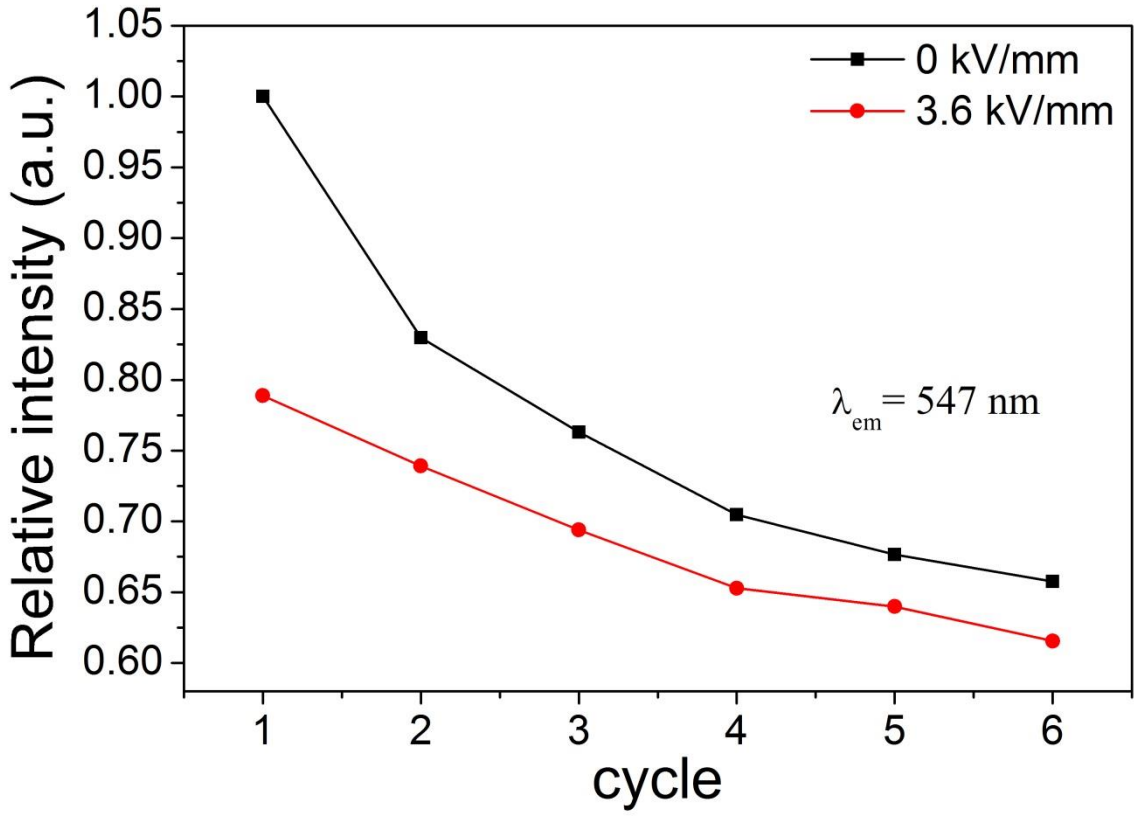

Figure 6.6 Relative PL intensity (547 nm) of the BNBT-0.005Er ceramic at 0 and 3.6 kV/mm in the consecutive E-field cycles.

6.4. Conclusion

BNBT-0.005Er ceramics with transparent ITO electrodes have been successfully prepared for studying the effects of E-field on PL properties. Our results reveal that the E-field does not affect the splitting of energy levels of Er^{3+} in BNBT ceramics. However, it can decrease the PL intensity effectively. Under a static E-field of 3.6 kV/mm, the decrease can be up to 22%. This should be partly attributed to the increase in structural symmetry arisen from dipoles alignment, and partly attributed to the increase in crystal symmetry arisen from E-field induced transformation. Although the change is not entirely reversible in the first E-field cycle, the reversibility is improved in the consecutive cycles. The difference between the observed PL intensity at the minimum and maximum E-field (0 and 3.6 kV/mm, respectively) remains almost the same for different E-field cycles as well as different samples, suggesting that the ceramics should be potential candidates for electric controlled multifunctional optoelectronic applications.

Chapter 7. Conclusion

Novel multifunctional lead-free rare-earth (RE^{3+})-doped $0.93(Bi_{0.5}Na_{0.5}TiO_3)$-$0.07(BaTiO_3)$ (BNBT)-based ceramics with good photoluminescence (PL), dielectric, piezoelectric and ferroelectric properties have been developed for various optoelectronic applications. Er^{3+} and Pr^{3+} are used as activators, and the ceramics are prepared by the conventional solid state reaction (SSR) method. The PL properties of the ceramics have been systematically investigated, and the effects of vacancies and dopant concentration have been studied. The corresponding PL mechanisms and energy transfer (ET) processes have also been deduced. As a type of ferroelectric ceramics, the effects of RE^{3+}-doping on the dielectric, piezoelectric and dielectric properties have also been studied.

BNBT ceramics doped with 0.01 mole Er^{3+} at various sites (BNBT-Er(y), where y is Bi, Ti, Ba or Na for denoting the ions replaced by Er^{3+}) have been prepared and the effects of the resulting vacancies, including both oxygen (V_o) and cation vacancies (V_c), on PL and electrical properties have been studied. All the ceramics possess a single-phase perovskite structure, suggesting that Er^{3+} has diffused into the corresponding sites of the BNBT lattice. Under an excitation of 980 nm, the ceramics exhibit strong green and red up-conversion (UC) emissions and near-infrared (NIR) and mid-infrared (MIR) down-conversion (DC) emissions. Our results also reveal that the vacancies arisen from charge imbalance between the dopants and the replaced ions could increase the PL intensity of the NIR and MIR emission bands at the expense of the visible emissions. For the BNBT-Er(Ba) ceramic containing V_c, a looping

mechanism is established such that the PL intensity of the NIR emission band increases significantly by more than 50%. The resulting effects of the looping mechanism is stronger in the BNBT-Er(Na) ceramic which contains more V_c. The BNBT-Er(y) ceramics also exhibit good dielectric, ferroelectric and piezoelectric properties, and hence they should have great potential for multifunctional applications.

BNBT ceramics doped with various contents of Er^{3+} at the Bi-site (BNBT-xEr) have been prepared and their PL, ferroelectric, dielectric and piezoelectric properties have been studied. The ceramics possess a single-phase perovskite structure, and the densification is improved by the Er^{3+}-doping. Under an excitation of 980 nm, the ceramics exhibit visible UC emissions at 532 nm (green), 547 nm (green) and 660 nm (red), as well as NIR (1.44 - 1.66 μm) and MIR (2.62 - 2.84 μm) DC emissions. Owing to the higher probability of cross relaxation (CR) and efficient multi-phonon relaxation (MPR) at higher Er^{3+} concentrations, the PL intensity of the red emission increases significantly by more than 47 times as x increases from 0.005 to 0.07. As a result, the Commission Internationale de L'Eclairage (CIE) chromaticity coordinates shift from (0.29, 0.69) to (0.49, 0.50) and the emission color shows an obvious change from green to yellowish green color. Probably due to the establishment of a dynamic circulatory energy process, the PL intensity of the MIR emission increases significantly by more than 4 times at the expense of NIR emission. The quenching concentration for the ceramics is high, about 6%. The BNBT-xEr ceramics also exhibit good dielectric, piezoelectric and ferroelectric properties, and hence they should have great potential for multifunctional applications.

BNBT ceramics doped with various contents of Pr^{3+} at the Bi-site (BNBT-xPr) have been prepared and their PL, ferroelectric, dielectric and piezoelectric properties

have been studied. Our results reveal that Pr^{3+} has diffused into the Bi^{3+} sites to form a single-phase perovskite structure. Under an excitation of 474 nm, the ceramics exhibit various DC emissions in visible light (green and red) and NIR regions. The quenching concentration is low, about a molar fraction of 0.005. Owing to the enhancement of CR, the PL intensity of the emissions at 654 nm and 741 nm increase significantly with increasing x. On the other hand, the enhanced CR processes decrease the PL intensities of the other emissions, both in the visible and NIR regions. For the BNBT-xPr ceramics with $x \leq 0.005$, both the PL properties and the dielectric, piezoelectric and ferroelectric properties are very good. Therefore, they should be a promising candidate for multifunctional optoelectronic applications.

The effects of (external) electric field (E-field) on PL properties of the BNBT-0.005Er ceramic have been studied. An ITO transparent electrode is deposited on one of the surfaces of the sample for allowing them to be irradiated with the excitation light. Our results reveal that the E-field does not affect the splitting of energy levels of Er^{3+} in BNBT ceramics. However, it can decrease the PL intensity effectively. Under a static E-field of 3.6 kV/mm, the decrease can be up to 22%. This should be partly attributed to the increase in structural symmetry arisen from dipoles alignment, and partly attributed to the increase in crystal symmetry arisen from E-field induced transformation. Although the change is not entirely reversible in the first E-field cycle, the reversibility is improved in the consecutive cycles. The difference between the observed PL intensity at the minimum and maximum E-field (0 and 3.6 kV/mm, respectively) remains almost the same for different E-field cycles as well as different samples, suggesting that the ceramics should be potential candidates for electric controlled multifunctional optoelectronic applications.

Reference

[1] S. Shionoya, W. Yen, T. Hase, *Phosphor Handbook*, **1999**.

[2] G. Blasse, *Luminescent Materials*, Springer. Verlag Berlin Heidelberg, **1994**.

[3] K. N. Shinde, S. J. Dhoble, H. C. Swart, K. Park, *Phosphate Phosphors for Solid-State Lighting*, Springer Berlin Heidelberg, Berlin, Heidelberg, **2012**.

[4] D. Peng, H. Zou, C. Xu, X. Wang, X. Yao, J. Lin, T. Sun, *AIP Adv.* **2012**, *2*, 042187.

[5] M.-K. Tsang, S. Zeng, H. L. W. Chan, J. Hao, *Opt. Mater. (Amst).* **2013**, *35*, 2691.

[6] Y. Zhang, J. Hao, *J. Appl. Phys.* **2013**, *113*, 184112.

[7] H. Zhang, D. Sun, J. Luo, S. Cao, M. Cheng, Q. Zhang, S. Yin, *J. Lumin.* **2015**, *158*, 215.

[8] K. . Gschneidner, Jr., L. Eyring, *Handbook on the Physics and Chemistry of Rare Earths*, Elsevier Science Publishers B.V., **1987**.

[9] C. Pfau, U. Skrzypczak, B. Ahrens, S. Schweizer, *J. physics. Condens. matter* **2014**, *26*, 025406.

[10] R. Ious, Y. Orthoaluminate, *Phys. Rev. B* **1973**, *8*.

[11] M. J. W. C. B. Layne, W. H. Lowdermilk, *Phys. Rev. B* **1977**, *16*, 10.

[12] M. Yamaga, H. Uno, S. Tsuda, J.-P. R. Wells, T. P. J. Han, *J. Lumin.* **2012**, *132*, 1608.

[13] Y. G. Choi, B. J. Park, K. H. Kim, J. Heo, *Chem. Phys. Lett.* **2003**, *368*, 625.

[14] M. Haase, H. Schäfer, *Angew. Chem. Int. Ed. Engl.* **2011**, *50*, 5808.

[15] J. F. Suyver, a. Aebischer, D. Biner, P. Gerner, J. Grimm, S. Heer, K. W. Krämer, C. Reinhard, H. U. Güdel, *Opt. Mater. (Amst).* **2005**, *27*, 1111.

[16] F. Wang, X. Liu, *Chem. Soc. Rev.* **2009**, *38*, 976.

[17] G. Chen, T. Y. Ohulchanskyy, A. Kachynski, H. Agren, P. N. Prasad, *ACS Nano* **2011**, *5*, 4981.

[18] J. S. Chivian, W. E. Case, D. D. Eden, *Appl. Phys. Lett.* **1979**, *35*, 124.

[19] W. E. Case, M. E. Koch, a. W. Kueny, *J. Lumin.* **1990**, *45*, 351.

[20] M. Joubert, *Opt. Mater. (Amst).* **1999**, *11*, 181.

[21] Y. Li, Z. Song, C. Li, R. Wan, J. Qiu, Z. Yang, Z. Yin, Y. Yang, D. Zhou, Q. Wang, *Appl. Phys. Lett.* **2013**, *103*, 231104.

[22] F. Auzel, *Chem. Rev.* **2004**, *104*, 139.

[23] G. Chen, L. Yang, C. Xu, S. Hao, H. Qiu, L. Sun, Y. Xu, C. Yang, *Opt. Lett.* **2012**, *37*, 1268.

[24] X. Huang, S. Han, W. Huang, X. Liu, *Chem. Soc. Rev.* **2013**, *42*, 173.

[25] Q. Y. Zhang, X. Y. Huang, *Prog. Mater. Sci.* **2010**, *55*, 353.

[26] B. M. van der Ende, L. Aarts, A. Meijerink, *Adv. Mater.* **2009**, *21*, 3073.

[27] P. Vergeer, T. Vlugt, M. Kox, M. den Hertog, J. van der Eerden, a. Meijerink, *Phys. Rev. B* **2005**, *71*, 014119.

[28] G. E. Rindone, in *Lumin. Inorg. Soilds* (Ed.: P. Goldberg), Academic Press INC., New York, **1966**, pp. 419–462.

[29] A. de Bettencpurt-Dias, *The Rare Earth Elements: Fundamentals and Applications*, John Wiley & Sons Limited, **2012**.

[30] F. Träger, in *Springer Handb. Lasers Opt.*, Springer Science+Business Media, New York, **2007**, pp. 583–936.

[31] G. Liu, *Chem. Soc. Rev.* **2015**, DOI 10.1039/C4CS00187G.

[32] L. Tsonev, *Opt. Mater. (Amst).* **2008**, *30*, 892.

[33] a. J. Silversmith, W. Lenth, R. M. Macfarlane, *Appl. Phys. Lett.* **1987**, *51*, 1977.

[34] S. Ivanova, F. Pellé, *J. Opt. Soc. Am. B* **2009**, *26*, 1930.

[35] T. Sanamyan, M. Kanskar, Y. Xiao, D. Kedlaya, M. Dubinskii, *Opt. Express* **2011**, *19*, 1082.

[36] M.-K. Tsang, G. Bai, J. Hao, *Chem. Soc. Rev.* **2014**, DOI 10.1039/c4cs00171k.

[37] X. Wu, C. M. Lau, K. W. Kwok, *J. Lumin.* **2014**, *155*, 343.

[38] M. Wojdak, H. Jayatilleka, M. Shah, a. J. Kenyon, F. Gourbilleau, R. Rizk, *J. Lumin.* **2013**, *136*, 407.

[39] A. Polman, *Phys. B* **2001**, *300*, 78.

[40] G. Blasse, in *Struct. Bond. 26*, Springer. Verlag Berlin Heidelberg, **1976**, pp. 43–82.

[41] W. W. Piper, J. a. DeLuca, F. S. Ham, *J. Lumin.* **1974**, *8*, 344.

[42] L. Guerbous, M. Seraiche, O. Krachni, *J. Lumin.* **2013**, *134*, 165.

[43] P. Du, L. Luo, W. Li, Y. Zhang, H. Chen, *J. Alloys Compd.* **2013**, *559*, 92.

[44] D. Peng, H. Sun, X. Wang, J. Zhang, M. Tang, X. Yao, *J. Alloys Compd.* **2012**, *511*, 159.

[45] P. Du, L. Luo, W. Li, Y. Zhang, H. Chen, *J. Alloys Compd.* **2013**, *551*, 219.

[46] G. Zhu, Z. Ci, Y. Shi, Y. Wang, *J. Rare Earths* **2013**, *31*, 1049.

[47] F. Zhu, Z. Xiao, L. Yan, F. Zhang, K. Zhong, G. Cheng, *Nucl. Instruments Methods Phys. Res. Sect. B Beam Interact. with Mater. Atoms* **2009**, *267*, 3100.

[48] G. H. Haertling, *J. Am. Ceram. Soc.* **1999**, *82*, 797.

[49] Y. Xu, *Ferroelectric Materials and Their Applications*, Elsevier Science Publishers B.V., **1991**.

[50] D. Damjanovic, *Reports Prog. Phys.* **1998**, *61*, 1267.

[51] S. Bhagavantam, S. Radhakrishna, in *Proc. Indian Acad. Sci. - Sect. A*, Springer, **1969**, pp. 182–188.

[52] P. V. Lambeck, G. H. Jonker, *J. Phys. Chem. Solids* **1986**, *47*, 453.

[53] M. Oualla, a. Zegzouti, M. Elaatmani, M. Daoud, D. Mezzane, Y. Gagou, P. Saint-Grégoire, *Ferroelectrics* **2003**, *291*, 133.

[54] V. A. Stephanovich, *J. Physics. Condens. matter* **2010**, *22*, 235902.

[55] D. C. Arnold, F. D. Morrison, *J. Mater. Chem.* **2009**, *19*, 6485.

[56] N. N. Kolpakova, P. P. Syrnikov, a. O. Lebedev, P. Czarnecki, W. Nawrocik, C. Perrot, L. Szczepanska, *J. Appl. Phys.* **2001**, *90*, 6332.

[57] X. W. Dong, K. F. Wang, S. J. Luo, J. G. Wan, J. –M. Liu, *J. Appl. Phys.* **2009**, *106*, 104101.

[58] T. M. McQueen, D. V West, B. Muegge, Q. Huang, K. Noble, H. W. Zandbergen, R. J. Cava, *J. Phys. Condens. Matter* **2008**, *20*, 235210.

[59] A. Ando, M. Kimura, in *Lead- Free Ceram.* (Eds.: S. Priya, S. Nahm), Springer, **2012**, p. 373.

[60] H. Jaffe, B.; Cook, W. R.; Jaffe, *Piezoelectric Ceramics*, Academic: New York, **1971**.

[61] J. W. Wanders, *Piezoelectric Ceramics-Properties and Applications*, Philips Components: Eindhoven, **1991**.

[62] W. Lin, L. Fan, D. Lin, Q. Zheng, X. Fan, H. Sun, *Curr. Appl. Phys.* **2013**, *13*, 159.

[63] S. E. Park, W. Hackenberger, *Curr. Opin. Solid State Mater. Sci.* **2002**, *6*, 11.

[64] E. M. Sabolsky, a. R. James, S. Kwon, S. Trolier-McKinstry, G. L. Messing, *Appl. Phys. Lett.* **2001**, *78*, 2551.

[65] S. Zhang, R. Xia, T. R. Shrout, *J. Electroceramics* **2007**, *19*, 251.

[66] S. Guillemet-Fritsch, Z. Valdez-Nava, C. Tenailleau, T. Lebey, B. Durand, J.-Y. Chane-Ching, *Adv. Mater.* **2008**, *20*, 551.

[67] C. Xu, D. Lin, K. W. Kwok, *Solid State Sci.* **2008**, *10*, 934.

[68] B. Parija, T. Badapanda, P. Sahoo, M. Kar, P. Kumar, S. Panigrahi, *Process. Appl. Ceram.* **2013**, *7*, 73.

[69] W. Ge, H. Liu, X. Zhao, X. Li, X. Pan, D. Lin, H. Xu, X. Jiang, H. Luo, *Appl. Phys. A* **2009**, *95*, 761.

[70] C.-W. Ahn, C.-S. Park, R. Dittmer, S.-H. Hong, S. Priya, *J. Mater. Sci.* **2010**, *45*, 3961.

[71] D. Gao, K. W. Kwok, D. Lin, H. L. W. Chan, *J. Phys. D. Appl. Phys.* **2009**, *42*, 035411.

[72] E. Hollenstein, M. Davis, D. Damjanovic, N. Setter, *Appl. Phys. Lett.* **2005**, *87*, 182905.

[73] W. Lu, Y. Wang, G. Fan, X. Wang, F. Liang, *J. Alloys Compd.* **2011**, *509*, 2738.

[74] E. F. Alberta, R. Guo, A. S. Bhalla, in *Morphotropic Phase Bound. Perovskites, High Strain Piezoelectrics, Dielectr. Ceram.*, **2003**, pp. 55–64.

[75] Y. Guo, Y. Liu, R. L. Withers, F. Brink, H. Chen, *Chem. Mater.* **2011**, *23*, 219.

[76] B. Parija, T. Badapanda, S. Panigrahi, T. P. Sinha, *J. Mater. Sci. Mater. Electron.* **2012**, *24*, 402.

[77] Y. Guo, K. Kakimoto, H. Ohsato, *Jpn. J. Appl. Phys.* **2004**, *43*, 6662.

[78] Y. Guo, K. Kakimoto, H. Ohsato, *Solid State Commun.* **2004**, *129*, 279.

[79] J. Ryu, S. Priya, K. Uchino, H. Kim, *J. Electroceramics* **2002**, *8*, 107.

[80] P. Du, L. Luo, W. Li, Y. Zhang, H. Chen, *Mater. Sci. Eng. B* **2013**, *178*, 1219.

[81] P. Du, L. Luo, W. Li, Q. Yue, *J. Appl. Phys.* **2014**, *116*, 014102.

[82] X. Wang, C.-N. Xu, H. Yamada, K. Nishikubo, X.-G. Zheng, *Adv. Mater.* **2005**, *17*, 1254.

[83] C.-N. Xu, X.-G. Zheng, M. Akiyama, K. Nonaka, T. Watanabe, *Appl. Phys. Lett.* **2000**, *76*, 179.

[84] Y. Liu, C.-N. Xu, *Appl. Phys. Lett.* **2004**, *84*, 5016.

[85] E. Smith, G. Dent, *Modern Raman Spectroscopy- A Practical Approach*, John Wiley & Sons Limited, **2005**.

[86] C. B. Sawyer, C. H. Tower, *Phys. Rev.* **1930**, *35*, 269.

[87] L. Luo, P. Du, W. Li, W. Tao, H. Chen, *J. Appl. Phys.* **2013**, *114*, 124104.

[88] Y. Zhang, J. Hao, C. L. Mak, X. Wei, *Opt. Express* **2011**, *19*, 1824.

[89] L. Chen, X. Wei, X. Fu, *Trans. Nonferrous Met. Soc. China* **2012**, *22*, 1156.

[90] M. Paredes-Olguín, I. a. Lira-Hernández, C. Gómez-Yáñez, F. P. Espino-Cortés, *Phys. B Condens. Matter* **2013**, *410*, 157.

[91] T. Takenaka, K. Maruyama, K. Sakata, *Jpn. J. Appl. Phys.* **1991**, *30*, 2236.

[92] D. Lin, K. W. Kwok, *J. Mater. Sci.* **2009**, *44*, 4953.

[93] A. Watcharapasorn, S. Jiansirisomboon, *Ceram. Int.* **2008**, *34*, 769.

[94] A. Yamaji, Y. Enomoto, K. Kinoshita, T. Murakami, *J. Am. Ceram. Soc.* **1977**, *60*, 97.

[95] B. Wylie-van Eerd, D. Damjanovic, N. Klein, N. Setter, J. Trodahl, *Phys. Rev. B* **2010**, *82*, 104112.

[96] R. Clement, A. Leaustic, K. Marnry, A. H. Franci, *J. Phys. Chem. Solids* **1994**, *55*, 9.

[97] V. E. Alexandrov, E. a. Kotomin, J. Maier, R. a. Evarestov, *Eur. Phys. J. B* **2009**, *72*, 53.

[98] Y. Cong, B. Li, S. Yue, D. Fan, X. Wang, *J. Phys. Chem. C* **2009**, *113*, 13974.

[99] S. F. Chichibu, A. Uedono, T. Onuma, B. a Haskell, A. Chakraborty, T. Koyama, P. T. Fini, S. Keller, S. P. Denbaars, J. S. Speck, U. K. Mishra, S. Nakamura, S. Yamaguchi, S. Kamiyama, H. Amano, I. Akasaki, J. Han, T. Sota, *Nat. Mater.* **2006**, *5*, 810.

[100] S. F. Chichibu, A. Uedono, T. Onuma, S. P. DenBaars, U. K. Mishra, J. S. Speck, S. Nakamura, in *Adv. Light Emit. Mater.*, Trans Tech Publications, **2008**, pp. 233–248.

[101] G. Chai, G. Dong, J. Qiu, Q. Zhang, Z. Yang, *Sci. Rep.* **2013**, *3*, 1598.

[102] Y. Hiruma, H. Nagata, T. Takenaka, *Jpn. J. Appl. Phys.* **2006**, *45*, 7409.

[103] S.-T. Zhang, A. B. Kounga, E. Aulbach, T. Granzow, W. Jo, H.-J. Kleebe, J. Rödel, *J. Appl. Phys.* **2008**, *103*, 034107.

[104] R. Zuo, C. Ye, X. Fang, J. Li, *J. Eur. Ceram. Soc.* **2008**, *28*, 871.

[105] C. Lu, Y. Cui, *Phys. B Condens. Matter* **2012**, *407*, 3856.

[106] D. Lin, K. W. Kwok, *J. Mater. Sci.* **2009**, *44*, 4953.

[107] M. Wu, Y. Lu, Y. Li, *J. Am. Ceram. Soc.* **2007**, *90*, 3642.

[108] L. Luo, P. Du, W. Li, W. Tao, H. Chen, *J. Appl. Phys.* **2013**, *114*, 124104.

[109] B. Wu, J. Qiu, N. Jiang, S. Zhou, J. Ren, D. Chen, X. Jiang, C. Zhu, *J. Mater. Res.* **2007**, *22*, 3410.

[110] G. Bai, Y. Zhang, J. Hao, *Sci. Rep.* **2014**, *4*, 5724.

[111] B. Zhou, L. Tao, Y. H. Tsang, W. Jin, E. Y. Pun, *Opt. Express* **2012**, *20*, 468.

[112] P. Y. Goh, K. a. Razak, S. Sreekantan, *J. Alloys Compd.* **2009**, *475*, 758.

[113] H. Sun, D. Peng, X. Wang, M. Tang, Q. Zhang, X. Yao, *J. Appl. Phys.* **2011**, *110*, 016102.

[114] K. Ruan, X. Chen, T. Liang, G. Wu, D. Bao, *J. Appl. Phys.* **2008**, *103*, 086104.

[115] W. J. Park, S. G. Yoon, D. H. Yoon, *J. Electroceramics* **2006**, *17*, 41.

[116] Y. Wei, Z. Wu, Y. Jia, J. Wu, Y. Shen, H. Luo, *Appl. Phys. Lett.* **2014**, *105*, 042902.

[117] H. Okamoto, K. Kasuga, I. Hara, Y. Kubota, *Opt. Express* **2009**, *17*, 20227.

[118] L. J. Borrero-González, G. Galleani, D. Manzani, L. a. O. Nunes, S. J. L. Ribeiro, *Opt. Mater. (Amst).* **2013**, *35*, 2085.

[119] V. Richard F., in *Princ. Pract. Bioanal.*, Taylor & Francis, **2000**, p. 119.

[120] H. Zhou, X. Liu, N. Qin, D. Bao, *J. Appl. Phys.* **2011**, *110*, 034102.

[121] J. Hao, Y. Zhang, X. Wei, *Angew. Chem. Int. Ed. Engl.* **2011**, *50*, 6876.

[122] T.-C. Huang, W.-F. Hsieh, *J. Fluoresc.* **2009**, *19*, 511.

[123] J. E. Daniels, W. Jo, J. Rödel, J. L. Jones, *Appl. Phys. Lett.* **2009**, *95*, 032904.

[124] J. E. Daniels, W. Jo, J. Rödel, V. Honkimäki, J. L. Jones, *Acta Mater.* **2010**, *58*, 2103.